9

Electrostatic Accelerators and Pulsed High Voltage

In this chapter we begin the study of charged particle acceleration. Subsequent chapters describe methods for generating high,-energy charged particle beams. The kinetic energy of a charged particle is increased by electric fields according to $\Delta T = \int \boldsymbol{E}(\boldsymbol{x},t) \cdot \boldsymbol{dx}$ [Eq. (3.16)], where the integral is taken along the particle orbit. This equation applies to all accelerators. The types of accelerators discussed in the next six chapters differ by the origin and characteristics of the electric field. In the most general case, **E** varies in time and position. In this chapter, we limit consideration to the special case of static electric fields.

Static electric fields can be derived from a potential function with no contribution from time-varying magnetic flux. An electrostatic accelerator consists basically of two conducting surfaces with a large voltage difference V_o. A particle with charge q gains a kinetic energy qV_o. In this chapter, we shall concentrate mainly on methods for generating high voltage. The description of voltage sources, particularly pulsed voltage generators, relies heavily on passive circuit analysis. Section 9.1 reviews the properties of resistors, capacitors, and inductors. A discussion of circuits to generate dc voltage follows in Section 9.2. The equations to describe ideal transformers are emphasized. A thorough knowledge of the transformer is essential to understand linear induction accelerators (Chapter 10) and betatrons (Chapter 11).

Section 9.4 introduces the Van de Graaff voltage generator. This device is used extensively in low-energy nuclear;physics. It also provides preacceleration for beams on many high-energy accelerators. The principles of dc accelerators are easily understood - the main difficulties associated with these machines are related to technology, which is largely an empirical field. Properties of insulators are discussed in Section 9.3 and Paschen's law for spark breakdown of an insulating gas is derived. The important subject of vacuum breakdown is reviewed in Section 9.5.

The remainder of the chapter is devoted to techniques of pulsed voltage generation. Acceleration by pulsed voltage accelerators is well described by the electrostatic approximation because the transit time of particles and the propagation time for electromagnetic waves in acceleration gaps are small compared to typical voltage pulslengths ($\Delta t \geq 50$ ns). Although the static approximation describes the acceleration gap, the operation of many pulsed power circuits, such as the transmission line, involves electromagnetic wave propagation. Pulsed voltage generators have widespread use in accelerators characterized by cyclic operation. In some instances they provide the primary power, such as in high-current relativistic electron beam generators and in the linear induction accelerator. In other cases, they are used for power conditioning, such as klystron drivers in high-gradient rf electron linear accelerators. Finally, pulsed voltage modulators are necessary to drive pulsed extraction and injection fields for synchrotrons and storage rings.

Pulsed voltage circuits must not only produce a high voltage but must also shape the voltage in time. Sections 9.5-9.14 introduce many of the circuits and techniques used. Material is included on critically damped circuits (Section 9.6) inpulse generators (Section 9.7), transmission line modulators (Section 9.9), the Blumlein transmission line (Section 9.10), pulse forming networks (Section 9.11), power compression systems (Section 9.12), and saturable core magnetic switching (Section 9.13). The equations for electromagnetic wave propagation in a transmission line are derived in Section 9.8. This section introduces the principles of interacting electric and magnetic fields that vary in time. The results will be useful when we study electromagnetic wave phenomena in rf accelerators. Material is also included on basic methods to measure fast-pulsed voltage and current (Section 9.14).

9.1 RESISTORS, CAPACITORS AND INDUCTORS

High-voltage circuits can usually be analyzed in terms of five elements: resistors, capacitors, inductors, ideal diodes, and ideal switches. These elements are two-terminal passive components. Two conductors enter the device, and two quantities characterize it. These are the current through the device and the voltage between the terminals. The action of the circuit element is described by the relationship between voltage and current. Standard symbols and polarity conventions are shown in Figure 9.1.

A. Voltage-Current Relationships

The ideal diode has zero voltage across the terminals when the current is positive and passes zero current when the voltage is negative. Diodes are used for rectification, the conversion of a bipolar voltage waveform into a dc voltage. A switch is either an open circuit (zero current at any

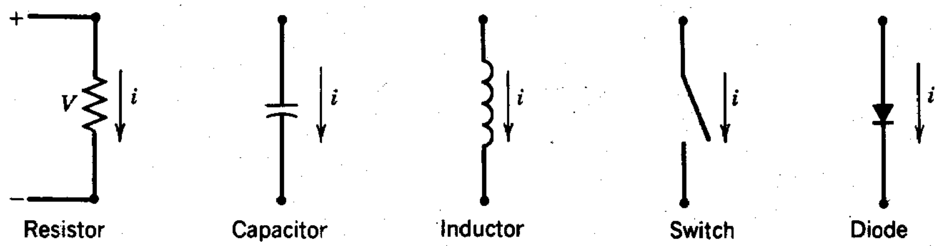

Figure 9.1 Symbols and polarity conventions for common circuit elements.

voltage) or a closed circuit (zero voltage at any current). In pulsed voltage circuits, a closing switch is an open circuit for times $t < 0$ and a short circuit for $t > 0$. An opening switch has the inverse properties. The spontaneous breakdown gap used on some pulse power generators and pulse sharpening circuits is an example of a two-terminal closing switch. Triggered switches such as the thyratron and silicon-controlled rectifier are more common; they are three terminal, two-state devices.

In this section, we consider the properties of resistors, capacitors, and inductors in the *time-domain*. This means that time variations of the total voltage are related to time variations of the total current. Relationships are expressed as differential equations. It is also possible to treat circuits in the *frequency-domain*. This approach is useful for oscillating harmonic circuits, and will be applied to rf cavities in Chapter 12. In the frequency-domain analysis, time variations are Fourier analyzed in terms of the angular frequency ω. Each harmonic component is treated separately. In the frequency-domain analysis, voltage and current in individual elements and multielement circuits are related simply by $V = a(\omega)I$, where $a(\omega)$ may be a complex number.

A resistor contains material that impedes the flow of electrons via collisions. The flow of current is proportional to the driving voltage

$$I = V/R, \tag{9.1}$$

where I is in amperes, V in volts, and R is the resistance in ohms (Ω). Energy is transferred from flowing electrons to the resistive material. With the polarity shown in Figure 9.1, electrons flow into the bottom of the resistor. Each electron absorbs an energy eV_o from the driving circuit during its transit through the resistor. This energy acts to accelerate the electrons between collisions. They emerge from the top of the resistor with low velocity because most of the energy gained was transferred to the material as heat. The number of electrons passing through the resistor per second is I/e. The power deposited is

$$P\ (watts) = VI = V^2/R = I^2R. \tag{9.2}$$

As we saw in Section 5.2, the basic capacitor geometry has two conducting plates separated by a dielectric (Figure 5.6c). The voltage between the plates is proportional to the stored charge on the plates and the geometry of the capacitor:

$$V = Q/C. \tag{9.3}$$

The quantity V is in volts, Q is in coulombs, and C is in farads (F). Neglecting fringing fields, the capacitance of the parallel plate geometry can be determined from Eq. (3.9):

$$C = \frac{\varepsilon_0\ (\varepsilon/\varepsilon_0)\ A}{\delta} \quad (F), \tag{9.4}$$

where $\varepsilon_o = 8.85 \times 10^{-12}$ and $\varepsilon/\varepsilon_o$ is the relative dielectric constant of the material between the plates, A is the plate area in square meters, and δ is the plate spacing in meters. Small capacitors in the pF range (10^{-12} F) look much like Figure 5.6c with a dielectric such as Mylar ($\varepsilon/\varepsilon_o \sim$ 2-3). High values of capacitance are achieved by combining convoluted reentrant geometries (for large A) with high dielectric constant materials. The current through a capacitor is the time rate of change of the stored charge. The derivative of Eq. (9.3) gives

$$I = C\ (dV/dt). \tag{9.5}$$

The capacitor contains a region of electric field. The inductor is configured to produce magnetic field. The most common geometry is the solenoidal winding (Fig. 4.18). The magnetic flux linking the windings is proportional to the current in the winding. The voltage across the terminals is proportional to the time-rate of change of magnetic flux. Therefore,

$$V = L\ (di/dt), \tag{9.6}$$

where L is a constant dependent on inductor geometry. Inductance is measured in Henries (H) in the mks system.

B. Electrical Energy Storage

A resistor converts electrical to thermal energy. There is no stored electrical energy that remains in a resistor when the voltage supply is turned off. Capacitors and inductors, on the other hand, store electrical energy in the form of electric and magnetic fields. Electrical energy can be extracted at a latter time to perform work. Capacitors and inductors are called *reactive* elements (*i.e.*, the energy can act again).

We can prove that there is no average energy lost to a reactive element from any periodic voltage waveform input. Voltage and current through the element can be resolved into Fourier components. Equations (9.5) and (9.6) imply that the voltage and current of any harmonic component are 90° out of phase. In other words, if the voltage varies as $V_o cos(\omega t)$, the current varies as $\pm I_o \sin(\omega t)$. Extending the arguments leading to Eq. (9.2) to reactive elements, the total energy change in an element is

$$\Delta U = \int Pdt = I_0 V_0 \int \sin(\omega t) \cos(\omega t).$$

Although the energy content of a reactive element may change over an oscillation period, the average over many periods is zero.

Energy is stored in a capacitor in the form of electric fields. Multiplying Eq. (5.19) by the volume of a parallel-plate capacitor, the stored energy is

$$U_c = ½ [\varepsilon_0 (\varepsilon/\varepsilon_0) (V/\delta)^2] A\delta. \tag{9.7}$$

Comparing Eq. (9.7) to (9.4),

$$U_c = ½ CV^2. \tag{9.8}$$

The magnetic energy stored in an inductor is

$$U_c = ½ LI^2. \tag{9.9}$$

C. Common Capacitor and Inductor Geometries

The coaxial capacitor (Fig. 9.2a) is often used as an energy storage device for high-voltage pulsed power generators. The electrodes are cylinders of length *d* with radii R_o and R_i . The cylinders have. a voltage difference V_o, and there is a medium with relative dielectric constant $(\varepsilon/\varepsilon_o)$ between them. Neglecting fringing fields at the ends, the electric field in the dielectric region is

$$E_r = Q/2\pi\varepsilon rd. \tag{9.10}$$

The integral of Eq. (9.10) from R_i to R_o equals V_o or

$$V_0 = (Q/2\pi\varepsilon d) \ln(R_o/R_i). \tag{9.11}$$

Comparing Eq. (9.11) with (9.3) shows the capacitance is

$$C = 2\pi\varepsilon d / \ln(R_o/R_i). \tag{9.12}$$

All current-carrying elements produce magnetic fields and thus have an inductance. There is a magnetic field between the cylinders of Figure 9.2b if current flows along the center conductor.

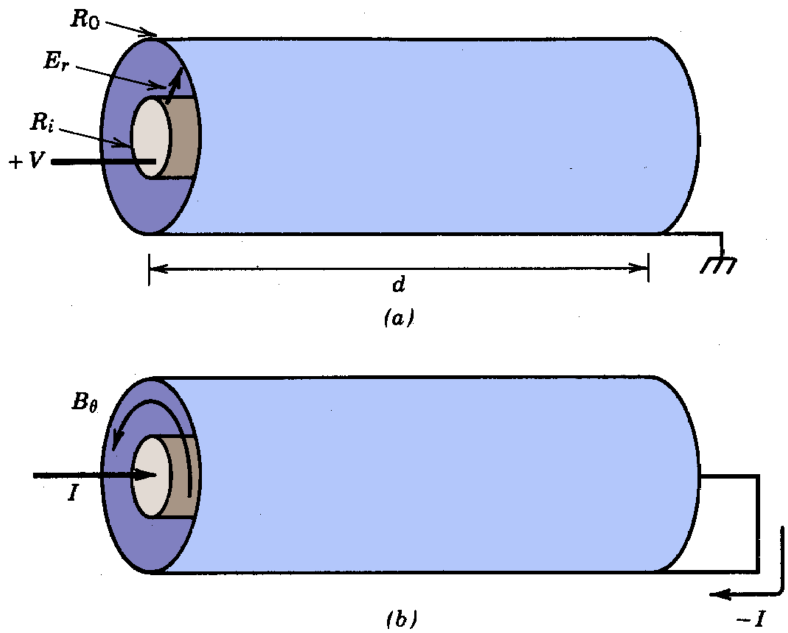

Figure 9.2 Lumped circuit elements. (*a*) Coaxial capacitor. (*b*) Coaxial inductor.

An equal and opposite current must return along the outer conductor to complete the circuit; therefore, there is no magnetic field for $r > R_o$. Equation (4.40) specifies that the field between the cylinders is

$$B_\theta(r) = \mu_0 I/2\pi r \tag{9.13}$$

if there is no ferromagnetic material in the intercylinder volume. The total magnetic field energy is

$$U_m = d \int dr\ (2\pi r)\ (B_\theta^2/2\mu_0) = (\mu_0/2\pi)\ (I^2/2)\ (d\ \ln(R_o/R_i)). \tag{9.14}$$

Setting U_m equal to $LI^2/2$ implies that

$$L = (\mu_0/2\pi)\ d\ \ln(R_o/R_i). \tag{9.15}$$

Equation (9.15) should be multiplied by μ/μ_o if the coaxial region contains a ferromagnetic material with an approximately linear response.

Coaxial inductors generally have between 0.1 and 1 μH per meter. Higher inductances are produced with the solenoidal geometry discussed in Section 4.6.We shall make the following assumptions to calculate the inductance of a solenoid: edge fields and curvature effects are neglected, the winding is completely filled with a linear ferromagnetic material, and N series windings of cross-sectional area A are uniformly spaced along a distance d. The magnetic field inside the winding for a series current I is

$$B_z = \mu I \ (N/d) \tag{9.16}$$

according to Eq. (4.42). Faraday's law implies that a time variation of magnetic field linking the windings produces a voltage

$$V = NA \ (dB_z/dt). \tag{9.17}$$

We can identify the inductance by combining Eqs. (9.16) and (9.17):

$$L = \mu_0 \ (\mu/\mu_0) \ N^2A/d. \tag{9.18}$$

Compact solenoids can assume a wide range of inductance values because of the strong scaling with N.

D. Introductory Circuits

Figure 9.3 shows a familiar circuit combining resistance, capacitance, and a switch. This is the simplest model for a pulsed voltage circuit; electrical energy is stored in a capacitor and then dumped into a load resistor via a switch. Continuity of current around the circuit combined with Eqs. (9.1) and (9.5) implies the following differential equation for the load voltage after switching:

$$C \ (dV/dt) + V/R = 0. \tag{9.19}$$

The solution (plotted in Fig. 9.3) for switching at $t = 0$ is $V(t) = V_o exp(-t/RC)$ with V_o the initial

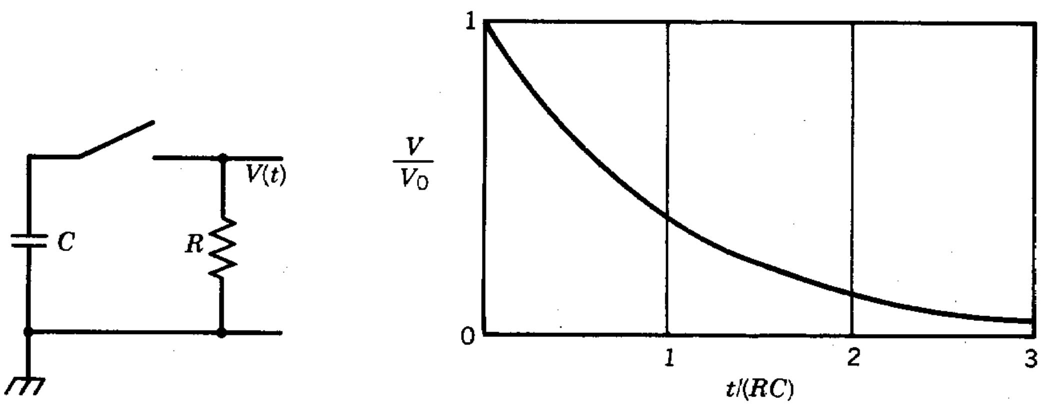

Figure 9.3 Time-dependent load voltage in a switched RC circuit.

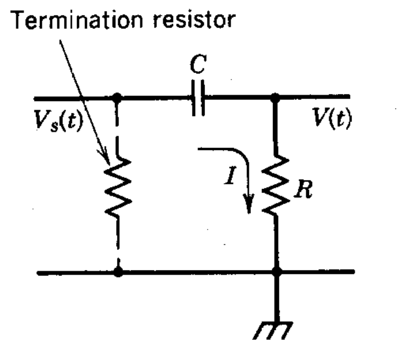

Figure 9.4 Passive integrator.

charge voltage. The *RC time* ($\Delta t = RC$) is the characteristic time for the transfer of energy from a capacitor to a resistor in the absence of inductance.

The passive integrator (Fig. 9.4) is a useful variant of the *RC* circuit. The circuit can integrate fast signals in the nanosecond range. It is often used with the fast diagnostics described in Section 9.14. Assume that voltage from a diagnostic, V(t) is incident from a terminated transmission line (Section 9.10). The signal has duration Δt. When $\Delta T \ll RC$, the voltage across the capacitor is small compared to the voltage across the resistor. Thus, current flowing into the circuit is limited mainly by the resistor and is given by $I \cong V_s(t)/R$. Applying Eq. (9.5), the output voltage is

$$V_{out} = \int V_s(t)\ dt\ /\ RC. \tag{9.20}$$

The passive integrator is fast, resistant to noise, and simple to build compared to a corresponding circuit with an operational amplifier. The main disadvantage is that there is a droop of the signal. For instance, if V_s is a square pulse, the signal at the end of the pulse is low by a factor $1 - \Delta t/RC$. An accurate signal integration requires that $RC \gg \Delta t$. This condition means that the output signal is reduced greatly, but this is usually not a concern for the large signals available from fast diagnostics.

A circuit with an inductor, resistor, voltage source, and switch is shown in Figure 9.5. This circuit models the output region of a pulsed voltage generator when the inductance of the leads and the load is significant. Usually, we want a rapid risetime for power into the load. The time for initiation of current flow to the load is limited by the undesirable (or parasitic) inductance. Continuity of current and the V-I relations of the components [Eqs. (9.1) and (9.6)] give the following differential equation for the load voltage:

$$\int V\ dt\ /\ L\ =\ V/R\ =\ 0. \tag{9.21}$$

The time variation for load voltage, plotted in Figure 9.5, is

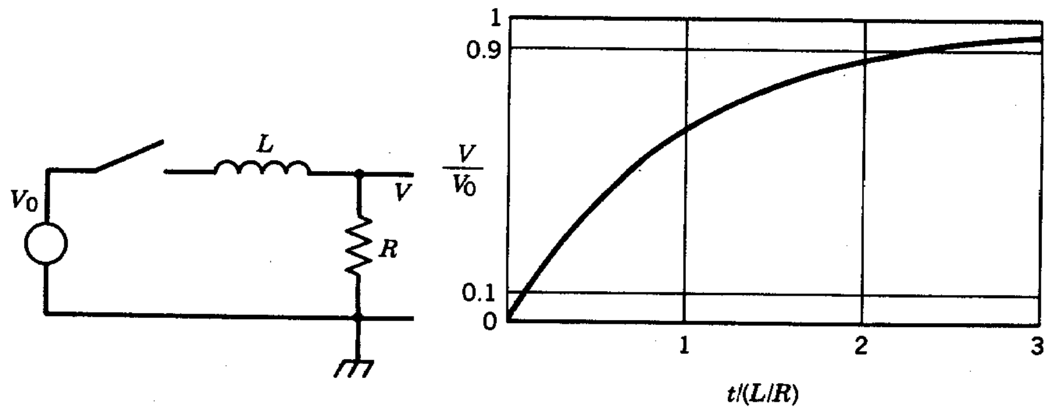

Figure 9.5 Time-dependent load voltage from a pulse generator with a series inductance.

$$V(t) = V_0\ [1 - \exp(-t/(L/R)]. \tag{9.22}$$

The *L/R time* determines how fast current and voltage can be induced in the load. The 10-90% risetime for the voltage pulse is 2.2(*L/R*). The load power varies as

$$P(t) = V^2(t)/R = (V_0^2/R)\ [1 - \exp(-t/(L/R)]^2. \tag{9.23}$$

The 10-90 time for the power pulse is 2.6(*L/R*). As an example, if we had a 50-ns pulse generator to drive a 25 Ω load, the total inductance of the load circuit must be less than 0.12 μH if the risetime is to be less than 25% of the pulsewidth.

9.2 HIGH-VOLTAGE SUPPLIES

The transformer is a prime component in all high-voltage supplies. It utilizes magnetic coupling to convert a low-voltage ac input to a high-voltage ac output at reduced current. The transformer does not produce energy. The product of voltage times current at the output is equal to or less than that at the input. T'he output can be rectified for dc voltage.

We will first consider the air core transformer illustrated in Figure 9.6. Insulated wire is wound uniformly on a toroidal insulating mandrel with $\mu \cong \mu_0$. There are two overlapped windings, the primary and the secondary. Power is introduced in the primary and extracted from the secondary. There is no direct connection between them; coupling is inductive via the shared magnetic flux in the torus. Assume that the windings have cross-sectional area A_t and average radius r_t. The primary winding has N_1 turns, and the secondary winding has N_2 turns. The symbol for the transformer with polarity conventions in indicated in Figure 9.6. The windings are oriented so that

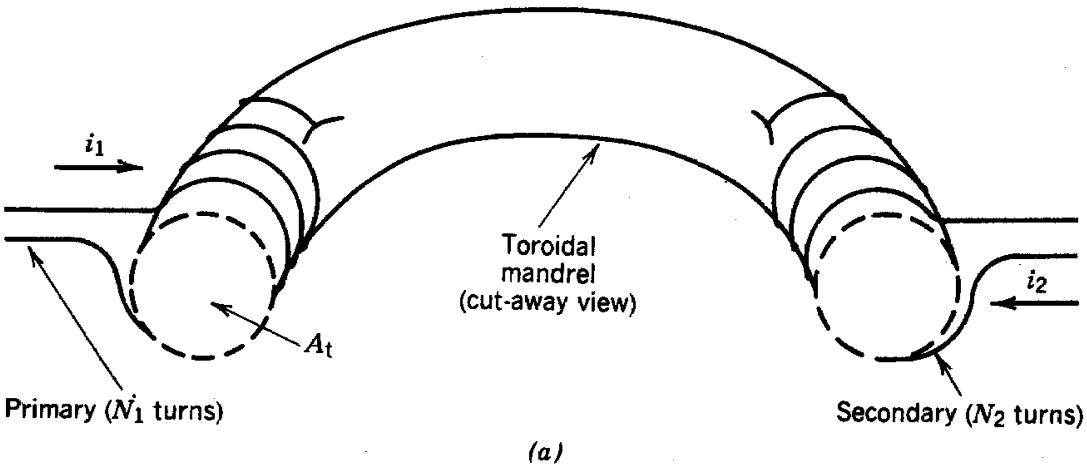

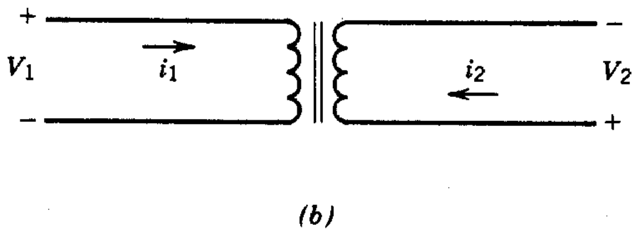

Figure 9.6 Air core transformer. (*a*) Geometry. (*b*) Circuit symbol.

positive i_1 and positive i_2 produce magnetic fields in opposite directions.

We will determine V_2 and i_2 in terms of V_1 and i_1 and find a simple model for a transformer in terms of the circuit elements of Section 9.1. First, note that energy entering the transformer on the primary can have two destinations. It can be transferred to the secondary or it can produce magnetic fields in the torus. The ideal transformer transfers all input energy to a load connected to the secondary; therefore, the second process is undesirable. We will consider each of the destinations separately and then make a combined circuit model.

To begin, assume that the secondary is connected to an open circuit so that $i_2 = 0$, no energy is transferred to the secondary. At the primary, the transformer appears to be an inductor with $L_1 = \mu_0 N_1^2 A_t / 2\pi r_t$. All the input energy is converted to magnetic fields; the load is reactive. The equivalent circuit is shown in Figure 9.7a.

Next, suppose the secondary is connected to a resistive load and that there is a way to make L_1 infinitely large. In this case, there is no magnetic field energy and all energy is transferred to the load. Infinite inductance means there are no magnetic fields in the torus with finite driving voltage. The field produced by current flow in the primary is exactly canceled by the secondary field. This means that

$$N_1 i_1 \cong N_2 i_2. \tag{9.24}$$

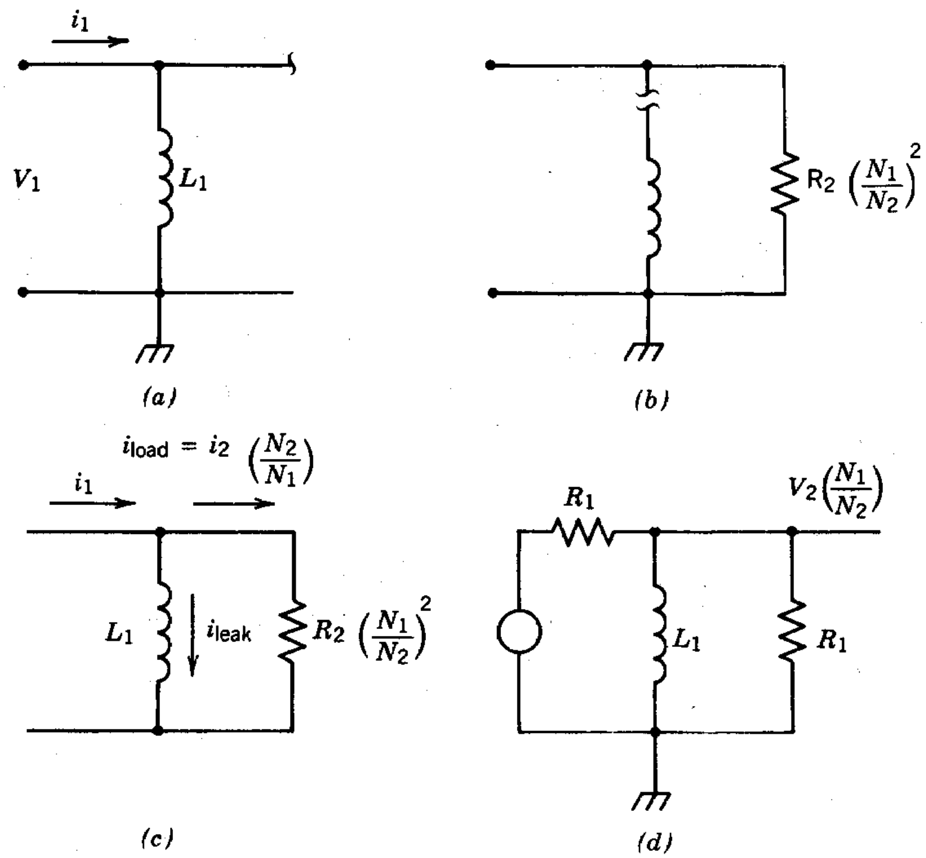

Figure 9.7 Equivalent circuit models for a transformer with ideal coupling. (*a*) Open circuit load on secondary. (*b*) Infinite primary shunt inductance. (*c*) Basic circuit model for an ideal transformer with a resistive load on the secondary. (*d*) Driving a resistive load on the secondary by a pulse modulator with matched impedance at the primary.

Equation (9.24) holds, if the transformer is perfectly wound so that the primary and secondary windings enclose the same area. This situation is called *ideal coupling*. With ideal coupling, the windings enclose equal magnetic flux so that

$$N_1 \; (d\Phi/dt) \; = \; V_1,$$
$$N_2 \; (d\Phi/dt) \; = \; V_2. \tag{9.25}$$

and hence,

$$V_2 \; = \; V_1 \; (N_2/N_1). \tag{9.26}$$

Equations (9.24)-(9.26) indicate that energy exchange between the windings is through a changing magnetic flux and that there is a voltage step-up when $N_2 > N_1$. In the case of infinite L_1

the combination of Equations 9.24 and 9.26 gives the condition for conservation of energy,

$$V_1 i_1 = V_2 i_2. \tag{9.27}$$

When the secondary is connected to a load resistor R_2, the primary voltage is proportional to current via $V_1 = i_1 R_2 (N_1/N_2)^2$. Thus, when viewed from the primary, the circuit is that illustrated in Figure 9.7b with a transformed load resistance.

We have found voltage-current relationships for the two energy paths with the alternate path assumed to be an open circuit. The total circuit (Fig. 9.7c) is the parallel combination of the two. The model shown determines the primary current in terms of the input voltage when the secondary is connected to a resistive load. The input current is expended partly to produce magnetic field in the transformer (i_{leak}) with the remainder coupled to the secondary (i_{load}). The secondary voltage is given by Eq. (9.26). The secondary current is given by Eq. (9.27) with i_{load} substituted for i_1. The conclusion is that if the primary inductance is low, a significant fraction of the primary current flows in the reactance; therefore $i_1 > (N_2/N_1)\ i_1$.

The reactive current component is generally undesirable in a power circuit. The extra current increases resistive losses in the transformer windings and the ac voltage source. If the transformer is used to amplify the voltage of a square pulse from a pulsed voltage generator (a common accelerator application), then leakage currents contribute to droop of the output voltage waveform. Consider applying a square voltage pulse of duration Δt from a voltage generator with an output impedance $R_1 = R_2 (N_1/N_2)^2$. The equivalent circuit has resistance R_1 in series with the primary (Fig. 9.7d). We will see in Section 9.10 that this is a good model for the output of a charged transmission line. The output pulse shape is plotted in Figure 9.8 as a function of the ratio of the circuit time $L/[R_2(N_1/N_2)^2]$ to the pulselength Δt . The output pulse is a square pulse when $L/R_1 \gg \Delta t$. If this condition is not met, the pulse droops. Energy remains in transformer magnetic fields at the end of the main pulse; this energy appears as a negative post-pulse. Although no energy is lost in the ideal transformer, the negative post-pulse is generally useless. Therefore, pulse transformers with low primary inductance have poor energy transfer efficiency and a variable voltage output waveform. Drooping waveforms are often unacceptable for accelerator applications.

Leakage current is reduced by increasing the primary inductance. This is accomplished by constructing the toroidal mandrel from ferromagnetic material. The primary inductance is increased by a factor of μ/μ_0. Depending on the operating regime of the transformer, this factor may be as high as 10,000. Another way to understand the role of iron in a transformer is to note that a certain flux change is necessary to couple the primary voltage to the secondary. In an air core transformer, the flux change arises from the difference in the ampere turns between the primary and secondary; the flux change is generated by the leakage current. When a ferromagnetic material is added, atomic currents contribute to the flux change so that the leakage current can be much smaller.

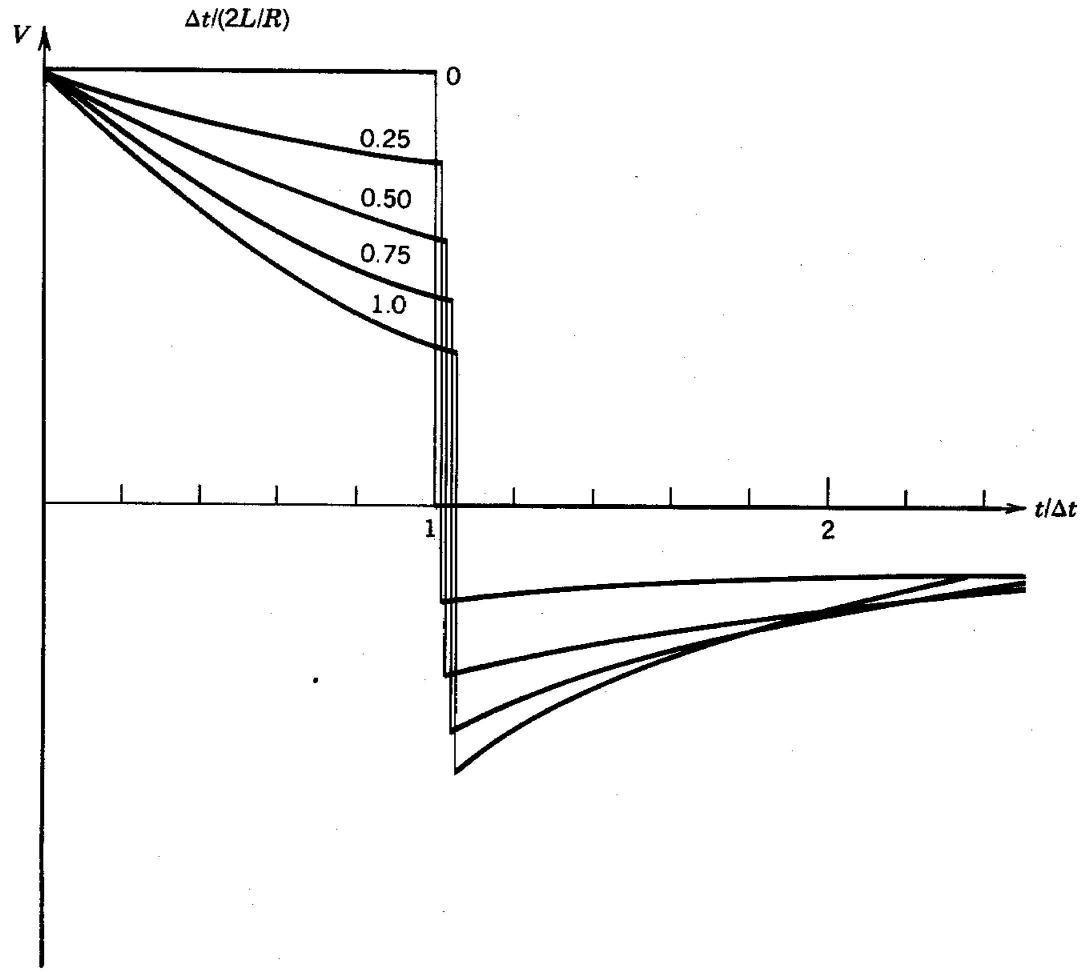

Figure 9.8 Pulse waveforms; resistive load driven by a matched pulse modulator through a transformer: Δt is the duration of the voltage pulse, R is the output impedance of the modulator and the load resistance viewed at the primary, and L is the primary shunt inductance.

The energy transfer efficiency of real transformers falls short of that for the ideal transformer of Figure 9.7c. One reason for power loss is that ferromagnetic materials are not ideal inductors. Eddy current losses and hysteresis losses in iron transformer cores for fast pulses are discussed in Section 10.2. Another problem is that ideal coupling between the primary and secondary cannot be achieved. There is a region between the windings in which there is magnetic field that is not canceled when both windings have the same ampere turns; the effect of this region is represented as a series inductance in the primary or secondary. Minimizing the effects of nonideal coupling is one of the motivations for using an iron core to increase the primary inductance of the transformer rather than simply increasing the number of turns in the pnmary and secondary windings of an air core transformer.

There are limitations on the primary voltage waveforms that can be handled by pulse transformers with ferromagnetic cores. The rate of change of flux enclosed by the primary is given by Eq. (9.25a). The flux enclosed in a transformer with a toroidal core area A_1 is $A_1B(t)$. Inserting this into Eq. (9.25a) and integrating, we find that

$$[B(t) - B(0)]\ N_1A_1 = \int V(t)dt. \tag{9.28}$$

Equation (9.28) constrains the input voltage in terms of the core geometry and magnetic properties of the core material. An input signal at high voltage or low frequency may drive the core to saturation. If saturation occurs, the primary inductance drops to the air core value. In this case, the primary impedance drops, terminating energy transfer to the load. Referring to the hysteresis curve of Figure 5.12, the maximum change in magnetic field is $2B_s$. If the primary input is an ac signal, $V_1(t) = V_0 \sin(2\pi ft)$, then Eq. (9.28) implies that

$$V_0/f\ (volt{-}s) \leq 2\pi N_1A_1B_s. \tag{9.29}$$

Transformers are usually run well below the limit of Eq. (9.29) to minimize hysteresis losses.

The basic circuit for a high-voltage dc supply is shown in Figure 9.9. The configuration is a *half-wave rectifier*; the diode is oriented to pass current only on the positive cycle of the transformer output. A capacitor is included to reduce ripple in the voltage. The fractional drop in voltage during the negative half-cycle is on, the order $(1/2f)/RC$, where R is the load resistance. Output voltage is controlled by a variable autotransformer in the primary.

Because of the core volume and insulation required, transformers are inconvenient to use at voltages above 100 kV. The ladder network illustrated in Figure 9.10a can supply voltages in the 1-MV range. It is the basis of the Cockcroft-Walton accelerator [J. D. Cockcroft and E. T. S. Walton, Proc. Roy. Soc. (London) **A136**, 619 (1932)] which is utilized as a preinjector for many

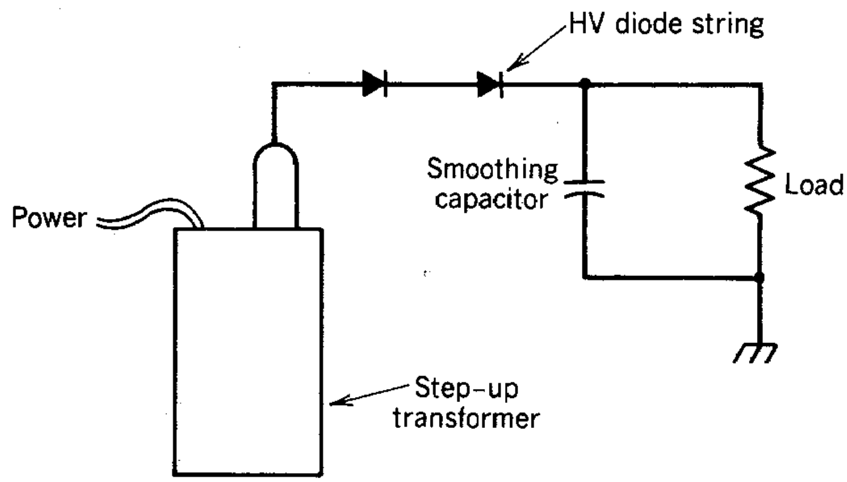

Figure 9.9 Half-wave-rectifier circuit to generate high-voltage dc power from a transformed ac waveform.

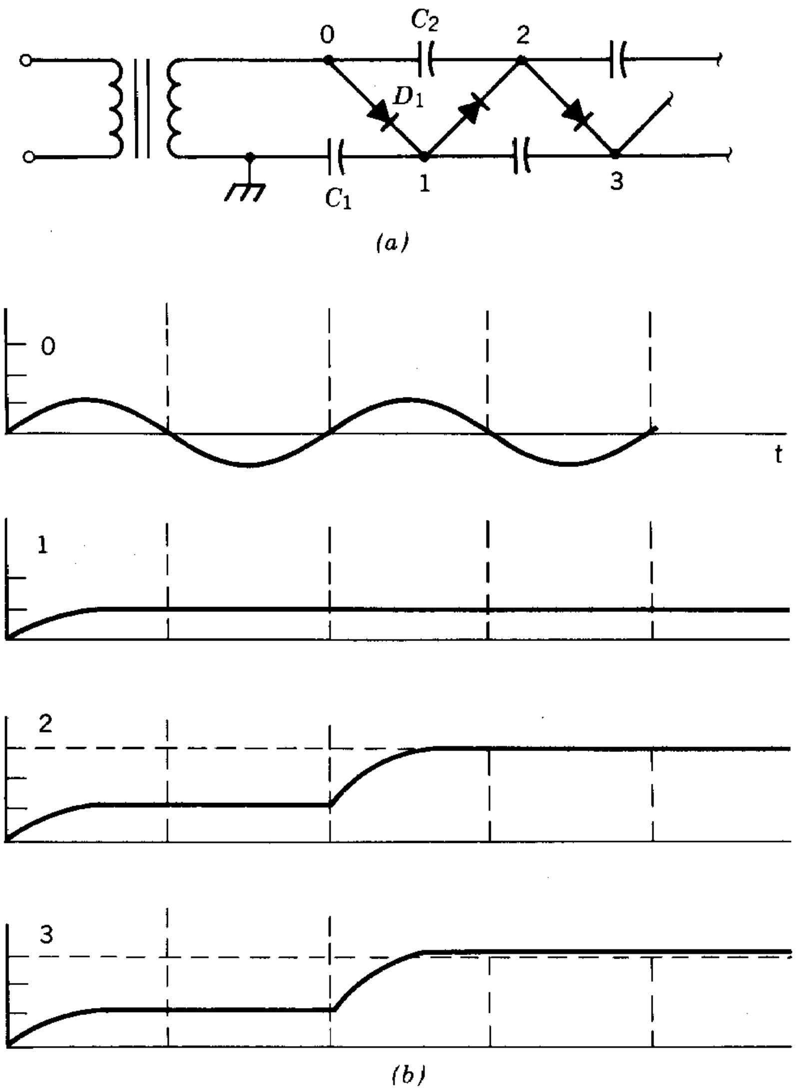

Figure 9.10 (*a*) Voltage multiplication ladder network (Cockcroft–Walton accelerator). (*b*) Ideal voltage waveforms (neglecting the ac generator impedance) shown at various points of the network.

high-energy accelerators. We can understand operation of the circuit by considering the voltage waveforms at the input (0) and, at the three points indicated in Figure 9.10b (1, 2, 3). The input voltage is a bipolar ac signal. In order to simplify the discussion, we assume an ideal ac voltage source that turns on instantaneously and can supply infinite current; in reality, a series resistor extends charging over many cycles to prevent damage to the transformer. On the first positive half-cycle, current flows through the diodes to charge all the points to $+V_o$. On the negative half-cycle, the voltage at point 1 is maintained positive because current cannot flow backward in diode D_1. The voltage at point 2 is maintained positive by conductance from C_1 to C_2 through diode D_2. At the time of maximum negative voltage at the input, there is a voltage difference greater than V_o across capacitor C_2. In the steady state, the voltage difference approaches $2V_o$. On the second positive cycle, the voltage at point 2 is boosted to $3V_o$. The voltage at point 3 also approaches $3V_o$ because of charging through D_3. The reasoning can be extended to higher points on the ladder, leading to the unloaded steady-state voltages indicated in Figure 9.10.

At the same voltage, a ladder network requires about the same number of diodes and capacitors as a power supply based on a transformer and rectifier stack. The main advantages of a ladder network is that it utilizes a smaller transformer core and it is easier to insulate. Insulation of the secondary of a transformer is difficult at high voltage because the secondary winding must encircle the transformer core. A large core must be used with oil-impregnated insulation. In contrast, the ladder network is extended in space with natural voltage grading along the column. It is possible to operate Cockcroft-Walton-type accelerators at megavolt levels with air insulation at atmospheric pressure by locating the capacitor-diode stack in a large shielded room.

9.3 INSULATION

Insulation is the prevention of current flow. It is the major technological problem of high-voltage electrostatic acceleration. At low values of electric field stress, current flow through materials such as glass, polyethylene, transformer oil, or dry air is negligible. Problems arise at high voltage because there is sufficient energy to induce ionization in materials. Portions of the material can be converted from a good insulator to a conducting ionized gas (plasma). When this happens, the high-voltage supply is shorted. Plasma breakdowns can occur in the solid, liquid, or gaseous insulation of high-voltage supplies and cables. Breakdown may also occur in vacuum along the surface of solid insulators. Vacuum breakdown is discussed in the Section 9.5.

There is no simple theory of breakdown in solids and liquids. Knowledge of insulating properties is mainly empirical. These properties vary considerably with the chemical purity and geometry of the insulating material. The *dielectric strength* and relative dielectric constant of insulators commonly used in high-voltage circuits are given in Table 9.1. The dielectric strength is the maximum electric field stress before breakdown. The actual breakdown level can differ considerably from those given; therefore, it is best to leave a wide safety factor in designing high-voltage components. The dielectric strength values of Table 9.1 hold for voltage pulses of submicrosecond duration. Steady-state values are tabulated in most physical handbooks.

Measurements show that for voltage pulses in the submicrosecond range the dielectric strength of liquids can be considerably higher than the dc value. The following empirical formulas describe breakdown levels in transformer oil and purified water [see R. B. Miller, **Intense Charged Particle Beams**, (Plenum, New York, 1982), 16] two media used extensively in high-power pulse modulators. The pulsed voltage dielectric strength of transformer oil is approximately

TABLE 9.1 Properties of Some Common Insulators[a]

Material	Relative Dielectric Constant ($\varepsilon/\varepsilon_0$)	Dielectric Strength (MV/cm)
Transformer oil	3.4	1
Mylar	3	1.8
Polyethylene	2.25	1.8
Teflon	2.1	4.3
Polycarbonate	2.96	5.5

[a]Adapted from J. F. Francis, *High Voltage Pulse Techniques*, Air Force Office of Scientific Research, AFOSR-74-2639-5, 1974.

$$E_{\max} \cong 0.5/t_p^{0.33} A^{0.1}. \tag{9.30}$$

The quantity E_{max} (in megavolts per centimeter) is the highest value of electric field in the insulator at the peak of the voltage pulse. The quantity t_p is the time during which the voltage is above 63% of the maximum value (in microseconds), and A is the surface area of the high voltage electrode in centimeters squared. The breakdown level of water has the same scaling as Eq. (9.30) but is polarity dependent. The dielectric strength of water for a negative high-voltage electrode is given by

$$E_{\max} \cong 0.6/t_p^{0.33} A^{0.1} \qquad (negative) \tag{9.31}$$

in the same units as Eq. (9.30). With a positive polarity, the breakdown level is approximately

$$E_{\max} \cong 0.3/t_p^{0.33} A^{0.1} \qquad (positive). \tag{9.32}$$

The polarity dependence of Eqs. (9.31) and (9.32) is important for designing optimum pulsed power systems. For example, a charged coaxial transmission line filled with water can store four times the electrostatic energy density if the center conductor is negative with respect to the outer conductor rather than positive.

The enhanced dielectric strength of liquids for fast pulsed voltages can be attributed to the finite time for a breakdown streamer to propagate through the medium to short the electrodes. Section

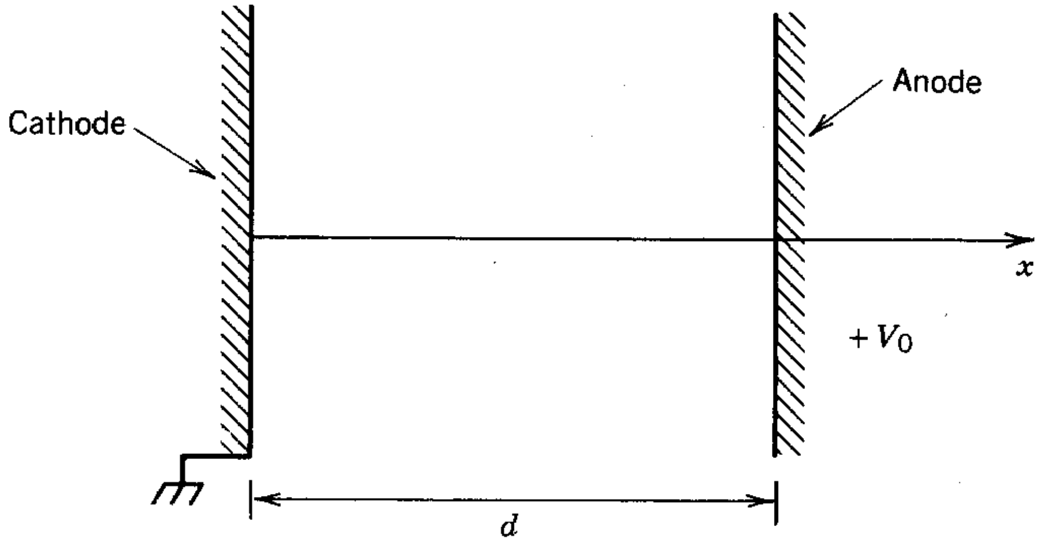

Figure 9.11 Gas-filled high-voltage gap, planar electrodes.

9.12 will show how pulse-charge overvolting is used to increase the electrostatic energy density of a pulse modulator for high output power. This process can be applied in liquid insulators because they are *self-healing*. On the other hand, the damage caused by streamers is cumulative in solids. Solid insulators cannot be used above the steadv-state levels.

Gas insulation is used in most steady-state high-voltage electrostatic accelerators. Gases have $\varepsilon/\varepsilon_0 \sim 1$; therefore, gas insulators do not store a high density of electrostatic energy. Gases, like liquids, are self-healing after spark breakdowns. The major advantage of gas insulationb is cleanliness. A fault, or leak in an accelerator column with oil insulation usually leads to a major cleanup operation. Although the gas itself is relatively inexpensive, the total gas insulation system is costly if the gas must be pressurized. Pressurization requires a large sealed vessel.

We shall study the theory of spark breakdown in gas in some detail. The topic is essential for the description of most types of fast high-voltage switches and it is relevant to insulation in most high-voltage electrostatic, accelerators. Consider the one-dimensional gas-filled voltage gap of Figure 9.11. The electrodes have separation *d* and the applied voltage is V_o. There is negligible transfer of charge between the electrodes when V_o is small. We will determine how a large interelectrode current can be initiated at high voltage.

Assume that a few electrons are produced on the negative electrode. They may be generated by photoemission accompanying cosmic ray or ultraviolet bombardment. The small source current density leaving the electrode is represented. by j_o. The electrons are accelerated by the applied field and move between the widely spaced gas molecules, as shown in Figure 9.12a. In a collision with a molecule, an electron is strongly deflected and much of its kinetic energy is absorbed. To construct a simple model, we assume that electrons are accelerated between molecules and lose all their directed energy in a collision. The parameter λ is the mean free path, the average distance between collisions. The mean free path is inversely proportional to the density of gas molecules. The density is, in turn, proportional to the pressure, *p*, so that $\lambda \sim 1/p$.

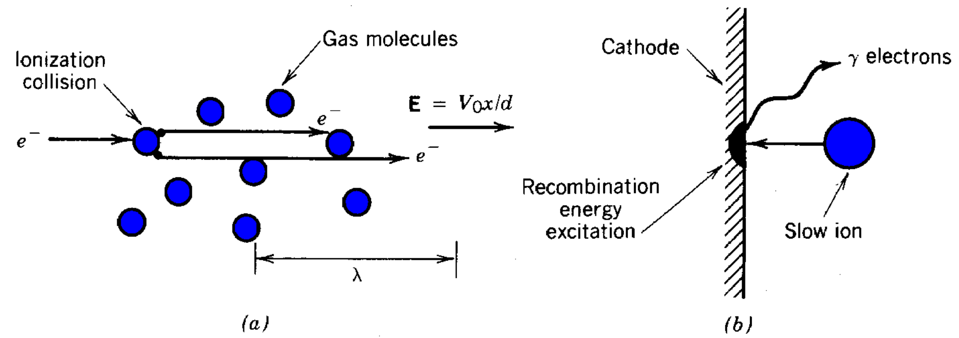

Figure 9.12 Processes in a gas-filled, high-voltage gap. (*a*) Electron migration in presence of a strong electric field showing electron acceleration, ionizing collision, and the mean free path. (*b*) Liberation of secondary electrons from a negative polarity electrode (cathode) by recombination of slow ions.

The average energy gained by an electron between collisions is

$$\Delta T = \lambda e E = \lambda e V_0/d. \tag{9.33}$$

An election may ionize a molecule in a collision if ΔT is high enough ($\Delta T > 30$ eV). In the ionization process, the excess kinetic energy of the electron drives an electron out of the molecule, leaving a positive ion. The two electrons move forward under the influence of the field, producing further electrons. The current density increases geometrically along the electron drift direction. The ions drift in the opposite direction and do not contribute to ionization in the gas. The motion of drifting ions is dominated by collisions; generally, they cannot reach high enough velocity to eject electrons in a collision with a molecule.

Electron multiplication in a gas with an applied electric field is characterized by α, the first Townsend coefficient [J. S. Townsend, *Electricity in Gases*, Phil. Trans. **A193**, 129 (1900)]. This parameter is defined by

$$\alpha = \frac{\textit{number of ionizations induced by an electron}}{\textit{cm of pathlength}} . \tag{9.34}$$

Consider an element of length Δx at the position x. The quantity $n(x)$ is the density of electrons at x. According to the definition of α, the total number of additional electrons produced in a volume with cross-sectional area dA and length Δx is

$$dN \cong \alpha\ n(x)\ dA\ \Delta x.$$

Dividing both sides of the equation by $dA\Delta x$, and taking the limit of small Δx, we find that

$$dn(x)/dx = \alpha\ n(x). \tag{9.35}$$

The solution of Eq. (9.35) implies an exponential electron density variation. Expressed in terms of the current density of electrons (assuming that the average electron drift velocity is independent of *x*), Eq. (9.35) implies that

$$j(x) = j_0 \exp(\alpha x). \tag{9.36}$$

if the negative electrode is located at x = 0. The current density arriving at the positive electrode is

$$j_a = j_0 \exp(\alpha d). \tag{9.37}$$

Although the amplification factor may be high, Eq. (9.37) does not imply that there is an insulation breakdown. The current terminates if the source term is removed. A breakdown occurs when current flow is self-sustaining, or independent of the assumed properties of the source. In the breakdown mode, the current density rapidly multiplies until the voltage supply is shorted (discharged). Ion interactions at the negative electrode introduce a mechanism by which a self-sustained discharge can be maintained. Although the positive ions do not gain enough energy to ionize gas molecules during their transit, they may generate electrons at the negative electrode through secondary emission (Fig. 9.12b). This process is parametrized by the secondary emission coeficient γ. The coefficient is high at hiph ion energy (> 100 keV). The large value of reflects the fact that ions have a short stoppmg range in solid matter and deposit their energy near the surface. Ions in a gas-filled gap have low average energy. The secondary-emission coefficient has a nonzero value for slow ions because there is available energy from recombination of the ion with an electron at the surface. The secondary emission coefficient for a zero-velocity ion is in the range $\gamma \approx 0.02$.

With ion interactions, the total electron current density leaving the negative electrode consists of the source term plus a contribution from secondary emission. We define the following current densities: j_o is the source, j_c is the net current density leaving the negative electrode, j_i is the ion current density arriving at the negative electrode, and j_a is the total electron flux arriving at the positive electrode. Each ionizing collision creates one electron and one ion. By conservation of charge, the ion current is given by

$$j_i = j_a - j_c, \tag{9.38}$$

Equation (9.38) states that ions and electrons leave, the gap at the same rate in the steady state. The portion of the electron current density from the negative electrode associated with secondary emission is thus,

$$j_c - j_o = \gamma\ (j_a - j_c). \tag{9.39}$$

Equation (9.39) implies that

$$j_c = (j_0 + \gamma j_a)/(1+\gamma). \tag{9.40}$$

By the definition of α

$$j_a = j_c \exp(\alpha d). \tag{9.41}$$

Combining Eqs. (9.40) and (9.41) gives

$$\frac{j_a}{j_o} = \frac{\exp(\alpha d)}{1 - \gamma\ [\exp(\alpha d) - 1]} . \tag{9.42}$$

Comparing Eq. (9.42) with (9.37), the effects of ion feedback appear in the denominator. The current density amplification becomes infinite when the denominator equals zero. When the conditions are such that the denominator of Eq. (9.42) is zero, a small charge at the negative electrode can initiate a self-sustained discharge. The discharge current grows rapidly over a time scale on the order of the ion drift time, heating and ionizing the gas. The end result is a *spark*. A spark is a high-current-density plasma channel. The condition for spark formation is

$$\exp(\alpha d) \le (1/\gamma) + 1 \cong 1/\gamma. \tag{9.43}$$

The discharge continues until the electrode voltage is depleted.

Calculation of the absolute value of α as a function of the gap parameters involves complex atomic physics. Instead, we will develop a simple scaling relationship for α as a function of gas pressure and electric field. Such a relationship helps to organize experimental data and predict breakdown properties in parameter regimes where data is unavailable. The ionization coefficient is proportional to the number of collisions between an electron and gas atoms per centimeter traveled, or $\alpha \sim 1/\lambda$. The ionization coefficient also depends on the average electron drift energy, Eλ. The ionization rate is proportional to the fraction of collisions in which an electron enters with kinetic energy greater than the ionization energy of the atom, *I*. The problem of a particle traveling through a random distribution of collision centers is treated in texts on nuclear physics. The familiar result is that the distance traveled between collisions is a random variable that follows a Poisson distribution, or

$$P(x) = \exp(-x/\lambda), \tag{9.44}$$

where λ is the mean free path. The energy of a colliding electron is, by definition, $T = xeV_o/d$. The fraction of collisions in which an electron has $T > I$ is given by the integral of Eq. (9.44) from x = Id/eV_o to ∞.

The result of these considerations is that α is well described by the scaling law

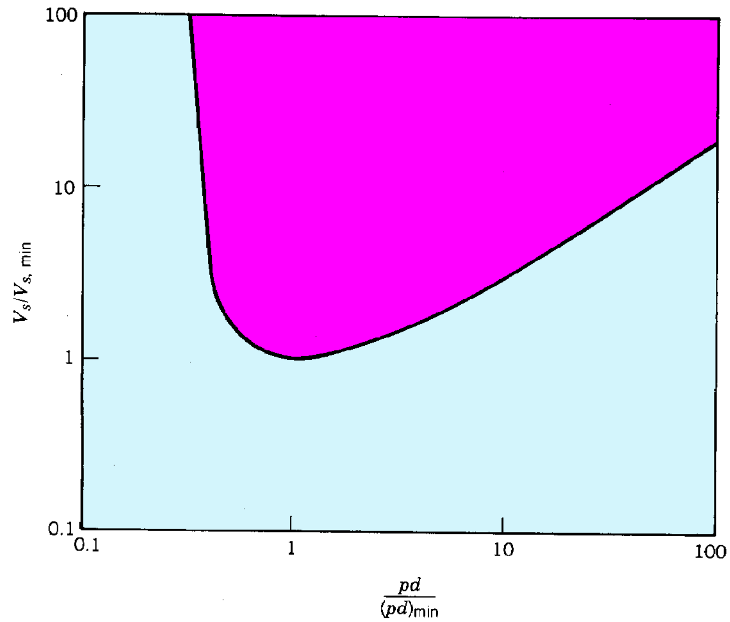

Figure 9.13 Normalized Paschen curve; sparking voltage versus the product of pressure and gap width.

$$\alpha = (A'/\lambda)\ \exp(-B'd/V_o\lambda) = (Ap)\ \exp(-Bpd/V_o). \tag{9.45}$$

The quantities *A* and *B* are determined from experiments or detailed collision theory The gap voltage for sparking is found by substituting Eq. (9.45) into (9.43):

$$\ln(1/\gamma) = (Apd)\ \exp(-Bpd/V_s).$$

Solving for V_s,

$$V_s = BPd\ /\ \ln\left(\frac{Apd}{\ln(1/\gamma)}\right)\ . \tag{9.46}$$

Equation. (9.46) is Paschen's law [F.Paschen, Wied. Ann. **37**, 69 (1889)] for gas breakdown. The sparking voltage is a function of the product *pd* and constants that depend on the gas properties. The values of *A* and *B* are relatively constant over a wide voltage range when the average electron energy is less than *I*. Furthermore, V_s is insensitive to γ; therefore, the results are almost independent of the electrode material.

Figure 9.13 is a normalized lot of V_s versus *pd.* The sparking voltage reaches a minimum value

TABLE 9.2 Minimum Sparking Constants[a]

Gas	$V_{s,\min}$ (V)	$(pd)_{\min}$ (torr-cm)
Air (dry)	327	0.567
A	137	0.9
H_2	273	1.15
He	156	4.0
CO_2	420	0.51
N_2	251	0.67
O_2	450	0.7

[a]Adapted from J. D. Cobine, *Gaseous Conductors*, Dover, New York, 1958, p. 164.

$V_{s,min}$ at a value $(pd)_{min}$. Voltage hold-off increases at both low and high values of *pd*. Voltage hold-off is high at low pd because there is a small probability that an electron will strike a molecule while traveling between electrodes. Paschen's law does not hold at very low vacuum because the assumption of a Poisson distribution of mean free paths is invalid.
At high values of *pd*, $V_s \sim (pd)$. In this regime, electrons undergo many collisions, but the mean free path is short. Few electrons gain enough energy to produce an ionization.

Equation (9.46) can be rewritten,

$$V_s = \frac{V_{s,\min}\ [pd/(pd)_{\min}]}{\ln[2.72\ pd/(pd)_{\min}]} \ . \tag{9.47}$$

Table 9.2 gives a table of spark parameters for some common gases. Note that the minimum sparking voltage is high for electronegative gases like oxygen and low for gases with little probability of electron capture like helium and argon. In electronegative gases, there is a high probability that electrons are captured to form negative ions. The heavy negative ions cannot produce further ionization, so that the electron is removed from the current multiplication process. The result is that gaps with electronegative-gases can sustain high voltage without breakdown. Sulfur hexafluoride an extremely electronegative gas, is often mixed with air or used alone to provide strong gas insulation at high pressure. The expense of the gas is offset by cost savings in the pressure vessel surrounding the high-voltage system. The addition of 8% (by volume) SF_6 to air increases V_s by a factor of 1.7. Pure SF_6 has V_s 2.2 times that of air for the same *pd*. Vacuum insulation is seldom used in power supplies and high-voltage generators because of technological difficulties in maintaining high vacuum and the possibility of long breakdown paths. Vacuum insulation in accelerator columns is discussed in Section 9.5.

Our discussion of gas breakdown has been limited to a one-dimensional geometry. Two-dimensional geometries are difficult to treat analytically because a variety of electron trajectories are possible and the electric field varies along the electron paths. Breakdown voltages,

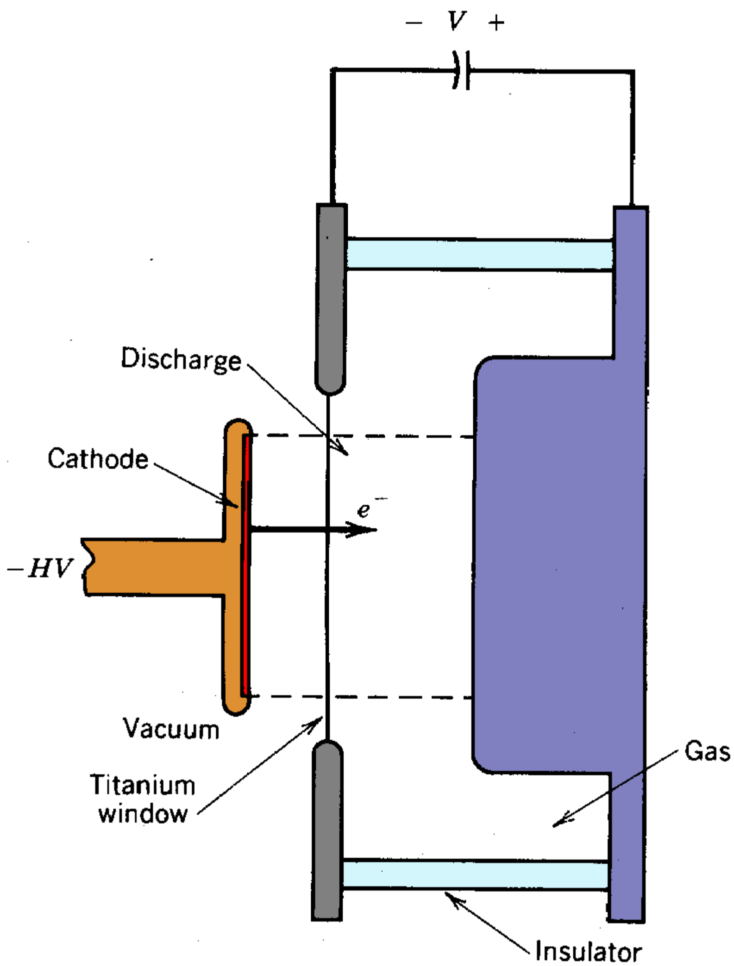

Figure 9.14 Electron-beam-controlled gas discharge laser.

are tabulated for special electrode geometries such as two spheres. In some circumstances (such as gas lasers), a stable, uniform discharge must be sustained over a large area, as shown in Figure 9.14. The interelectrode voltage must be less than V_s to prevent a localized spark; therefore, a source current is required to sustain the discharge. The source is often provided by injections of a high-energy electron beam through a foil on the negative electrode. Demands on the source are minimized if there is a large multiplication factor, exp(αd); therefore, the main gap is operated as close to V_s as possible. In this case, care must be taken with shaping of the electrodes. If the electrode has a simple radius (Fig. 9.15a), then the field stress is higher at the edges than in the body of the discharge, leading to sparks. The problem is solved by special shaping of the edges. Qne possibility is the Rogowski profile [W. Rogowski and H. Rengier, Arch. Elekt. **16**, 73 (1926)] illustrated in Figure 9.15b. This shape, derived by conformal mapping, has the property that the field stress on the electrodes decreases monotonically moving away from the axis of symmetry. The shape for two symmetric profiled electrodes is described by the parametric equations

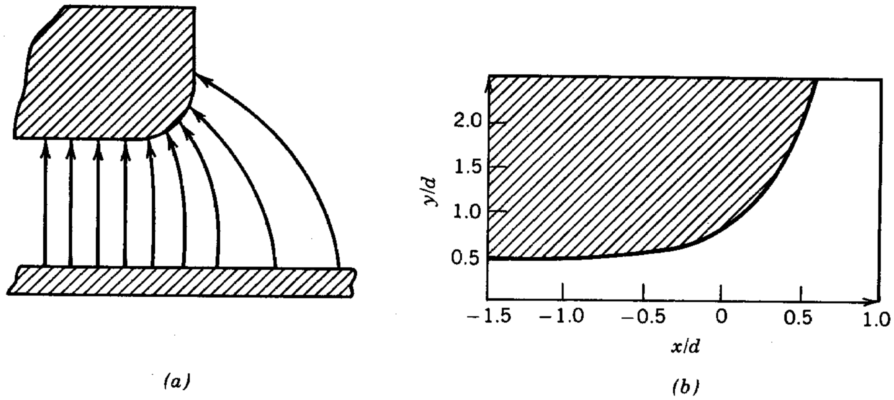

Figure 9.15 Electrode shaping. (*a*) Field enhancement at the edge of an electrode with a simple radius. (*b*) Electrode with a Rogowski profile.

$$x = d\varphi/\pi,$$
$$y = (d/\pi)\ [\pi/2 + \exp(\varphi)]. \tag{9.48}$$

where d is the minimum separation between electrodes. As indicated in Figure 9.15b, x is the transverse distance from the center of the electrodes, and $\pm y$ is the distance from the midplane (between electrodes) to the electrode surfaces.

Corona discharges appear in gases when electrodes have strong two-dimensional variations (Figure 9.16). Corona (crown in Latin) is a pattern of bright sparks near a pointed electrode. In such a region, the electric field is enhanced above the breakdown limit so that spark discharges occur. Taking the dimension of the corona region as d, the approximate condition for breakdown is

$$\overline{E}d_c \approx V_{s,\mathrm{min}}\ (pd_c/(pd)_{\mathrm{min}})\ /\ \ln[2.72(pd_c/(pd)_{\mathrm{min}})] \tag{9.49}$$

where $\overline{E}$ is the average electric field in the corona region. A self-sustained breakdown cannot be maintained by the low electric field in the bulk of the gap. Current in the low-field region is conducted by a Townsend (or dark) discharge, with the corona providing the source current j_o. The system is stabilized by the high resistivity of the dark discharge. A relatively constant current flows, even though the sparks of the corona fluctuate, extinguish, and reform rapidly. Inspection of Eq. (9.49) shows that for constant geometry, the size of the corona region grows with increasing electrode voltage. The voltage drop in the highly ionized corona is low; therefore, the voltage drop is concentrated in the dark discharge region. At some voltage, bulk breakdown occurs and the electrodes are shorted.

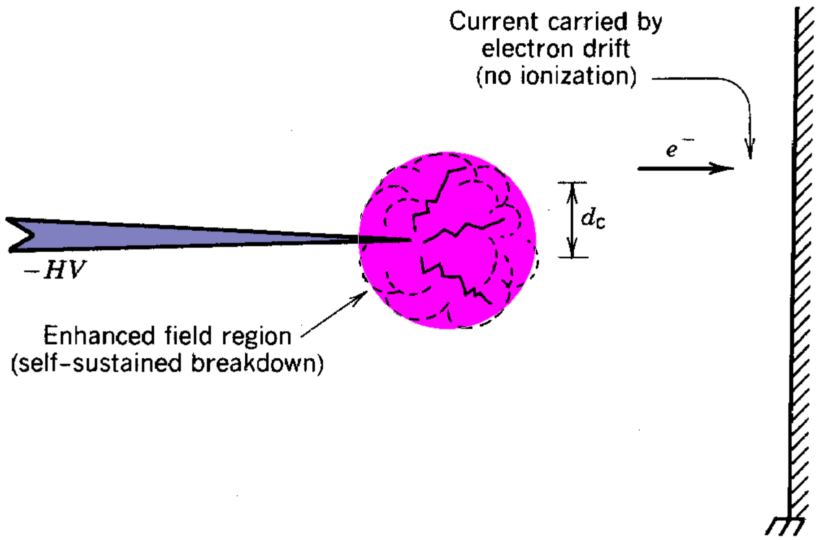

Figure 9.16 Physical basis for corona discharge near a pointed electrode.

9.4VAN DE GRAAFF ACCELERATOR

Two types of voltage generators are used for low current electrostatic accelerators in the megavolt range, the Cockcroft-Walton and Van de Graaff generators. We have already discussed the principle of the ladder network voltage used in the Cockcroft-Walton accelerator in Section 9.2. Cockcroft-Walton accelerators are used mainly for injectors with voltage of approximately 1 MV. In this section, we shall discuss the Van de Graaff generator, which can sustain steady-stale voltages up to 15 MV.

A Van de Graaf [R. J. Van de Graaff, Phys. Rev. **38**, 1919 (1931)] acelerator for electrons is illustrated in Figure 9.17. The principle of operation is easily understood. A corona discharge from an array of needles in gas is used as a convenient source of electrons. The electrons drift toward the positive electrode and are deposited on a moving belt. The belt composed of an insulating material with high dielectric strength, is immersed in insulating gas at high pressure. The attached charge is carried mechanically against the potential gradient into a high-voltage metal terminal. The terminal acts as a Faraday cage; there is no electric field inside the terminal other than that from the charge on the belt. The charge flows off the belt when it comes in contact with a metal brush and is deposited on the terminal.

The energy to charge the high-voltage terminal is supplied by the belt motor. The current available to drive a load (such as an accelerated beam) is controlled by either the corona discharge current or the belt speed. Typical currents are in the range of 10 µA. Power for ion sources or thermonic electron sources at high voltage can be supplied by a generator attached to the belt pulley inside the high-voltage terminal. The horizontal support of long belts and accelerator

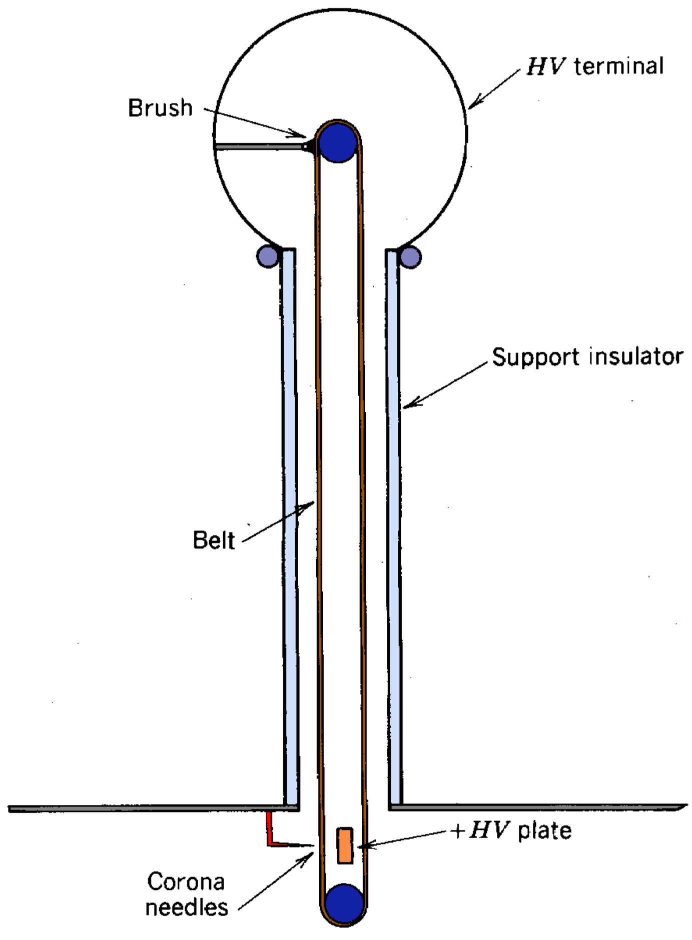

Figure 9.17 Van de Graaff accelerator. (*a*) Principle of operation. (*b*) Los Alamos National Laboratory, 7 MeV Van de Graaff accelerator, utilized as injector for 24.5 MeV tandem Van de Graaff accelerator facility. (Courtesy, J. R. Tesmer, Los Alamos National Laboratory.)

columns is difficult; therefore, many high-voltage Van de Graaff accelerators are constructed vertically, as in Figure 9.17.

Van de Graaff accelerators are excellent research tools because they provide a steady-state beam with good energy regulation. Continuous low-current beams are well suited to standard nuclear diagnostics that detect individual reaction products. Although the primary use of Van de Graaff accelerators has been in low-energy nuclear physics, they are finding increased use for high-energy electron microscopes and ion microprobes. The output beam energy of a Van de Graaff accelerator can be extended a factor of 2 (up to the 30 MeV range) through the tandem configuration illustrated in Figure 9.19. Negative ions produced by a source at ground potential are accelerated to a positive high-voltage terminal and pass through a stripping cell. Collisions in the cell remove electrons, and some of the initial negative ions are converted to positive ions. They are further

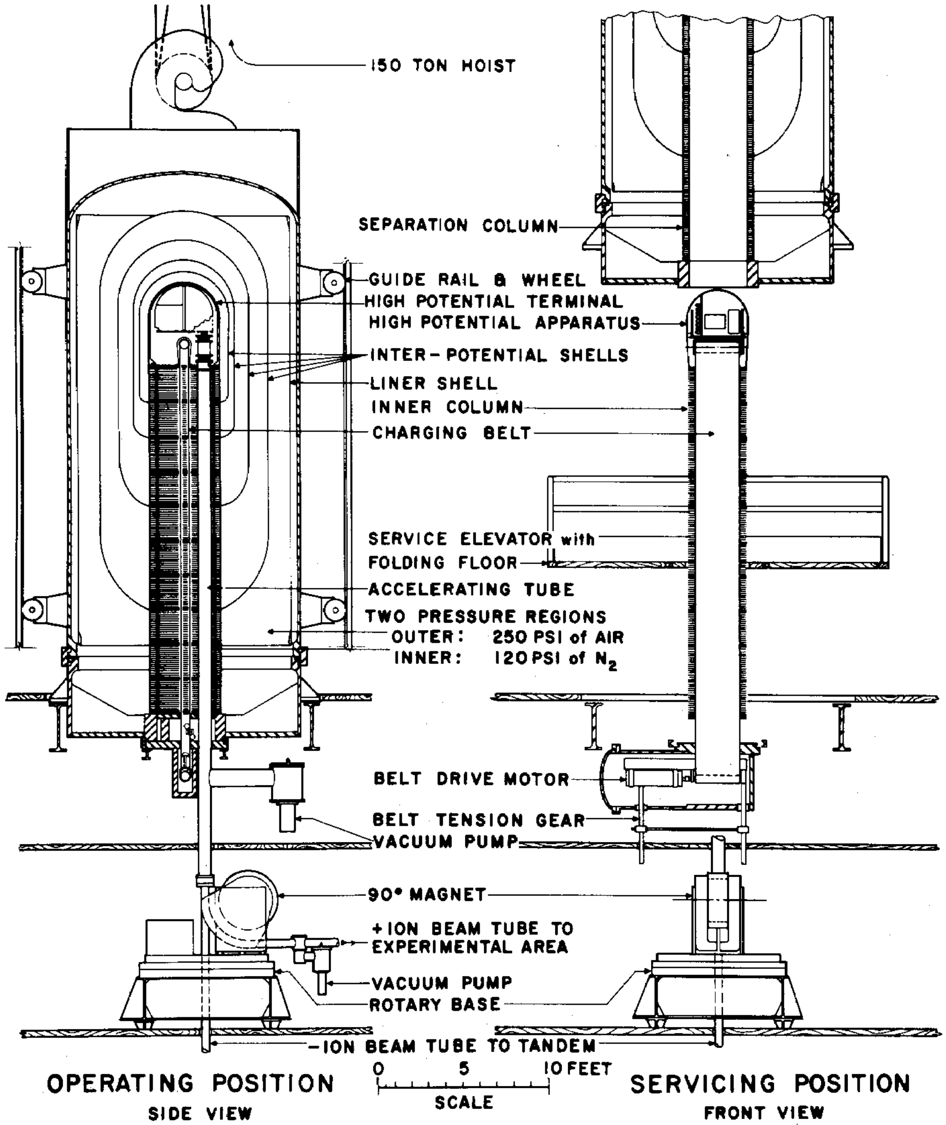

Figure 9.17 (*Continued*).

accelerated traveling from the high-voltage terminal back to ground.

Voltage hold-off is maximized when there are no regions of enhanced electric field. In other words, the electric field stress should be made as uniform as possible in the region of gas insulation. High-voltage terminals are usually constructed as large, smooth spheres to minimize peak electric field stress. We can show that, given the geometry of the surrounding grounded pressure vessel, there is an optimum size for the high-voltage terrminal. Consider the geometry of Figure 9.19a. The high-voltage terminal is a sphere of radius R_o inside a grounded sphere of radius R_2. Perturbing effects of the belt and accelerator column are not included. The solution to

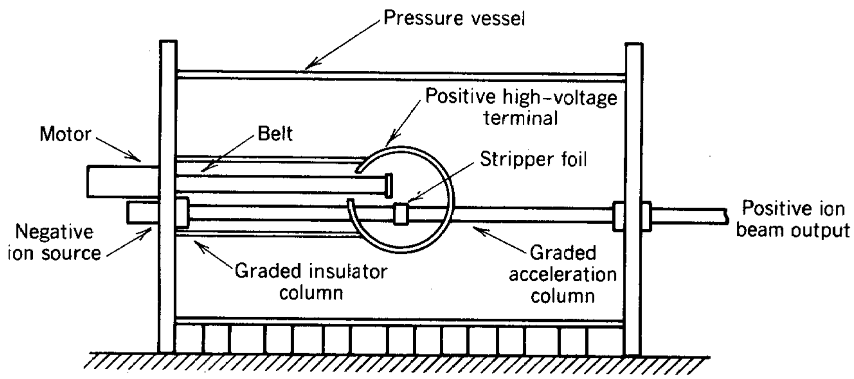

Figure 9.18 Schematic diagram of a tandem Van de Graaff accelerator.

the Laplace equation in spherical coordinates gives the radial variation of potential between the spheres

$$\varphi(r) = \frac{V_0 R_0 \; (R_2/r - 1)}{R_2 - R_0} . \tag{9.50}$$

Equation (9.50) satisfies the boundary conditions $\varphi(R_0) = V_0$ and $\varphi(R_2) = 0$. The radial electric field is

$$E_r(r) = -\partial\varphi/\partial r = \frac{V_0 R_0 \; (R_2/r^2)}{R_2 - R_0} . \tag{9.51}$$

The electric field is maximum on the inner sphere,

$$E_{r,\max} = \frac{(V_0/R_2) \; (R_2/R_0)}{1 - R_0/R_2} . \tag{9.52}$$

We assume R_2 is a fixed quantity, and determine the value of R_0/R_2 that will minimize the peak electric field. Setting $\partial E_{r,\max}/\partial(R_0/R_2) = 0$, we find that

$$R_0/R_2 = ½. \tag{9.53}$$

A similar calculation can be carried out for concentric cylinders. In this case, the optimum, ratio of inner to outer cylinder radii is

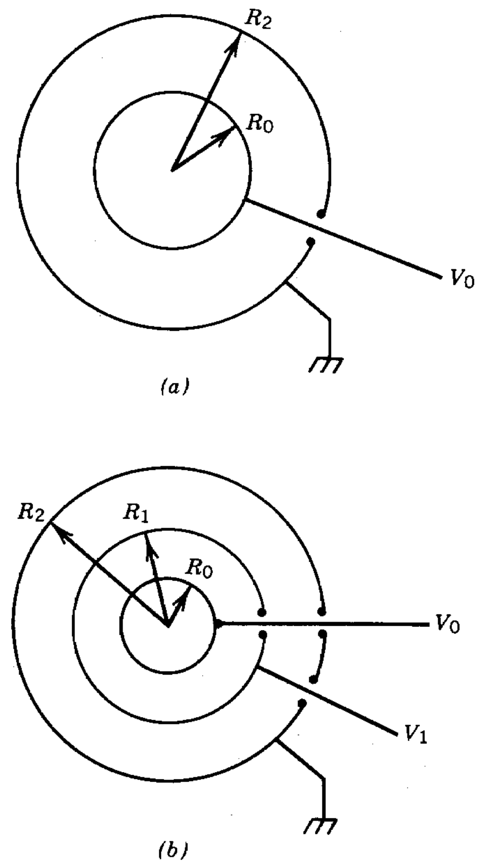

Figure 9.19 Geometry for calculating electric fields on spherical electrodes. (*a*) Two concentric spheres. (*b*) Concentric spheres with an equipotential shield.

$$R_0/R_2 = 1/e = 0.368. \tag{9.54}$$

A better electric field distribution can be obtained through the use of equipotential shields. Equipotential shields are biased electrodes located between the high-voltage terminal aid ground, as in Figure 9.17. Voltage on the shields is maintained at specific intermediate values by a high-voltage resistive divider circuit. The simplified geometry of three nested spheres (Fig. 9.19b) will help in understanding the principle of equipotential shields. The quantities R_2 and V_0 are constrained by the space available and the desired operating voltage. We are free to choose R_0, R_l, and V_1 (the potential of the shield) for optimum voltage hold-off. The electric fields on outer surfaces of the nested spheres, $E_1(r=R_1^+)$ and $E_0(r=R_0^+)$ are simultaneously minimized.

The fields on the outer surfaces of the electrodes are

$$E_0 = \frac{(V_0 - V_1)/R_0}{1 - R_0/R_1}, \tag{9.55}$$

$$E_1 = \frac{V - 1/R_1}{1 - R_1/R_1}. \tag{9.56}$$

The following equations are satisfied when the surface fields are minimized:

$$\Delta E_0 = (\partial E_0/\partial V_1)\ \Delta V_1 + (\partial E_0/\partial R_1)\ \Delta R_1 + (\partial E_0/\partial R_0)\ \Delta R_0 = 0, \tag{9.57}$$

$$\Delta E_1 = (\partial E_1/\partial V_1)\ \Delta V_1 + (\partial E_1/\partial R_1)\ \Delta R_1 + (\partial E_1/\partial R_0)\ \Delta R_0 = 0, \tag{9.58}$$

The final term in Eq. (9.58) is zero since there is no explicit dependence of E_1 on R_0. The previous study of two nested spheres implies that E_0 is minimized with the choice $R_0 = R_1/2$ given V_1 and R_1. In this case, the last term in Eq. (9.57) is independently equal to zero. In order to solve the reduced Eqs. (9.57) and (9.58), an additional equation is necessary to specify the relationship between ΔR_1 and ΔV_1. Such a relationship can be determined from Eqs. (9.55) and (9.56) with the choice $E_0 = E_l$. After evaluating the derivatives and substituting into Eqs. (9.57) and (9.58), the result is two simultaneous equations for R_1 and V_1. After considerable algebra, the optimum parameters are found to be

$$R_0 = R_1/2 \quad R_1 = 5R_2/8, \quad V_1 = 3V_0/5. \tag{9.59}$$

Addition of a third electrode lowers the maximum electric field stress in the system. To compare, the optimized two electrode solution (with $R_0 = R_2/2$) has

$$E_0 = 4V_0/R_2. \tag{9.60}$$

The peak field for the three electrode case is

$$E_0 = E_1 = (192/75)\ V_0/R_2 = 2.56\ V_0/R_2. \tag{9.61}$$

Larger numbers of nested shells reduce the peak field further. The intent is to counter the geometric variation of fields in spherical and cylindrical geometries to provide more uniform voltage grading. For a given terminal and pressure vessel size, multiple shells have approximately equal voltage increments if they are uniformly spaced.

9.5 VACUUM BREAKDOWN

A column for electron beam acceleration in an electrostatic accelerator is shown in Figure 7.14. It consists of insulating disks separated by metal grading rings. The disks and rings are sealed to hold high vacuum, either by low vapor pressure epoxy or by a direct metal to ceramic bond. We have already discussed the role grading rin s play in focusing particle beams through long columns (Section 7.7). We shall now consider how rings also improve the voltage hold-off capability of solid insulators in vacuum. High-vacuum sparking is determined by complex phenomena occurring on solid surfaces under high-field stress. Effects on both conductors and insulators can contribute to breakdown.

When a metal is exposed to a strong electric field, electrons may be produced by field emission. Field emission is a quantum mechanical tunneling process. Strong electric fields lower the energy barrier at the metal surface, resulting in electron emission. Field emission is described by the Fowler-Nordheim equation [see J. Thewlis (Ed.), **Encyclopaedic Dictionary of Physics, Vol. 3**, (Macmillan, New York, 1962), 120]. which has the scaling

$$j_{ef} \sim E^2 \exp(-B/E), \tag{9.62}$$

where E is the electric field. Typical current density predicted by Eq. (9.62) in a gap, with an electric field of 25 MV is on the order of 10 nA/cm^2.

Equation (9.62) implies that a plot of $\ln(j_{ef}/E^2)$ versus $1/E$ is a straight line. The scaling is observed in experiments on clean metal surfaces, but the slope of the plot indicates that the field magnitude on the surface is 10-100 times the macroscopic field (voltage divided by gap spacing). The discrepancy is explained by the presence of whiskers on the metal surface [see P. A. Chatterton, *Vacuum Breakdown*, in **Electrical Breakdown in Gases**, edited by J. M. Meek and J. D. Craggs (Wiley, New York, 1978)]. Whiskers are small-scale protrusions found on all ordinary metal surfaces. The electric field is enhanced near whiskers, as shown in Figure 9.20a. Although the high-field regions account for a small fraction of the surface area, there is a significant enhancement of emitted current because of the strong scaling of Eq. (9.62) with E.

The area-averaged whisker-enhanced current density from a metal surface at 10 MV/m is only 1-100 μA/cm^2. The leakage current by this process is not a significant concern in high-voltage systems. The main problem is that whiskers may be vaporized by the high-current density at the tips, ejecting bursts of material into highly stressed vacuum regions. Vaporization of even a small amount of solid material (at a density of 10^{22} cm^{-3}) on the tip of the whisker can eject a significant gas pulse into the vacuum. A conventional gas spark can then occur. Vaporization occurs at field stress exceeding 10 MV/m (100 kV/cm). kV/cm) for machined metal surfaces. The level can be increased by careful chemical preparation of the surface or by conditioning. In conditioning, a

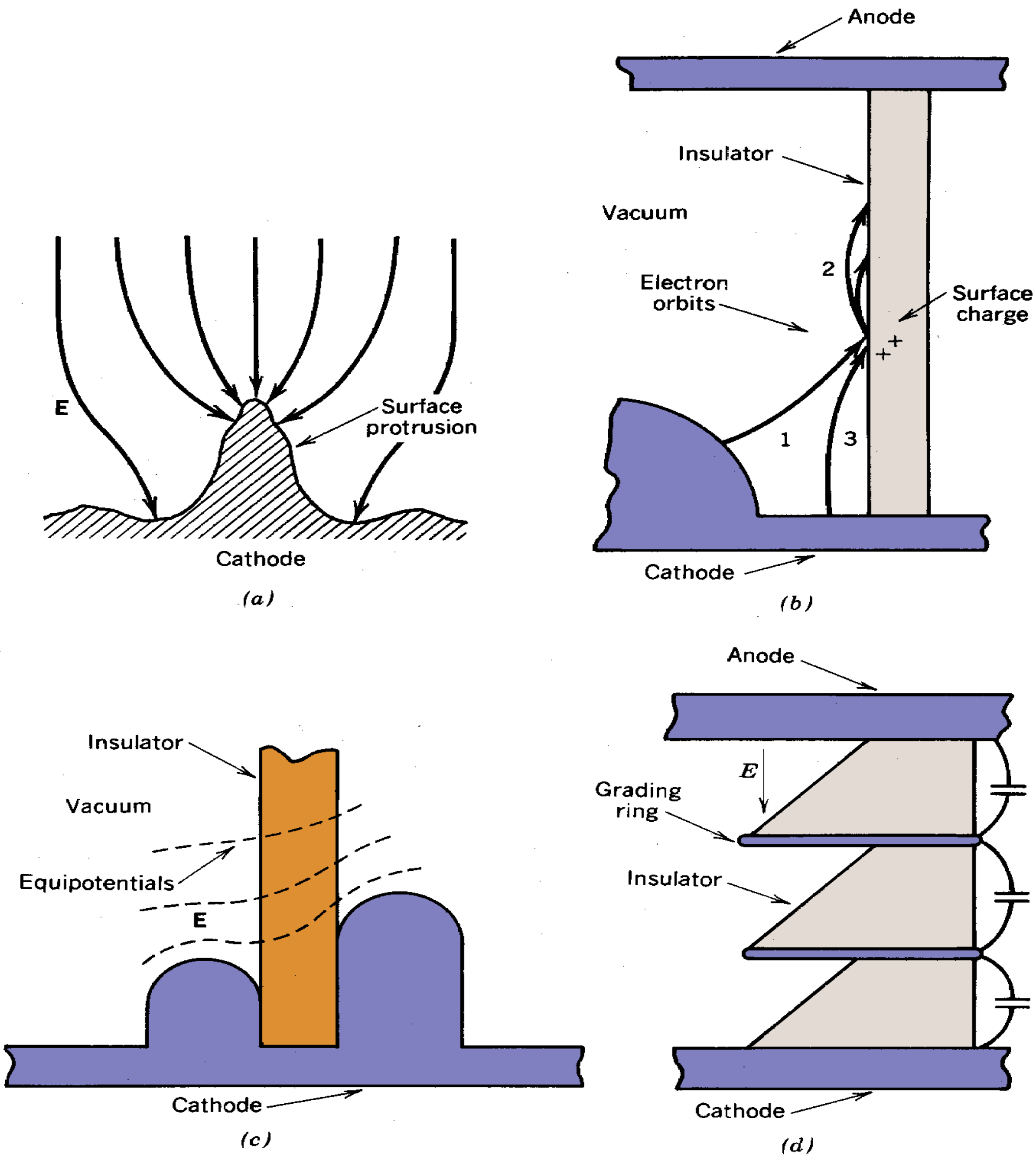

Figure 9.20 Processes influencing electric breakdowns in vacuum. (*a*) Microscopic view of surface of negative electrode showing field enhancement on tips of whiskers. (*b*) High-voltage electrodes separated by insulator; processes leading to insulator breakdown: (1) Electrons emitted from cathode (by field emission or whisker vaporization) collide with insulator surface. (2) If secondary emission coefficient exceeds unity, electrons are liberated. (3) Excess positive charge attracts other electrodes, increasing growth of surface charge. (*c*) Shielding triple point to prevent deposition of electrons emitted from negative electrode on insulator. (*d*) Common high-voltage insulator design, with insulator shaping (to minimize charge imbalance on surfaces) and grading rings.

metal surface is slowly raised to the final electric field operating level. Controlled vaporization of whiskers often smooths the surface, allowing higher operating field.

Whisker vaporization probably accounts for *microbursts* in steady-state electrostatic accelerators. Microbursts are random pulses of current observed in highly stressed accelerator columns. Whisker vaporizaton is used to advantage in pulsed electron accelerators. In this application, a rapidly pulsed electric field is applied to the cathode surface. Many whiskers vaporize simultaneously, covering the cathode with a dense, cold plasma. The plasma has zero work function; electrons can be extracted at current density exceeding 1 kA/cm^2. The main problem with *cold cathodes* is that the plasma expands into the acceleration gap (*plasma closure*), causing deterioration of the beam optics and ultimately shorting the gap. The expansion rate of the plasma, the *closure velocity*, is enhanced by electron flow through the plasma. Beam plasma instabilities rapidly beat the plasma. Closure velocities as high as 10 cm/μs have been observed. Depending on the acceleration gap width, cold cathodes are useful only for pulses in the 1-μs range.

Breakdowns occur on insulator surfaces in a vacuum at lower field levels than those that cause whisker vaporization on metals. Steady-state operating levels for insulators are in the 2 MV/m (20 kV/cm) range. Therefore, vacuum insulators are the weak point in any high-voltage electrostatic accelerator. The mechanisms of breakdown are not well understood. The following qualitative observations lead to useful procedures for optimizing insulator hold-off

1. There are two main differences between insulators and metals that affect vacuum breakdown. First, electric fields parallel to surfaces can exist near insulators. Second, regions of space charge can build up on insulators. These charges produce local distortions of electric fields.

2. A full-scale breakdown on an insulator is a complex process. Fortunately, it is usually sufficient to understand the low-current initiation processes that precede breakdown to predict failure levels.

3. Discharges on insulators are not initiated by whisker explosion because current cannot flow through the material. If the electric field is below the bulk dielectric strength of the insulator, discharge initiation is probably caused by processes on nearby metal surfaces.

4. When voltage pulses are short (< 50 ns), current flow from field emission on nearby electrodes is too small to cause serious charge accumulation on an insulator. In this case, the onset of insulator breakdown is probably associated with charge from whisker explosions on the metal electrodes. This is consistent with experiments; short-pulse breakdown levels on insulators between metal plates are in the 10-15 MV/m range.

5. Electrons produced in a whisker explosion move away from a metal electrode because the electric field is normal to the surface. In contrast, electrons can be accelerated parallel to the surface of an insulator. High-energy electrons striking the insulator can lead to

ejection of surface material. A microburst between metal electrodes in vacuum has a slow growth of discharge current (over many ion transit times) and may actually quench. In contrast, a discharge initiated along an insulator has a rapid growth of current and usually leads to a complete system short.

6. For long voltage pulses, field emission from nearby metal electrodes leads to accumulated space charge on insulator surfaces and field distortion (Fig.9.20b). Secondary emission coefficients on insulators are generally above unity in the energy range from 100 eV to a few keV. The impact of field-emitted electrons results in a net positive surface charge. This charge attracts more electrons, so that the electric field distortion increases. The nonuniform surface electric field fosters breakdown at levels well below that for whisker explosion on surrounding electrodes (~2 MV/m).

There are some steps that can be taken to maximize voltage hold-off along an insulator surface:

1. The *triple point* is the location where metal and insulator surfaces meet in a vacuum. In high-voltage pulsed systems, whisker explosions near the triple points at both ends of the insulator can spray charge on the insulator surface. Electrostatic shielding of the triple point to prevent whisker explosions, as shown in Figure 9.20c, improves voltage hold-off.

2. Electrons from whisker explosions are the most dangerous particles because they travel rapidly and have a secondary emission coefficient about two orders of magnitude higher than ions in the keV range. Voltage hold-off is high if the insulator is shaped so that electrons emitted from the negative electrode travel directly to the positive electrode without striking the insulator surface. A
common insulator configuration is illustrated in Figure 9.20d. Insulator sections with angled surfaces are separated by grading rings. With the angle shown, all electrons emitted from either metal or insulator surfaces are collected on the rings. The hold-off level in both pulsed and dc columns may be doubled with the proper choice of insulator angle. A graph of breakdown level for pulsed voltages as a function of insulator angle is shown in Figure 9.21.

3. Space-charge-induced field distortions in dc columns are minimized if the insulator is divided into a number of short sections separated by metal grading rings. The potential drop between rings is evenly distributed by a divider network outside the vacuum. Current flowing through the divider
relieves charge accumulate on the rings from field emission currents.

4. Many pulsed voltage insulating columns are constructed with grading rings in the configuration shown in Figure 9.20d,, although the utility of rings is uncertain. Capacitive grading is usually sufficient to prevent field distortion for fast pulses, especially if the medium outside the vacuum insulator has a high dielectric constant. Vacuum insulators in

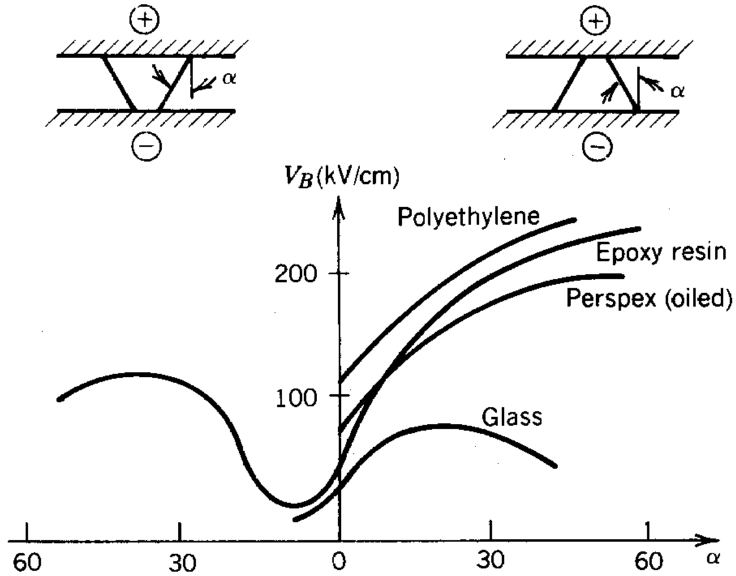

Figure 9.21 Insulator breakdown levels as function of insulator inclination angle for materials subject to fast voltage pulse (~ 30 ns). (Adapted from I. D. Smith, *Proc. First Int. Symp. Discharges and Elec. Insul. in Vac.*, MIT, Cambridge MA, 1964, p. 261.)

pulsed voltage systems usually have a breakdown level proportional to their length along the field.

Insulator hold-off in dc accelerator columns may be reduced with the introduction of a beam. Peripheral beam particles may strike the insulator directly or the beam may produce secondary particles. Beam induced ions are dangerous if they reach energy in the range > 100 keV. These ions have a high coefficient of secondary emission (> 10) and deposit large energy in a narrow layer near the surface when they collide with an insulator. Figure 9.22 illustrates a section of a Van de Graaff accelerator column designed to minimize insulator bombardment. Grading rings are closely spaced and extend inward a good distance for shielding. Furthermore, the gradient along the rings is purposely varied. As we saw in studying the paraxial ray equation (Section 7.5), variation of E_z has an electrostatic lens effect on low-energy particle orbits. Secondary electrons, ions, and negative ions are overfocused and collected on the rings before they are able to accelerate to high energy along the column.

9.6 LRC CIRCUITS

This section initiates our study of pulsed voltage generators. All pulsed voltage circuits have an energy storage element where electrical energy is contained in the form of electric or magnetic fields. The energy is transferred by a fast switch to a load. The speed of transfer (or the maximum

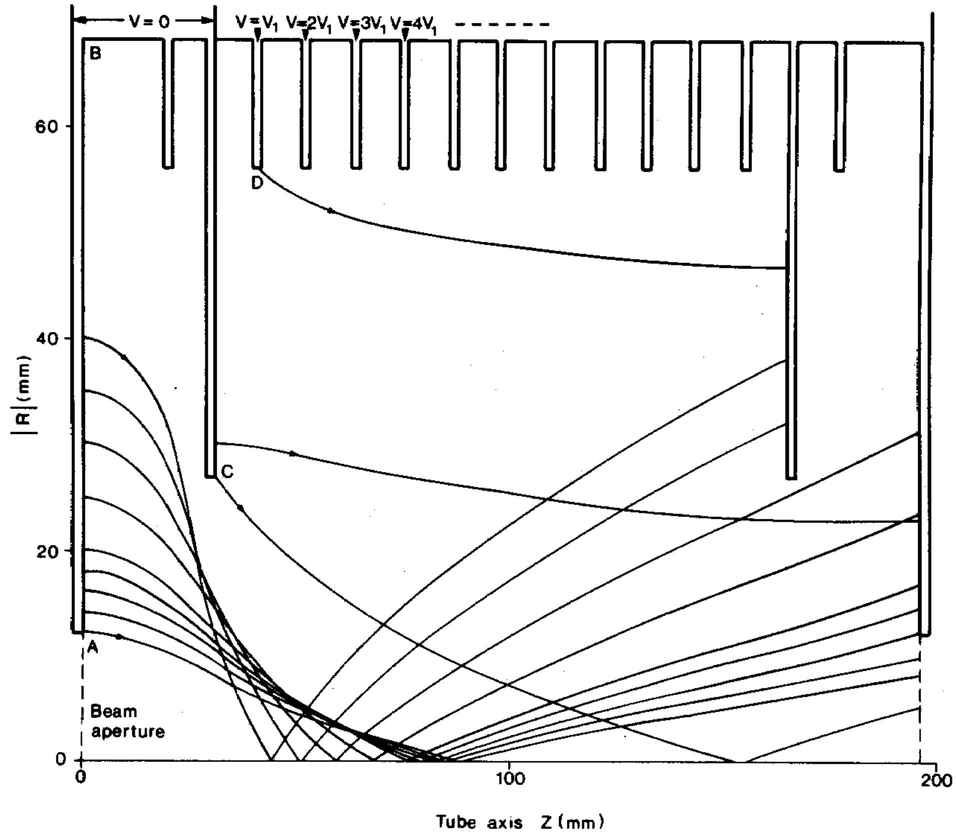

Figure 9.22 Insulator column for a Van de Graaff accelerator showing orbits of secondary ions liberated from electrodes. Variation of the grading ring spacing results in electrostatic overfocusing and radial loss of ions. (Courtesy T. Joy, Daresbury Laboratory.)

power attainable) is limited by parasitic inductance or capacitance in the circuit. The voltage pulse waveform is determined by the configuration of the energy storage element and the nature of the load. In the next sections we shall concentrate on simple resistive loads. The combination of energy storage element and switch is usually called a *voltage modulator*. The circuit produces a modulation, or variation in time, of the voltage.

There are four main accelerator applications of pulsed voltage circuits.

1. High electric field can often be sustained in small systems for short times because of time-dependent processes controlling breakdowns. Sparking on vacuum insulators is one example. Therefore, pulsed voltage modulators can be used to generate rapidly pulsed high-energy beams in compact systems.

2. Pulsed accelerators are often required for the study of fast physical processes. Applications include pulsed X-ray radiography, material response at high pressure and temperatures, and inertial fusion.

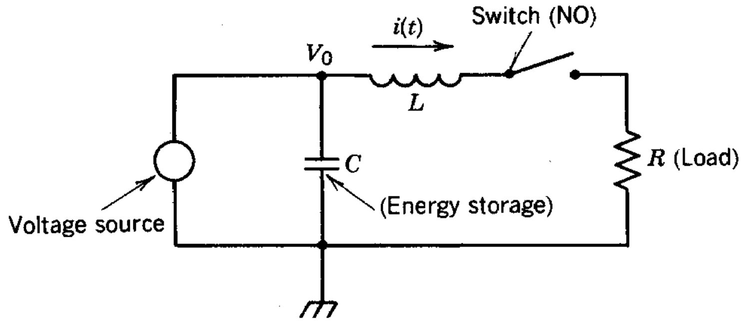

Figure 9.23 Pulse modulator with capacitive energy storage and closing switch.

3. Some beam applications require power at the multimegawatt level. Such systems are usually run at low-duty cycle. A system capable of supplying such power on a steady-state basis would require extensive ancillary power and cooling equipment. In contrast, a pulsed power modulator stores energy over a long time and releases it in a short pulse. This process is called *power compression*. High-energy electron linacs (Section 14.1) illustrate this process. Strong accelaccelerating gradient is obtained by injecting pulsed electromagnetic energy into a slow-wave structure. Klystron tubes powered by modulated dc generate the rf power.

4. Accelerators that utilize inductive isolation by ferromagnetic cores, such as the induction linac and the betatron, must operate in a pulsed mode.

The simplest electrical energy storage device. is a single capacitor. The voltage modulator of Figure 9.23 consists of a capacitor (charged to voltage V_0) and a shorting switch to transfer the energy. The energy is deposited in a load resistor, R. The flow of current involved in the transfer generates magnetic fields, so we must include the effect of a series inductance L in the circuit.

The time-dependent voltage across the circuit elements is related to the current by

$$V_C = -V_0 = \int i \; dt/C,$$

$$V_L = L \; di/dt.$$

$$V_R = iR.$$

Setting the loop voltage equal to zero gives

$$L \; (d^2i/dt^2) + R \; (di/dt) + i/C = 0. \qquad (9.63)$$

Equation (9.63) is solved with the boundary conditions $i(0+) = 0$ and $di/dt(0+) = V_0/L$, where $t = 0$ is the switching time. The second condition follows from the fact that immediately after switching

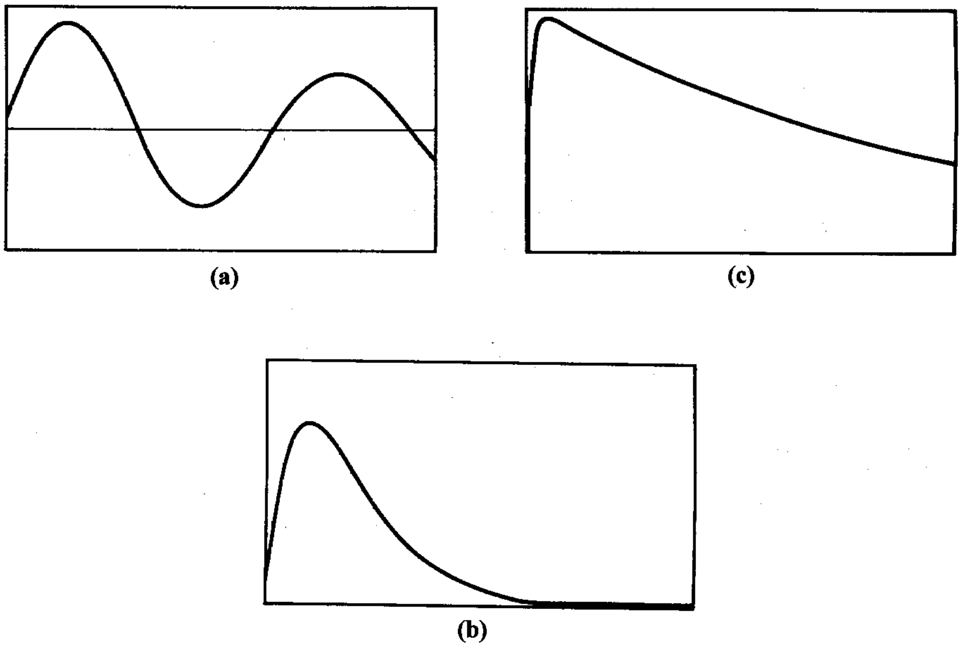

Figure 9.24 Voltage on a load driven by a switched capacitor with series inductance as a function of β/ω_0: L and C constant, load resistance (R) varied; $0 \leq \omega_0 t \leq 10$. ($a$) Underdamped circuit ($\beta/\omega_0 = 0.1$). ($b$) Critically damped circuit ($\beta/\omega_0 = 1$). (c) Overdamped circuit ($\beta/\omega_0 = 5$).

the total capacitor voltage appears across the inductor rather than the resistor (see Section 9.1).

The solution of Eq. (9.63) is usually written in three different forms, depending on the values of the following parameters:

$$\omega_0 = 1/\sqrt{LC}, \qquad (9.64)$$

$$\beta = R/2L, \qquad (9.65)$$

$$\omega_1 = \sqrt{\omega_0^2 - \beta^2},$$

$$\omega_2 = \sqrt{\beta^2 - \omega_0^2},$$

and

$$\delta = \tan^{-1}(\beta/\omega_1).$$

The solution with $\beta < \omega_0$ is illustrated in Figure 9.24a. The circuit behavior is oscillatory. Energy is transferred back and forth between the inductor and capacitor at approximately the characteristic frequency, ω_0. There is a small energy loss each oscillation, determined by the damping parameter

The circuit is *underdamped*. We shall study the underdamped LRC circuit in more detail when we consider rf accelerators. The time dependent current is

$$i(t) = (CV_0/\cos\delta)\ \exp(-\beta t)\ [\omega_1\ \sin(\omega_1 t-\delta) + \beta\ \cos(\omega_1 t-\delta)]$$
$$\cong CV_0\omega_0\ \exp(-\beta t)\ \sin\omega_0 t) \qquad (\beta \ll \omega_0). \tag{9.66}$$

The voltage on the load resistor is *i(t)R*.

The opposite extreme, *overdamping*, occurs when $\beta > \omega_0$. As indicated in Figure 9.24b, the circuit is dominated by the resistance and does not oscillate. The monopolar voltage pulse on the load rises in a time of approximately *L/R* and decays exponentially over a time *RC*. The current following switching in an overdamped circuit is

$$i(t) = [CV_0\ (\beta^2-\omega_2^2)/2\omega_2]\ [\exp(\omega_2 t) - \exp(-\omega_2 t)]\ \exp(-\beta t). \tag{9.67}$$

An LRC circuit is critically damped when $\beta = \omega_0$ or

$$R_c = 2\ \sqrt{L/C}. \tag{9.68}$$

The current for a critically damped circuit is

$$i(t) = \beta CV_0\ (\beta t)\ \exp(-\beta t). \tag{9.69}$$

The time-dependent load voltage is plotted in Figure 9.24c.

The waveforms in Figures 9.24a, b, and c have the same values of *L* and *C* with different choices of *R*. Note that the transfer of energy from the capacitor to the load resistor is accomplished most rapidly for the critically damped circuit. Thus, the power extracted from a pulsed voltage modulator is maximum when $R = R_c$. The quantity $2\ \sqrt{L/C}$, which has units of ohms, is called the characteristic impedance of the voltage modulator. Energy transfer is optimized when the load resistance is matched to the modulator impedance, as specified by Eq. (9.68). The peak power flow in a critically damped circuit occurs at a time $t = 1/\beta$. The maximum voltage at this time is $V_{max} = 0.736V_0$, the maximum current is $0.368V_0/\sqrt{L/C}$, and the maximum power in the load is $0.271V_0^2/\sqrt{L/C}$. The maximum power from this simple pulsed power generator is limited by the parasitic inductance of the circuit.

It is possible, in principle, to use an inductor for energy storage in a pulsed power circuit. A magnetic energy storage circuit is illustrated in Figure 9.25. In this case, a normally closed switch must be opened to transfer the energy to a load. We could also include the effects of parasitic capacitance in the circuit. Charging of this capacitance limits the current risetime in the load, analogous to the inductance in the capacitive storage circuit. The main advantage of magnetic

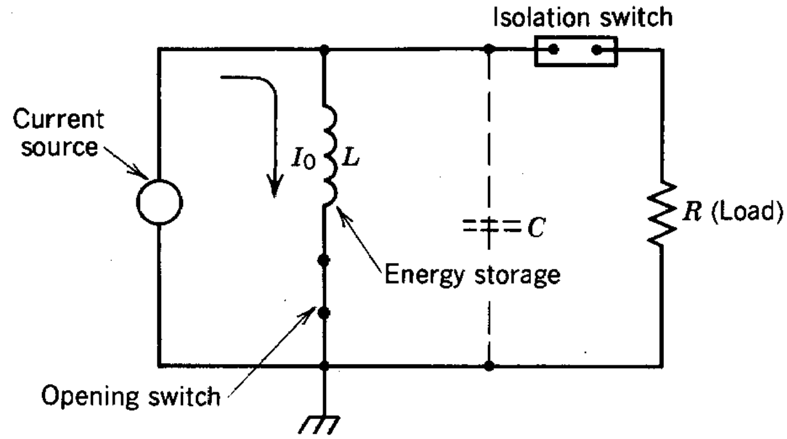

Figure 9.25 Pulse modulator with inductive energy storage and opening switch.

energy storage for, pulsed power applications is that a much higher energy density can be stored. Consider, for instance, a Mylar insulated capacitor with $\varepsilon/\varepsilon_0 \cong 3$ and a field stress of 200 kV/cm. Applying Eq. (5.19), the electrical energy density is only 10^4 J/m^3 (0.01 J/cm^3). In contrast, the energy density in a vacuum inductor with a field of 2 T (20 kG) is 1.6×10^6 J/m^3 (1.6 J/cm^3). The reason magnetic storage is not regularly used is the lack of a suitable fast opening switch. It is relatively easy to make a fast closing switch that conducts no current until a self-sustained discharge is initiated, but it is difficult to interrupt a large current and hold off the subsequent inductive voltage spike.

9.7 IMPULSE GENERATORS

The single-capacitor modulator is suitable for voltages less than 100 kV, but is seldom used at higher voltages. Transformer-based power supplies for direct charging are very large above 100 kV. Furthermore, it is difficult to obtain commercial high -energy-density capacitors at high voltage. Impulse generators are usually used for pulsed high voltage in the 0.1-10 MV range. These generators consist of a number of capacitors charged in parallel to moderate voltage levels (~50 kV). The capacitors are switched to a series configuration by simultaneously triggered shorting switches. The voltages of the capacitors add in the series configuration.

We will consider two widely used circuits, the *Marx generator* [E. Marx, Electrotech. Z. **45**,652 (1925)] and the *LC generator*. Impulse generators that produce submicrosecond pulses require less insulation than a single capacitor with a steady-state charge at the full output voltage. The peak voltage is applied for only a short time, and breakdown paths do not have time to form in the liquid or gas insulation. High-field stress means that compact systems can be designed. Small systems have lower parasitic inductance and can therefore achieve higher output power.

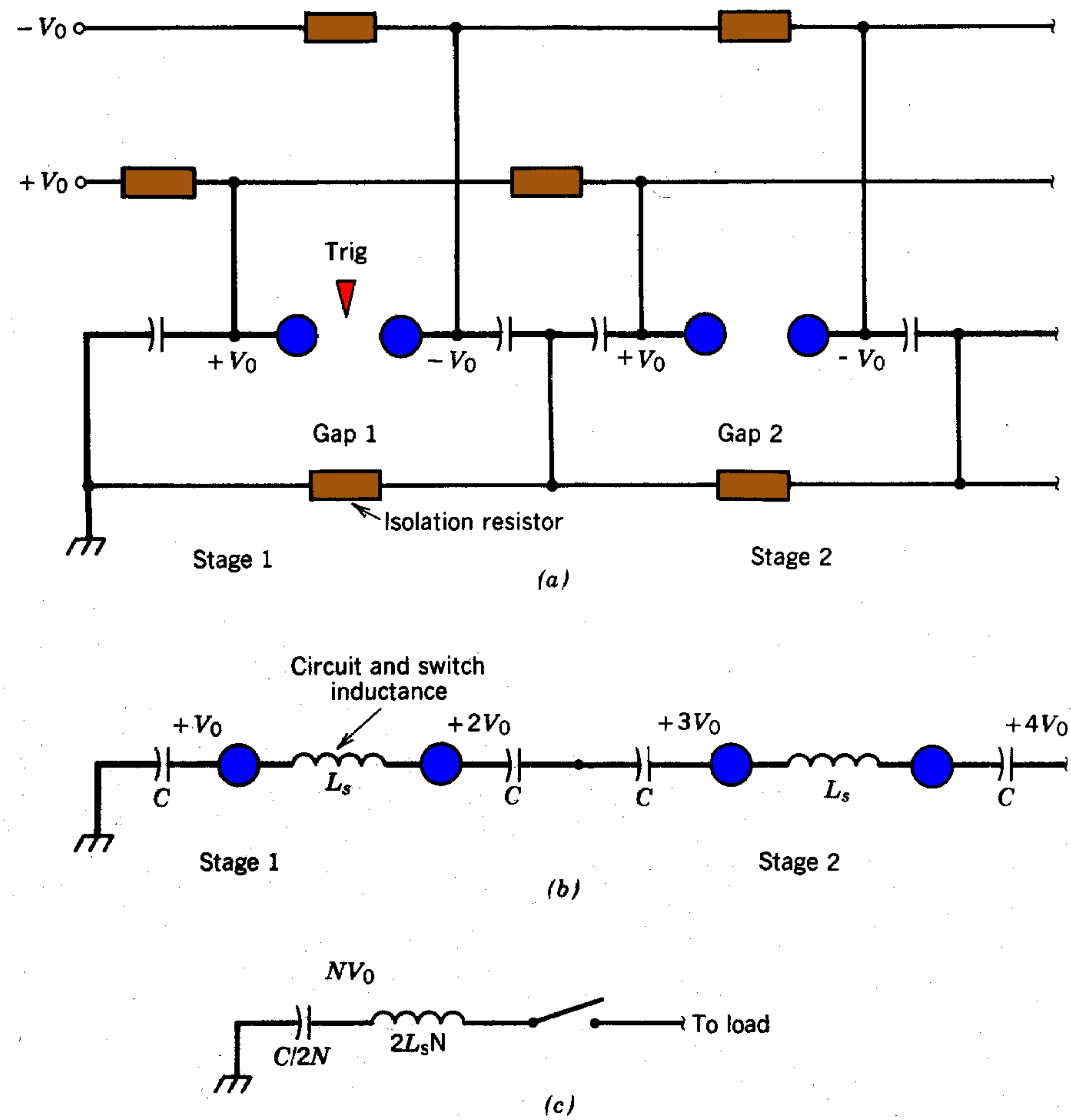

Figure 9.26 Marx generator. (*a*) Complete circuit diagram of a typical Marx generator showing charging lines. (*b*) Circuit model applicable for fast energy transfer following switching. (*c*) Simple lumped element circuit model for fast energy transfer neglecting electromagnetic wave phenomena.

A typical configuration for a Marx generator is illustrated in Figure 9.26. Positive and negative power supplies ($\pm V_0$) are used, charging the capacitors as shown in Figure 9.26a. Charging current is carried to the capacitors through isolation resistors (or inductors) that act as open circuits during the fast output pulse. The capacitor stack is interrupted by high-voltage shorting switches. Gas-filled distortion spark gaps are ideal for this application. The trigger enters at the midplane of the switch and is referenced to dc ground.

The circuit configuration immediately after switch shorting is shown in Figure 9.26b. The voltage across the load rapidly increases from 0 to $2NV_0$, where N is the number of switches and V_0 is the magnitude of charge voltage on each capacitor. The series inductance shown arises mainly from the narrow discharge channels in the spark gaps. If we ignore voltage variations on time scales less than the dimension of the generator divided by the speed of light in the insulating medium, the inductances and capacitors can be lumped together as shown in Figure 9.26c. The Marx generator in the high-voltage phase is equivalent to the single capacitor modulator. Output to a resistive load is described by the equations of Section 9.6.

The total series inductance is proportional to the number of switches, while the series capacitance is $C_0/2N$. Therefore, the characteristic generator impedance is proportional to N. This implies that it is difficult to design high-voltage Marx generators with low characteristic impedance. High-energy density capacitors and short connections help lower the inductance, but the main limitation arises from the fact that the discharge current must flow through the inductive spark gap switches.

One favorable feature of the Marx generator is that it is unnecessary to trigger all the switches actively. If some of the spark gaps at the low-voltage end of the stack are shorted, there is overvoltage on the remaining gaps. Furthermore, the trigger electrodes of the spark gaps can. be connected by circuit elements so that a trigger wave propagates rapidly through the generator. Using these techniques, pulsed voltages exceeding 10 MV have been generated in Marx generators with over 100 synchronous switches.

The LC generator, illustrated in Figure 9.27, is more difficult to trigger than the Marx generator, but it has lower characteristic impedance for the same output voltage. As in the Marx generator, a stack of capacitors is charged slowly in a parallel configuration by a positive-negative voltage supply (Fig. 9/27a). The main difference is that the switches are external to the main power flow circuit. Transition from a parallel to a series configuration is accomplished in the following way. Half of the capacitors are connected to external switched circuits with a series inductance. When the switches are triggered, each LC circuit begins a harmonic oscillation. After one half-cycle, the polarity on the switched capacitors is reversed. At this time, the voltages of all capacitors add in series, as shown in Figure 9.27b. The voltage at the output varies as

$$V_{out} = (2NV_0)\ [1 - \cos(\sqrt{2/lc}\ t)]. \tag{9.70}$$

where C is the capacitance of a single capacitor, N is the number of switches, and V_0 is the magnitude of the charge voltage.

The load must be isolated from the generator by a high-voltage switch during the mode change from parallel to series. The isolation switch is usually a low-inductance spark gap. It can be actively triggered or it can be adjusted for self-breakdown near the peak output voltage. Energy transfer to the load should take place at $t = \sqrt{LC/2}$ so that no energy remains in the external inductors. The transfer must be rapid compared to the mode change time or energy will return to

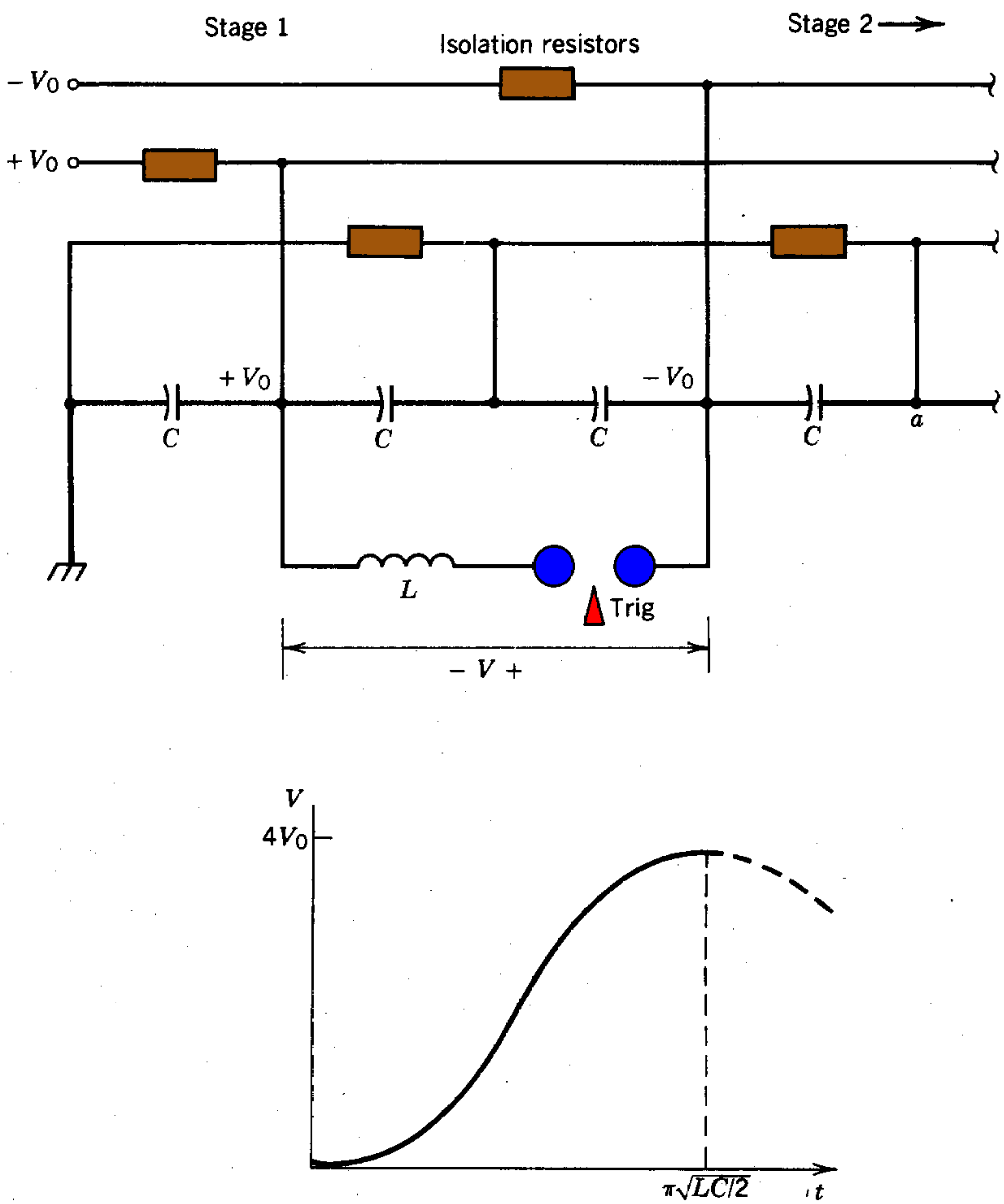

Figure 9.27 Circuit diagram of a typical *LC* generator, showing voltage at point *a* following switching through the external inductor.

the inductors, reducing the generator efficiency. Typically, an *LC* generator may have a mode change time of 6 μs and a transfer time to the load of 0.3 μs.

The equivalent circuit for the LC generator in the series state is the same as that for the Marx generator (Fig. 9.26c). The main difference is that the series inductances are reduced by elimination of the switches. The main disadvantages of the LC generator compared to the Marx generator are that the switching sequence is more complex, a low-inductance output switch is required, and the circuit remains at high voltage for a longer time. Triggering one reversmg circuit does not result in an overvoltage on the spark gaps of other sections. Therefore, all the switches in an LC generator must be actively fired with strong, synchronized trigger pulses.

9.8 TRANSMISSION LINE EQUATIONS IN THE TIME DOMAIN

Most accelerator applications for pulse modulators require a constant-voltage pulse. The critically damped waveform is the closest a modulator with a single capacitor and inductor can approach constant voltage. Better waveforms can be generated by modulators with multiple elements. Such circuits are called *pulse-forming networks* (PFNs). The transmission line is the continuous limit of a PFN. We shall approach the analysis of transmission lines in this section by a lumped element description rather than the direct solution of the Maxwell equations. Application of transmission lines as modulators is discussed in the following section. Discrete element PFNs are treated in Section 9.11.

We will derive the transmission line equations in the time domain. The goal is to find total voltage and current on the line as functions of time and position in response to specified inputs. The input functions have arbitrary time dependence, and may contain a number of frequency components. The frequency-domain analysis will be used in the study of rf accelerators which operate at a single frequency (Section 12.6). In the frequency-domain analysis, each harmonic component is treated separately. Voltage and current along the transmission line are described by algebraic equations instead of differential equations.

We will concentrate on the coaxial transmission line, illustrated in Figure 9.28. Properties of other common geometries are listed in Table 9.3. The coaxial line consists of an inner conducting

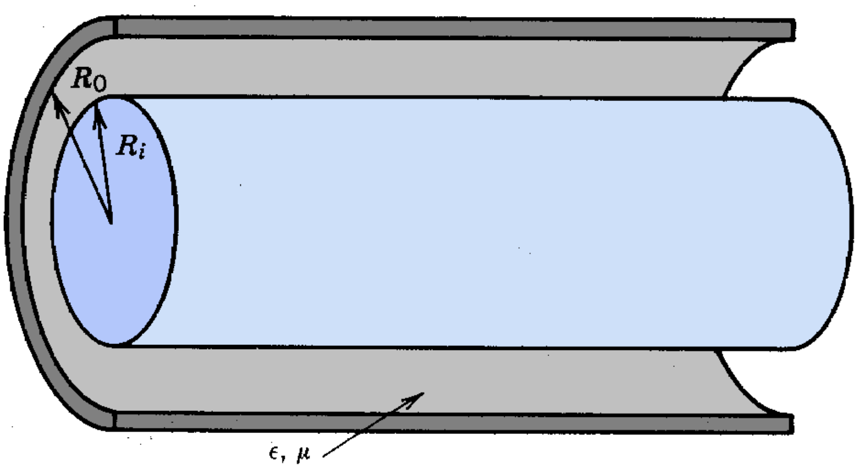

Figure 9.28 Section of a coaxial transmission line.

TABLE 9.3 Properties of Common Transmission Lines, TEM Modes[a]

1 Coaxial transmission line:

$$\mathscr{C} = 2\pi\varepsilon/\ln(R_0/R_i)$$
$$\mathscr{L} = (\mu/2\pi)\ln(R_0/R_i)$$
$$Z_0 = (\sqrt{\mu/\varepsilon}/2\pi)\ln(R_0/R_i)$$

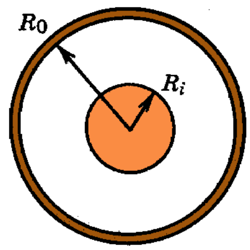

2 Two-wire transmission line

$$\mathscr{C} = \pi\varepsilon/\cosh^{-1}(D/d)$$
$$\mathscr{L} = \mu/\pi \cosh^{-1}(D/d)$$
$$Z_0 = (\sqrt{\mu/\varepsilon}/\pi)\cosh^{-1}(D/d)$$

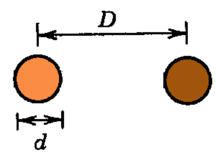

3 Isolated parallel plates ($d \ll D$)

$$\mathscr{C} = \varepsilon D/d$$
$$\mathscr{L} = \mu d/D$$
$$Z_0 = \sqrt{\mu/\varepsilon}(d/D)$$

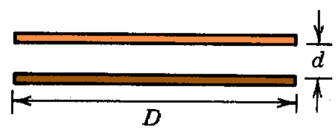

4 Stripline ($d \ll D$)

$$\mathscr{C} = 2\varepsilon D/d$$
$$\mathscr{L} = \mu d/2D$$
$$Z_0 = \sqrt{\mu/\varepsilon}(d/2D)$$

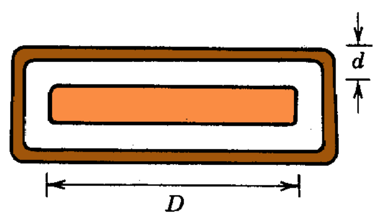

[a] $\mathscr{C}$ = capacitance per unit length (farads/meter); $\mathscr{L}$ = inductance per unit length (henries/meter); Z_0 = characteristic impedance (ohms).

cylinder (of radius R_i) and a grounded outer cylinder (R_o) separated by a medium with dielectric constant ε. We assume a linear magnetic permeability, μ. Figure 9.29a shows a sectional view of a line divided into differential elements of length (Δz). Each element has a capacitance between the center and outer conductors proportional to the length of the element . If *c* is the capacitance per length, the capacitance of an element is *c*Δz. Magnetic fields are produced by current flow along the center conductor, Each differential element also has a series inductance, *l*Δx where *l* is the inductance per unit length. The circuit model of Figure 9.29b can be applied as a model of the transmission line. The quantities *c* and *l* for cylindrical geometry are given by

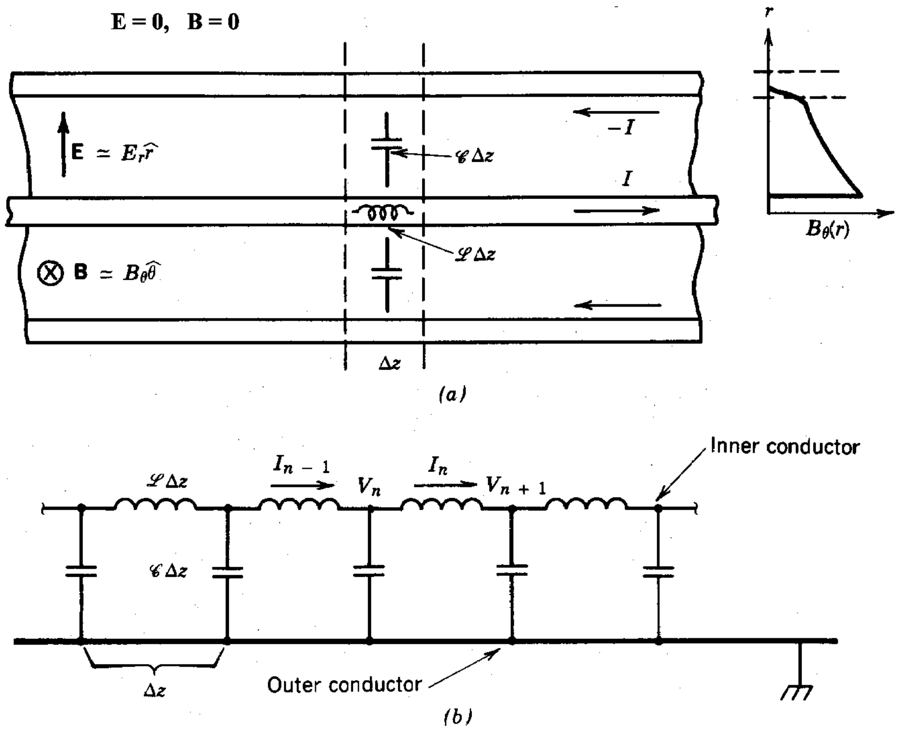

Figure 9.29 Coaxial transmission line. (*a*) Physical basis for lumped circuit element model of TEM wave propagation. (*b*) Lumped circuit element analog of a coaxial transmission line.

$$c = 2\pi\varepsilon \,/\, \ln(R_o/R_i) \qquad (F/m), \tag{9.71}$$

$$l = (\mu/2\pi)\ \ln(R_o/R_i) \qquad (H/m). \tag{9.72}$$

Before solving the circuit of Figure 9.29b, we should consider carefully the physical basis for the correspondence between the circuit model and the coaxial line. The following observations about the nature of electric and magnetic fields in the line are illustrated in Figure 9.29a.

1. Fast-pulsed magnetic fields cannot penetrate into a good conducting material. We shall study this effect, the magnetic skin depth, in Section 10.2. Because there is no magnetic field inside the center conductor, the longitudinal current must flow on the outer surface.

2. The outer conductor is thick compared to the magnetic skin depth. Therefore, magnetic fields resulting from current flow on the inner conductor are not observed outside the line. Real current flowing on the outside of the inner conductor is balanced by negative current flow on the inside of the outer conductor. Magnetic fields are confined between the two cylinders.

3. To an external observer, the outer conductor is an equipotential surface. There is no electrostatic voltage gradient along the conductor, and there is no inductively generated voltage since there are no magnetic fields outside the conductor. Furthermore, the inside surface of the outer conductor is at the same potential as the outside surface since there are no magnetic fields in the volume between the surfaces.

4. If the distance over which current on the inner conductor varies is large compared to (R_o - R_i), then the only component of magnetic field is toroidal, B_θ.

5. Similarly, if the voltage on the inner conductor varies over a long distance scale, then there is only a radial component of electric field.

Observations 1, 2, and 3 imply that we can treat the outer conductor as an ideal ground; voltage variations occur along the inner conductor. The two quantities of interest that determine the fields in the line are the current flow along the inner conductor and the voltage of the inner conductor with respect to the grounded outer conductor. Observations 4 and 5 define conditions under which electromagnetic effects can be described by the simple lumped capacitor and inductor model. The condition is that $\omega \ll v/(R_o - R_i)$, where ω is the highest frequency component of the signal and $v = 1/\sqrt{\epsilon\mu}$. At higher frequency, complex electromagnetic modes can occur that are not well described by a single capacitor and inductor in a length elemental

Voltage differences along the center conductor are inductive. They are supported by changes in magnetic flux in the region between the two cylinders. Differences in current along the center conductor result from displacement current between the inner and outer conductors. The interaction of voltage, real current, and displacement current is illustrated in Figure 9.30a. The figure indicates the motion of a step input in voltage and current down a transmision line. The magnetic field behind the front is constant; the flux change to support the voltage differences between the inner and outer conductors comes about from the motion of the front. There is a rapid change of voltage at the pulse front. This supports a radial displacement current equal to the current of the pulse Current returns along the. other conductor to complete the circuit. T'he balance between these effects determines the relationship between voltage and current and the propagation velocity of the pulse.

Referring to Figure 9.29b, the voltage at point n is equal to the total current that has flowed into the point divided by the capacitance. Using the sign convention shown, this statement is expressed by

$$\int dt\ (I_{n-1} - I_n)\ /\ (c\Delta z) = V_n. \tag{9.73}$$

Taking the derivative,

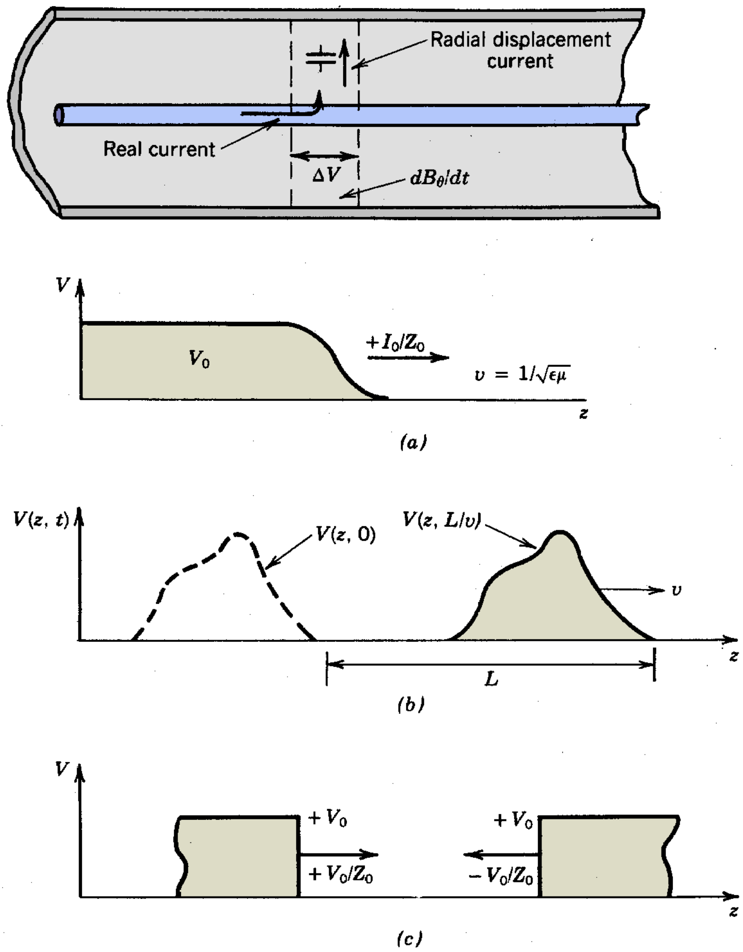

Figure 9.30 Coaxial transmission line. (*a*) Distribution of voltage, real current, and displacement current for a sharp rising step pulse propagating along a transmission line. (*b*) Distributions of voltage on a transmission line at time $t = 0$ (dashed line) and time $t = L/v$ (solid line). (*c*) Polarity conventions for positive voltage impulses traveling in the $+z$ and $-z$ directions.

$$-c\Delta z\ (\partial V_n/\partial t) = I_n - I_{n-1}. \tag{9.74}$$

The relationship is a partial differential equation because we are viewing the change in voltage with time at a constant position. The difference in voltage between two points is the inductive voltage between them, or

$$l\Delta z\ (\partial I_n/\partial t) = V_n - V_{n+1}. \tag{9.75}$$

If Δz becomes small, the discrete voltages approach a continuous function, *V(z, t)*. The voltage difference between two points can be approximated in terms of this function as

$$V_{n+1} \cong V_n + [\partial V(z_n,t)/\partial z]\ \Delta z. \tag{9.76}$$

Similarly,

$$I_{n-1} \cong I_n - [\partial I(z_n,t)/\partial z]\ \Delta z. \tag{9.77}$$

Substituting the results of Eqs. (9.76) and (9.77) into Eqs. (9.74) and (9.75) gives the continuous partial differential equations

$$\partial V/\partial z = -l\ (\partial I/\partial t), \tag{9.78}$$

$$\partial I/\partial z = -c\ (\partial V/\partial t). \tag{9.79}$$

Equations (9.78) and (9.79) are called the *telegraphist's equations*. They can be combined to give wave equations for V and I of the form

$$\partial^2 V/\partial z^2 = (lc)\ (\partial^2 V/\partial t^2). \tag{9.80}$$

Equation (9.80) is a mathematical expression of the properties of a transmisSion line. It has the following implications:

1. It can easily be verified that any function of the form

$$V(z,t) = F(t \pm z/v) \tag{9.81}$$

is a solution of Eq. (9.80) if

$$v = 1/\sqrt{lc}. \tag{9.82}$$

The spatial variation of voltage along the line can be measured at a particular time t by an array of probes. A measurement at a time $t + \Delta t$ would show the same voltage variation but translated a distance $v\Delta t$ either upstream or downstream. This property is illustrated in Figure 9.30b. Another way to phrase this result is that a voltage pulse propagates in the transmission line at velocity v without a change in shape. Pulses can travel in either the +z or -z directions, depending on the input conditions.

2. The current in the center conductor is also described by Eq. (9.80) so that

$$I(z,t) = G(t \pm z/v). \tag{9.83}$$

Measurements of current distribution show the same velocity of propagation.

3. The velocity of propagation in the coaxial transmission line can be found by substituting Eqs. (9.71) and (9.72) into Eq. (9.82):

$$v = 1/\sqrt{\varepsilon\mu} = c/\sqrt{(\varepsilon/\varepsilon_o)(\mu/\mu_o)}. \tag{9.84}$$

This velocity is the speed of light in the medium. The geometric factors in *c* and *l* cancel for all transmission lines so that the propagation velocity is determined only by the properties of the medium filling the line.

4. Inspection of Eqs. (9.78) and (9.79) shows that voltage is linearly proportional to the current at all points in the line, independent of the functional form of the pulse shape. In other words,

$$V = I\ Z_o, \tag{9.85}$$

where Z_o is a real number. The quantity Z_o is called the *characteristic impedance* of the line. Its value depends on the geometry of the line. The characteristic impedance for a coaxial transmission line is

$$Z_o = \sqrt{l/c} = \sqrt{\mu/\varepsilon}\ \ln(R_o/R_i)/2\pi. \tag{9.86}$$

Rewriting Eq. (9.86) in practical units, we find that

$$Z_o = \frac{60\ \ln(R_o/R_i)\ \sqrt{\mu/\mu_o}}{\sqrt{\varepsilon/\varepsilon_o}}\quad (\Omega). \tag{9.87}$$

5. Polarities of voltage and current often cause confusion. Conventions are illustrated in Figure 9.30c. A positive current is directed in the +*z* direction; a negative current moves in the -*z* direction. A positive-going current waveform creates a magnetic flux change that results in a positive voltage on the center conductor.

9.9 TRANSMISSION LINES AS PULSED POWER

A transmission line is a distributed capacitor. Energy is stored in the line when the center conductor is charged to high voltage. Transmission lines have the property that they can produce a constant-voltage output pulse when discharged into a resistive load. In order to understand this, we shall first consider the properties of signal propagation on finite length fines with resistive loads at an end. A load at the end of a transmission line is called a *termination*.

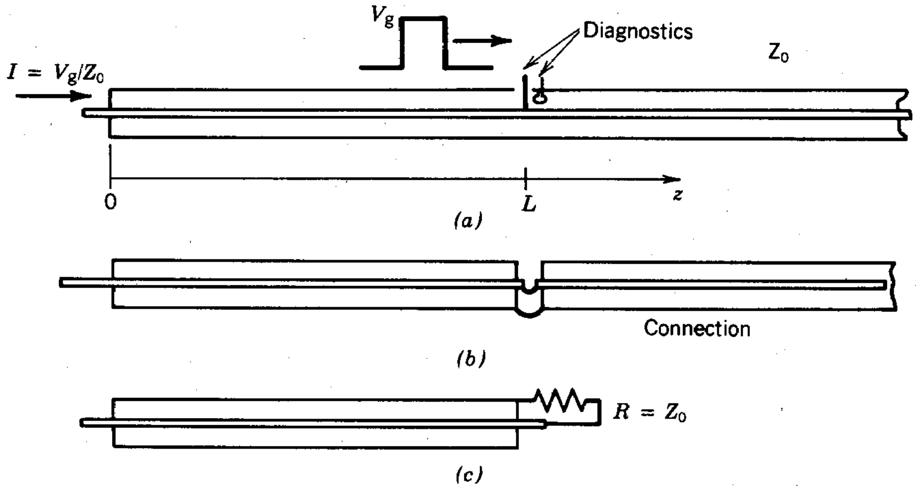

Figure 9.31 Matched terminations of a transmission line. (*a*) Infinite length line with characteristic impedance Z_0. (*b*) Finite length line connected to a semiinfinite length line with the same characteristic impedance. (*c*) Transmission line terpminated by a matched resistor ($R = Z_0$).

Figure 9.31 shows a transmission line extending from $z = 0$ to infinity driven by a voltage generator. The generator determines the entrance boundary condition on the line: $V_g(z = 0, t)$. The generator supplies a current V_g/Z_0. The assumption of an infinite line means, that there are no negatively-directed waves. There is a positively-directed wave produced by the generator. A voltage probe a distance L from the generator measures a signal $V_s(t') = V_g(t' - L/v)$. Similarly a current probe gives a signal $I_s(t') = V_g(t' - L/v)/Z_o$.

Assume that the line is split at the point L and he pieces are connected together with a good coaxial connector. This change makes no difference in wave propagation on the line or the signals observed at L. Proceeding another step, the infinite length. of line beyond the split could be replaced with a resistor with value $R = Z_o$. The important point is that, in term of observations at L, wave propagation with the resistive termination is indistinguishable from that with the infinite line. The boundary condition at the connection point is the same, $V(L, t) = I(L, t)Z_o$. In both cases, the energy of the pulse passes through the connector and does not return. In the case of the line, pulses propagate to infinity. With the resistor, the pulse energy is dissipated. T'he resistor with R = Z_o is a *matched termination*.

We must consider the properties of two other terminations in order to understand the transmission line as an energy storage element. One of them is an open circuit, illustrated in Figure 9.12a. Assume the voltage generator produces a sharp rising step pulse with voltage $+V_o$ and current $+I_o$. When the step function reaches the open circuit, it can propagate no further. The open-circuit condition requires that a probe at position $z = L$ measures zero current. This occurs if the boundary reflects the original wave as shown, giving a pulse propagating in the negative z direction with positive voltage and negative current. When this pulse is added to the positive-going pulse from the generator, the net current is zero and the net voltage is $+ 2V_o$.

Similar considerations apply to the short-circuit termination (Fig. 9.32b). A voltage probe at $z = L$ always measures zero voltage. The interaction of the inconung wave with a short-circuit

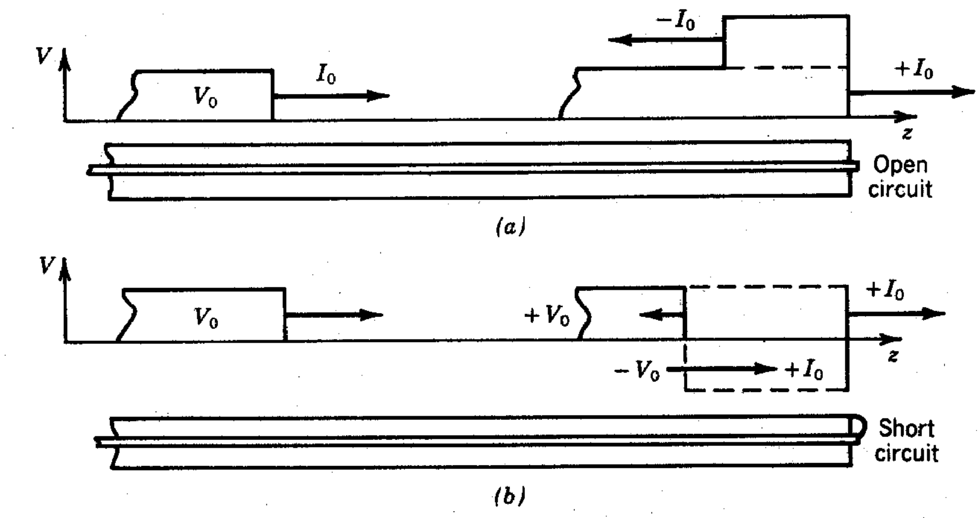

Figure 9.32 Reflection of step-function pulses at a transmission line termination. (*a*) Open circuit. (*b*) Short circuit.

termination generates a negative-going wave with negative voltage and positive current. In other words, the termination acts as an inverting transformer. These reflection properties can be confirmed by a direct numerical solution of Eqs. (9.78) and (9.79) with appropriate boundary conditions.

The circuit for a transmission line pulsed voltage modulator is shown in Figure 9.33. The center conductor of a line of length L is charged to high voltage by a power supply. The supply is connected through a large resistance or inductance; the connection can be considered an open circuit during the output pulse. The other end of the line is connected through a shorting switch to the load. We assume the load is a matched termination, $R = Z_o$.

Consider, first, the state of the charged line before switching. The center conductor has voltage V_o. There is no net current flow. Reference to Figure 9.33 shows that the standing voltage waveform of this state can be decomposed into two oppositely directed propagating pulses. The pulses are square voltage pulses with length L and magnitude ½V_o. The positively-directed pulse reflects from the switch open-circuit termination to generate a negatively-directed pulse that fills in behind the original negative-going pulse. The same process occurs at the other open-circuit termination; therefore, the properties of the line are static.

The resolution of a static charge into two traveling pulses helps in determining the time-dependent behavior of the circuit following switching. We are free to choose the boundaries of the positive and negative pulses at any location; let us assume that they are at $z = 0$ and $z = L$ at the time of switching, $t = 0$. Following switching, the positive-going pulse travels into the termination while the negative pulse moves away from it. The positive pulse produces a flat-top voltage waveform of duration $\Delta t = L/v$ and magnitude ½V_o in the load. At the same time, the negative-gomg pulse reflects from the open circuit at the charging end and becomes a

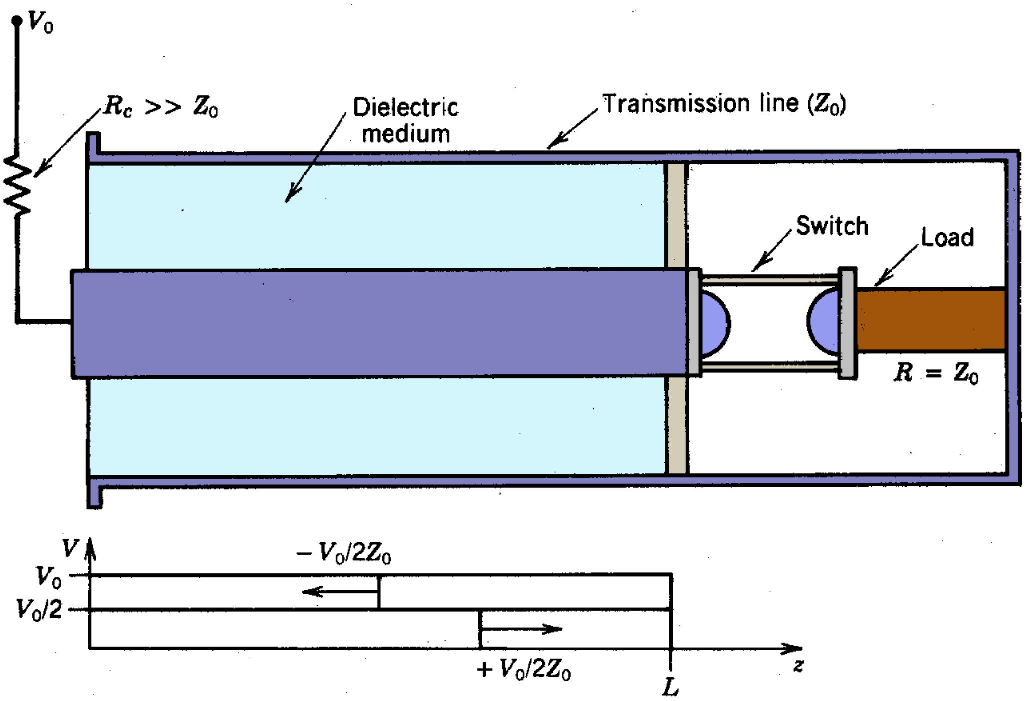

Figure 9.33 Coaxial transmission line used as a square-pulse generator.

positive-going pulse following immediately behind the original The negative pulse deposits its energy in the load during the time $L/v \le t \le 2L/v$. In summary, the discharge of a transmission line through a shorting switch into a matched resistive load produces a constant-voltage pulse. The magnitude of the pulse is ½V_o and the duration is

$$\Delta t_p = 2L/v. \tag{9.88}$$

where v is the pulse propagation velocity.

The total capacitance of a transmission line of length L can be expressed in terms of the single transit time for electromagnetic pulses ($\Delta t = L/v$) and the characteristic impedance as

$$C = \Delta t/Z_o. \tag{9.89}$$

It is easily demonstrated that energy is conserved when the line is discharged into a matched termination by comparing CV_o^2 to the time integral of power into the load. The total series inductance of a transmission line is

$$L = Z_o\Delta t. \tag{9.90}$$

Transformer oil is a common insulator for high-voltage transmission lines. It has a relative dielectric constant of 3.4. The velocity of electromagnetic pulses in oil is about 0.16 m/ns. Voltage hold-off in a coaxial transmission line is maximized when $R_i/R_o = 1/e$. For oil this translates into a 33 Ω characteristic impedance [Eq. (9.87)). Purified water is used as a transmission line energy storage medium in high-power density pulsed modulators because of its high relative dielectric constant ($\varepsilon/\varepsilon_o \cong 81$). Water is conductive, so that water lines must be pulse charged. In comparison with oil, a water line with a l/*e* radius ratio can drive a 6.8 Ω load. For the same charge voltage, the energy density in a water line is 24 times higher than in an oil line.

9.10 SERIES TRANSMISSION LINE CIRCUITS

Two features of the transmission line pulse modulator are often inconvenient for high-voltage work. First, the matched pulse has an amplitude only half that of the charge voltage. Second, the power transfer switch must be located between the high-voltage center conductor and the load. The switch is boosted to high voltage; this makes trigger isolation difficult. The problems are solved by the Blumlein transmission line configuration [A. D. Blumlein, U.S. Patent No. 2,465,840 (1948)]. The circuit consists of two (or more) coupled transmission lines. Fast-shorting switches cause voltage reversal in half the lines for a time equal to the double transit time of electromagnetic pulses. The result is that output pulses are produced at or above the dc charge voltage, depending on the number of stages. The Blumlein line circuit is the distributed element equivalent of the LC generator.

We shall analyze the two-stage transmission line driving a matched resistive load. A circuit with nested coaxial transmission lines is illustrated in Figure 9.34a. The three cylinders are labeled *OC* (outer conductor), *IC* (intermediate conductor), and *CC* (center conductor) . The diameters of the cylinders are usually chosen go that the characteristic impedance of the inner line is equal to that of the outer line. This holds when $R_{OC}/R_{IC} = R_{IC}R_{CC}$. We neglect end effects and assume that both lines have the same electromagnetic transit time.

A high-voltage feed penetrates the outer cylinder to charge the intermediate cylinder. The center conductor is connected to ground through an isolation element. The isolator acts as a short circuit over long times but approximates an open circuit during the output pulse. It is usually a simple inductor, although we shall investigate a more complex isolator when we study linear induction accelerators (Section 10.5). A shorting switch between the *IC* and *OC* is located at the end opposite the load.

The equivalent circuit of the two-stage Blumlein line is shown in Figure 9.34b. In order to analyze the pulse output of the circuit, we make the following assumptions:

1. The middle conductor is taken as a reference to analyze traveling voltage pulses.

2. The isolation element is an ideal open circuit during the pulse output.

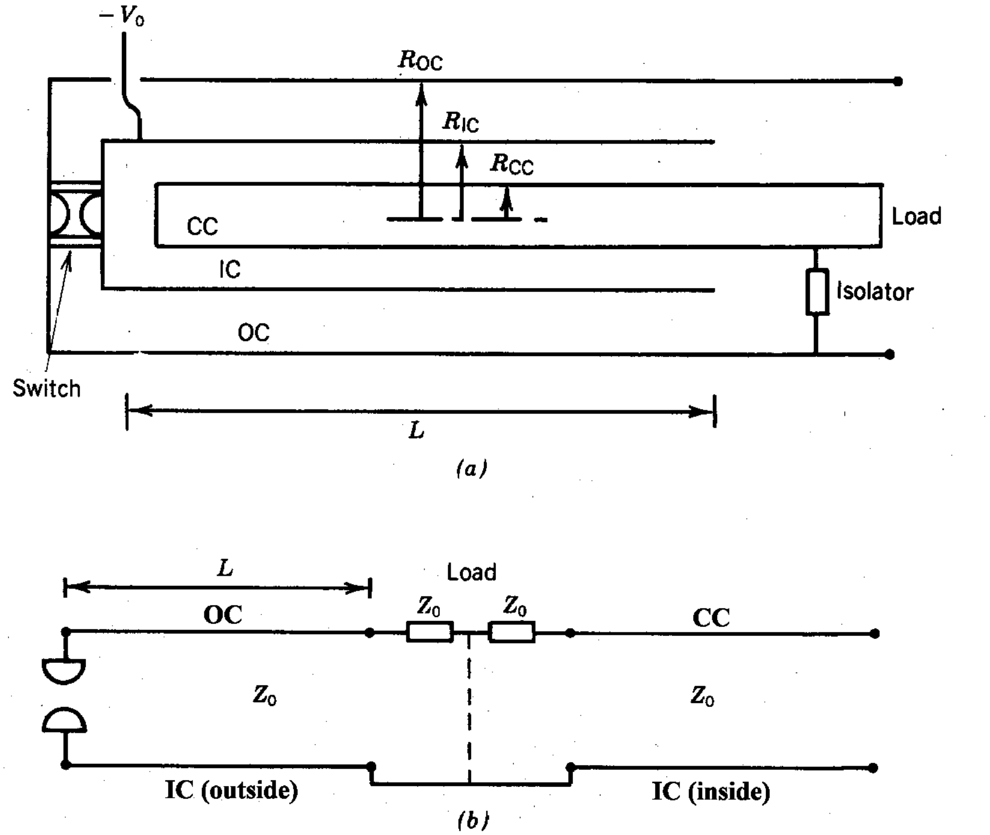

Figure 9.34 Nested coaxial transmission lines in the Blumlein configuration. (*a*) Schematic view and definition of quantities. (*b*) Equivalent circuit.

3.The load resistance is $Z_1 = 2Z_o$, where Z_o is the characteristic impedance of the individual nested lines.

4. An imaginary connection is attached from the intermediate conductor to the midpoint of the load during the output pulse. This connection is indicated by dotted lines in Figure 9.34b.

In the steady state, the intermediate conductor is charged to $-V_o$. The other two electrodes have positive voltage relative to the intermediate conductor. The static charge can be represented in the inner and outer lines as two oppositely-directed positive voltage pulses of length L and magnitude $\frac{1}{2}V_o$. Pulses arriving at the end connected to the load are partially reflected and partially transmitted to the other line. Transmission is the same in both directions so that a steady state is maintained. Assume that the boundaries of positive and negative pulses are aligned as shown in Figure 9.35a at switching time $t = 0^-$.

The following events take place when the shorting switch is activated:

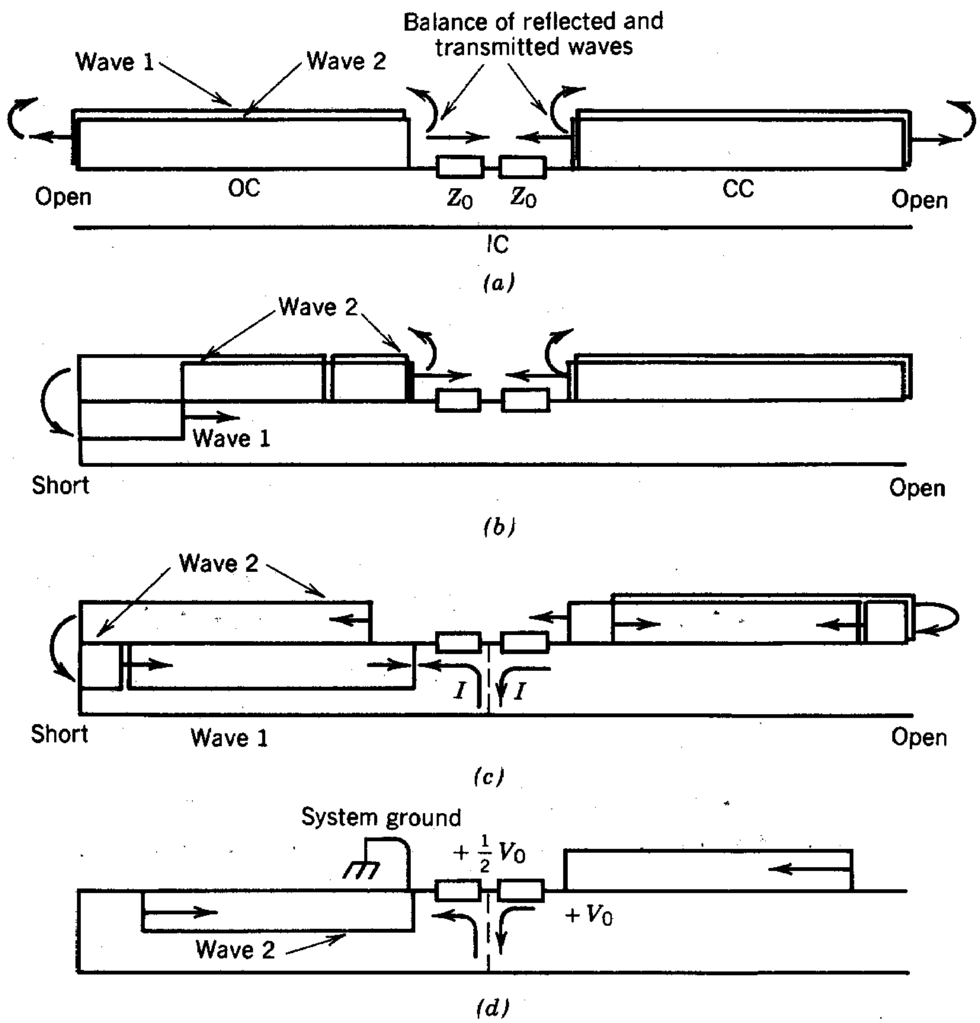

Figure 9.35 Propagation and reflection of step-function pulses following switching of a Blumlein line. (*a*) Resolution of static charge voltage prior to switching into interleaved traveling pulses. (*b*) Pulse polarities and directions during interval $0 < t < L/v$. (*c*) Pulses during interval $L/v < t < 2L/v$. (*d*) Pulses during interval $2L/v < t < 3L/v$.

1. There is a time lag before information about the shorting is communicated the load. During this time, the +z-directed pulse in the outer line and the -z-directed pulse in the inner line continue to move toward the load. The balance of transmission and reflection causes a positive-polarity reflected pulse to move backward in each line as though the midpoint were an open circuit (Fig. 9.35b).

2. The +z-directed pulse in the inner line moves to the open-circuit end opposite the load and is reflected with positive polarity. The major activity in the circuit is associated with the -z-directed pulse on the outer fine. This pulse encounters the short circuit and reflects with negative polarity.

3. The negative-polarity pulse arrives at the load at $\Delta t = L/v$. We make the imaginary connection at this time. Power from the positive pulse in the inner line and the negative pulse in the outer line is deposited in the two matched loads (Fig. 9.35c). The voltages on the loads have magnitude $\frac{1}{2}V_o$ and the same polarity; therefore, there is a net voltage of V_o between the connection points of the center and outer conductors to the load.

4. The situation of Figure 9.35c holds for $\Delta t < t < 2\Delta t$. During this time, the other pulse components in the two lines reflect from the boundaries opposite the load. The polarity of the reflected wave is positive in the inner line and negative in the outer line.

5. The pulses that originally moved away from the load deposit their energy during the time $2\Delta t < t < 3\Delta t$ (Fig. 9.35d).

6. Inspection of Figures 9.35c and d shows that currents from the two lines are equal and opposite in the imaginary conductor during the output pulse. Because the connection carries no current, we can remove it without changing the circuit behavior.

The above model resolves the Blumlein line into two independent transmission lines driving a series load. The voltage in one line is reversed by reflection at a short circuit. Voltages that cancel in the static state add in the switched mode. In summary, the Blumlein line circuit has the following characteristics:

1. An output voltage pulse of V_o is applied to a matched load between the center conductor and the outer conductor for the double transit time of an individual line, $2L/v$.

2.The voltage pulse is delayed from the switch time by an interval L/v.

3.The matched impedance for a two-stage Blumlein line is $2Z_o$.

4.A negatively charged intermediate conductor results in a positive output pulse when the switch is located between the intermediate and outer conductors. The output pulse is negative if a shorting switch is located between the intermediate and center conductors.

The Blumlein line configuration is more difficult to construct than a simple transmission line. Furthermore, the Blumlein line has no advantage with respect to energy storage density. Neglecting the thickness of the middle conductor and its voltage grading structures, it is easy to show that the output impedance, stored energy density, pulselength, and output voltage are the same as that for an equal volume transmission line (with $R_i = R_{CC}$ and $R_o = R_{OC}$) charged to $2V_o$. The main advantage of the Blumlein line is that requirements on the charging circuit are relaxed. It is much less costly to build a 1-MV Marx generator than 2-MV generator with the same stored energy. Furthermore, in the geometry of Figure 9.34, the switch can be a trigatron with the triggered electrode on the ground side. This removes the problem of trigger line isolation.

9.11. PULSE-FORMING NETWORKS

Transmission lines are well suited for output pulselengths in the range 5 ns < Δt_p < 200 ns, but they are impractical for pulselengths above 1 μs. Discrete element circuits are usually used for long pulselengths. They achieve better output waveforms than the critically damped circuit by using more capacitors and inductors. Discrete element circuits that provide a shaped waveform are called *pulse-forming networks*.

The derivations of Section 9.8 suggest that the circuit of Figure 9.36 can provide a pulse with an approximately constant voltage. A transmission line is simulated by a finite number *N* of inductor-capacitor units. Following the derivation of Section 9.8, the resistance of a matched load is

$$Z_o = \sqrt{L/C}. \tag{9.91}$$

The quantities L and *C* are the inductance and capacitance of discrete elements. We shall call Z_o the impedance of the PFN. The single transit time of an electromagnetic pulse through the network is approximately $N\sqrt{LC}$. The output voltage pulse has average magnitude ½V_o and duration $\Delta t_p \cong 2N\sqrt{LC}$.

The output pulse of a five-element network into a matched resistive load is shown in Figure 9.37. Although the general features are as expected, there is substantial overshoot at the beginning of the pulse and an undershoot at the end. In addition, there are voltage oscillations during the pulse. In some applications, these imperfections are not tolerable. For instance, the pulse modulator may be used to drive an ion injector where the beam optics depends critically on the voltage.

A Fourier analysis of the circuit of Figure 9.36 indicates the basis for the poor pulse shaping. The circuit generates *N* Fourier components with relative amplitudes optimized to replicate a sharp-edged square voltage pulse. In the Fourier series expansion of a square pulse, the magnitudes of the terms of order *n* decrease only as the inverse of the first power of *n*, $a_n \sim 1/n$. Thus, many terms are needed for an accurate representation. In other words, a large number of

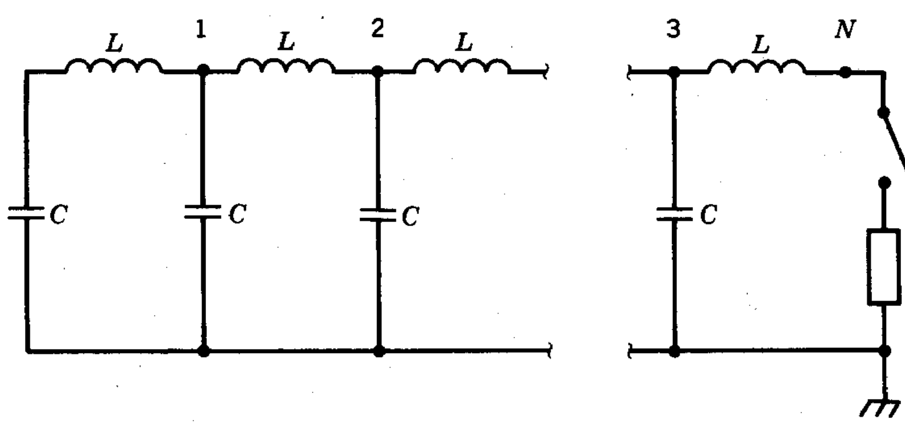

Figure 9.36 Pulse-forming network; lumped element approximation of a transmission line.

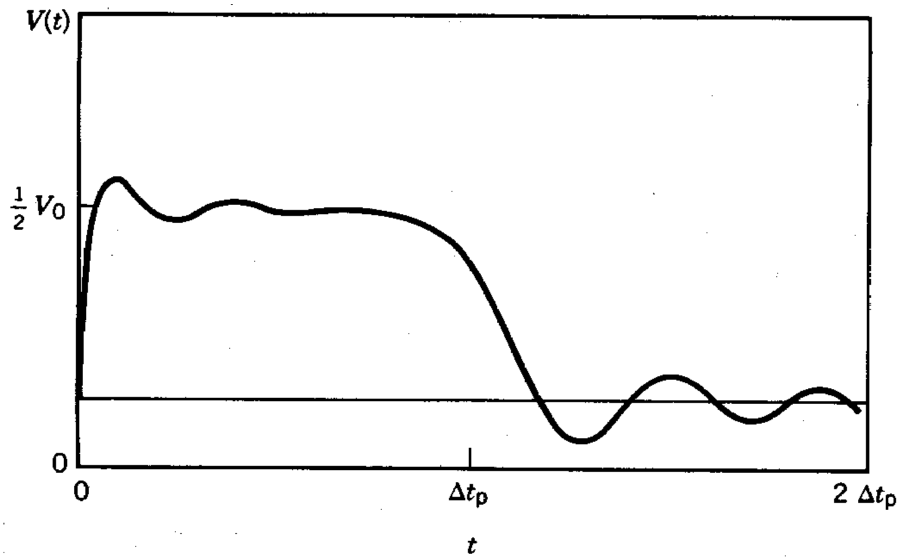

Figure 9.37 Load voltage, five-element PFN discharged into a matched load.

elements is needed in the circuit of Figure 9.36 for a relatively constant output voltage. Such a division increases the size and cost of the modulator.

A different approach to the PFN, developed by Guillemin [E.A. Guillemin, **Communications Networks, Vol. II**, (Wiley, New York, 1935)] provides much better pulse shaping with fewer elements. He recognized that the slow convergence of the network of Figure 9.36 is a consequence of approximating a discontinuous waveform. In most applications, the main concern is a good voltage flat-top, and gradual voltage variation on the rise and fall of the pulse can be tolerated The key is to work in reverse from a smooth waveform to derive a generating circuit.

We can utilize a Fourier series analysis if we apply the following procedure. Consider first an ideal transmission line discharged into a short-circuit load (Fig. 9.38a). The current oscillates between $+2I_o$ and $-2I_o$, where I_o is the output current when the line is discharged into a matched load, $I_o = V_o/2Z_o$. The periodic bipolar waveform can be analyzed by a Fourier series. When the circuit is connected to a matched load, there is a single square pulse (Fig. 9.38b). By analogy, if we could determine a circuit that produced a different bipolar current waveform with peak amplitude $2I_o$, such as the trapezoidal pulse of Figure 9.38c, then we expect that it would produce a trapezoidal pulse (Fig 9.38d) of amplitude I_o when connected to a resistance $R = V_o/2I_o$. We shall verify this analogy by direct computation.

It remains to determine a circuit that will produce the waveform of Figure 9.38c.when discharged into a short. The Fourier series representation of a trapezoidal current pulse with magnitude $2I_o$, total length Δt_p and rise and fall times $a\Delta t_p$ is

$$i(t) = 2I_o \sum_n \left(\frac{4}{n\pi}\right) \left(\frac{\sin(n\pi a)}{n\pi a}\right) \sin\left(\frac{n\pi t}{\Delta t_p}\right). \tag{9.92}$$

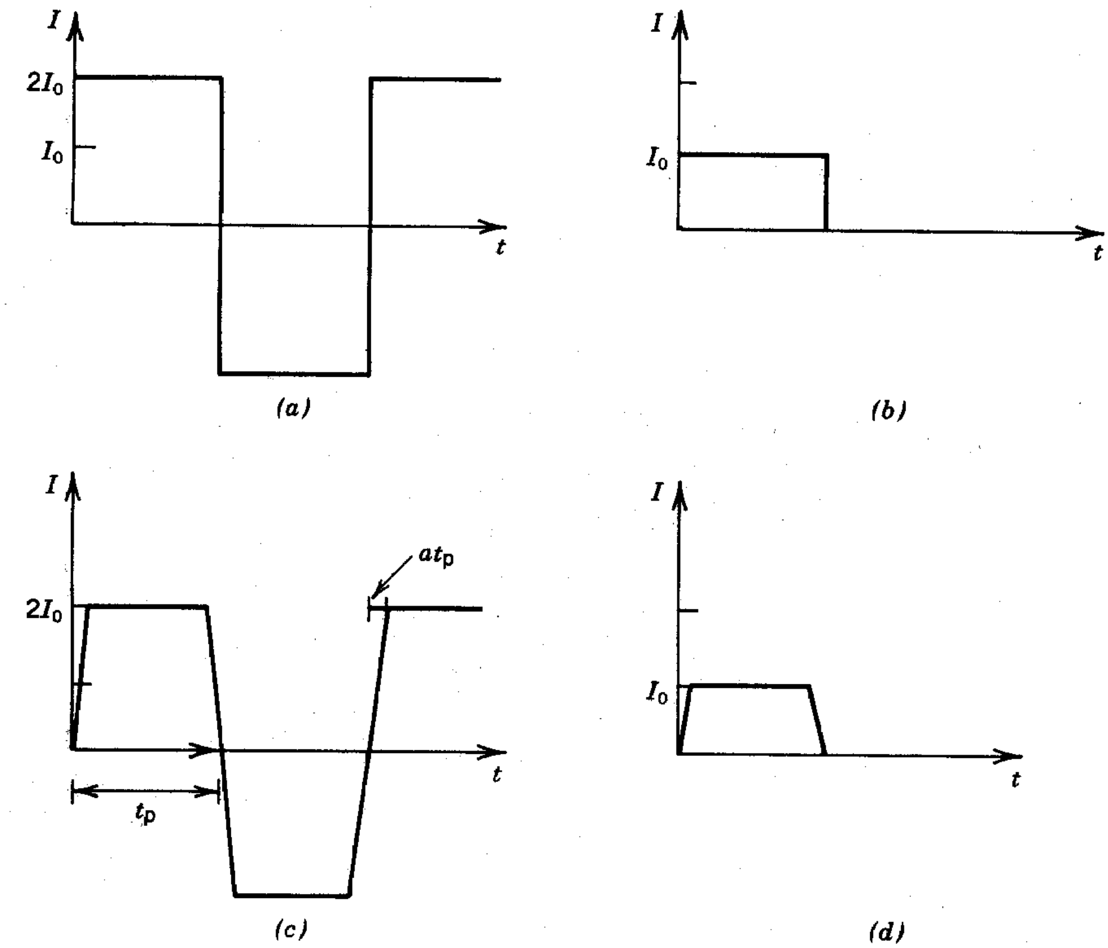

Figure 9.38 Design concept for Guillemin networks. (*a*) Output current of an ideal transmission line discharged into a short circuit. (*b*) Output current of an ideal transmission line discharged into a matched resistor. (*c*) Trapezoidal pulse of a Guillemin network discharged into a short circuit. (*d*) Guillemin network discharged into a matched resistor.

Consider the circuit of Figure 9.39. It consists of a number of parallel LC sections. If the PFN is dischared into a short circuit, the current flow through each of the sections is independent of the others. This occurs because the voltage across each section is zero. The current in a particular section after switching is

$$i_n(t) = i_{n0} \sin\left(\frac{t}{\sqrt{L_n C_n}}\right) \tag{9.93}$$

We choose the inductance and capacitance of sections so that their free harmonic oscillations are at the frequency of the Fourier components in Eq. (9.92). In other words,

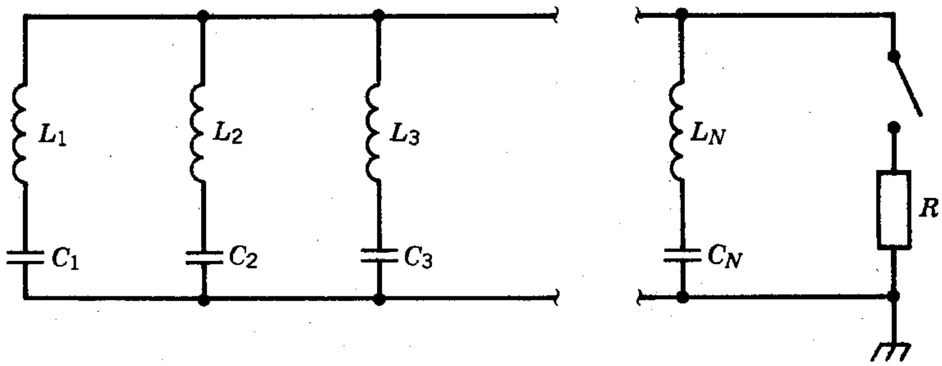

Figure 9.39 Basic Guillemin network.

$$\sqrt{L_1C_1} = \Delta t_p/\pi, \quad \sqrt{L_2C_2} = \Delta t_p/2\pi, \quad \sqrt{L_3C_3} = \Delta t_p/3\pi, \ \ldots \tag{9.94}$$

We know from our study of the undamped *LC* circuit (Section 9.6) that the magnitude of the current flowing through any one of the sections after switching is

$$i_{n0} = V_0/\sqrt{L_n/C_n}. \tag{9.95}$$

If Z_o is the desired characteristic impedance, the magnitude are matched to the Fourier series if

$$V_o/\sqrt{L_n/C_n} = (V_o/Z_o)\ (4/n\pi)\ [\sin(n\pi a)/n\pi a], \tag{9.96}$$

where we have substituted $V_o/Z_o = 2I_o$. Equations (9.94) and (9.96) can be solved to give the appropriate component values of the PFN:

$$L_n = (Z_o\Delta t_p/4)\ /\ [\sin(n\pi a)/n\pi a], \quad C_n = (4\Delta t_p/n^2\pi^2 Z_o)\ /\ [\sin(n\pi a)/n\pi a]. \tag{9.97}$$

Figure 9.40 shows a voltage pulse on a matched resistor ($R = Z_o$) for three and five-element Guillemin networks using the circuit values determined from Eqs. (9.97). Note the improvement compared to the pulse shape of Figure 9.37. Equation (9.92) shows that the Fourier expansion converges as $1/N^2$. A better flat-top can be obtained by approximating smoother pulses. For instance, the series converges as $1/N^3$ if the pulse is assumed to have parabolic edges with no discontinuity in slope. Alternate circuits to that of Figure 9.39 can be derived. The main disadvantage of the Guillemin network is that the capacitors all have different values. It is usually difficult to procure commercial high-voltage capacitors with the required capacitances.

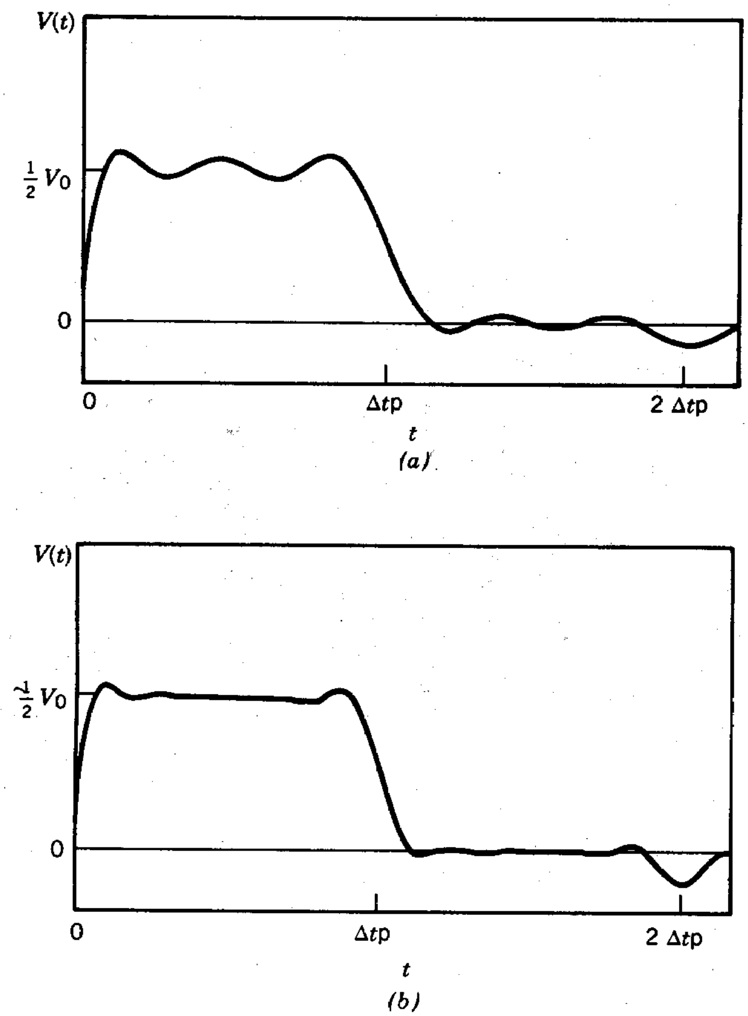

Figure 9.40 Load voltage, Guillemin network discharged into a matched resistor. (*a*) Three-element network. (*b*) Five-element network.

9.12 PULSED POWER COMPRESSION

Electron and ion beams in the megampere range have been generated in pulsed power diodes [see T. H. Martin and M. F. Rose, Eds., **Proc. 4th IEEE Pulsed Power Conference**, (IEEE 83CH1908-3, Piscataway, New Jersey, 1983)]. Such beams have, application to inertial fusion and studies of materials at high temperature, pressure, and radiation levels. High-power pulse modulators are needed to drive the diodes. Pulsed power research is largely centered on extending the limits of the output power of voltage generators. At present, single-unit generators have been built that can apply power in the TW (10^{12} W) range to a load. Typical output parameters of such a modulator are 1 MA of current at 1 MV in a 50-ns pulse. Parallel generators have reached levels of 10 TW.

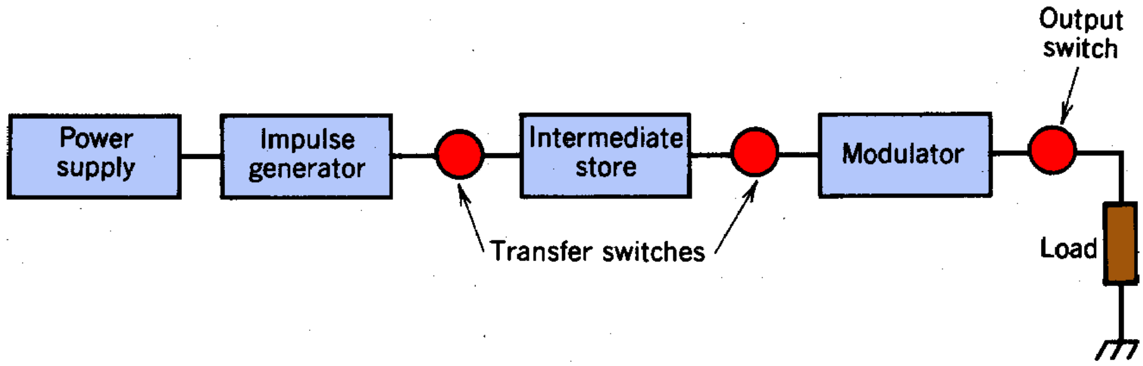

Figure 9.41 Schematic diagram of a pulsed power compression sequence.

Power compression is the technique that has allowed the generation of such high output. A general power compression circuit is illustrated in Figure 9.41. Energy is transferred from one stage of energy storage to the next in an increasingly rapid sequence. Each storage stage has higher energy density and lower inductance. Even though energy is lost in each transfer, the decrease in transfer time is sufficient to raise the peak power.

The first power compression stage in Figure 9.41 is one we are already familiar with. A dc source charges an impulse generator such as a Marx generator. The output power from the Marx generator may be a factor of 10^7 higher than the average power from the source. In the example, the Marx generator transfers its energy to a low-inductance water-filled capacitor. A shorting switch then passes the energy to a low-impedance transmission line. A low-inductance multi-channel switch then connects the line to a vacuum load. Power multiplication in stages following the Marx generator are not so dramatic; gains become increasingly difficult. Figure 9.42 is a scale drawing of a pulsed power compression system to generate 300-kV, 300-kA, 80-ns pulses. The system consists of a low inductance 1-MV *LC* generator that pulse-charges a 1.5-Ω water-filled transmission line. Energy from the line is transferred by a multi-element high-pressure gas switch. The pulse is matched to a 1-Ω electron beam load by a coaxial line transformer.

The highest power levels have been achieved with multiple stages of capacitive energy storage connected by sequenced shorting switches. Triggered gas-filled switches are used in the early stages. Gas switches have too much inductance for later stages, so that self-breakdown between electrodes in a highly stressed liquid medium is used. Discharges in liquids absorb considerable energy. The resulting shock wave rapidly erodes electrodes. Therefore, machines of this type are fired typically 1-10 times per day and may need repair after 10-100 shots. In Section 9.13, we shall study a potential method for low-inductance switching at high repetition rate, saturable core magnetic switching. Characteristics of the EAGLE pulsed power generator are summarized in Table 9.4.

Transfer of energy between capacitors forms the basis of most pulsed power generators. A model for the transfer is illustrated in Figure 9.43. A capacitor is charged to voltage V_o, and then energy is switched through an inductance to a second capacitor by a shorting switch. The inductance may be

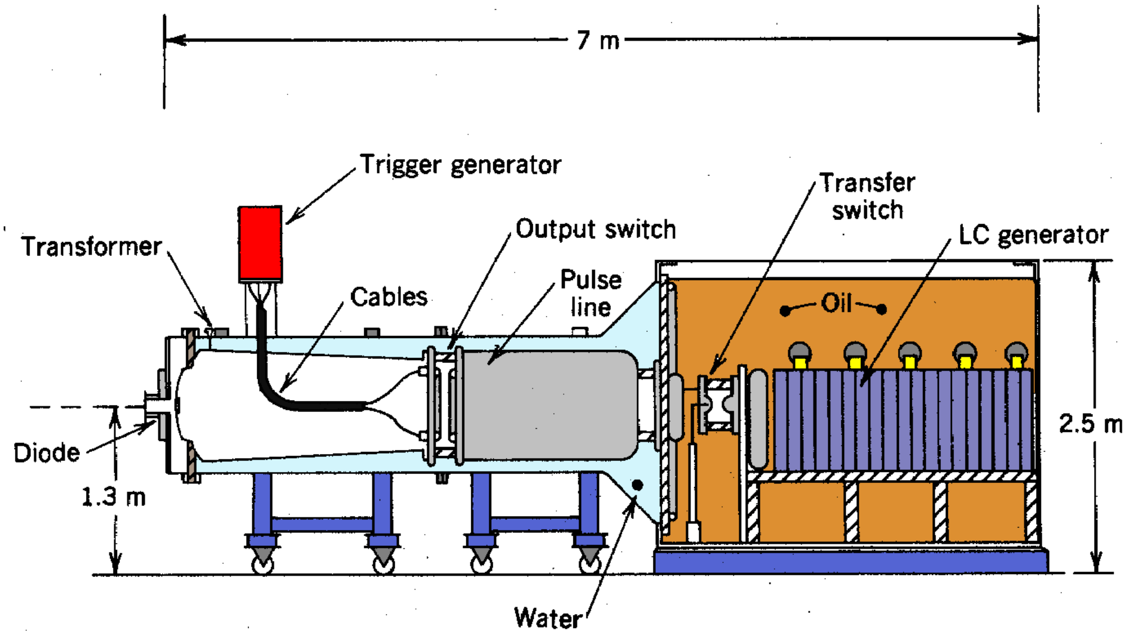

Figure 9.42 Neptune C, low-impedance pulsed power generator using overstressed water dielectric. (Courtesy H. Milde, Ion Physics Corporation.)

introduced purposely or may represent the inevitable parasitic inductance associated with current flow. Current in the circuit is described by the equation

$$-V_o + \int i dt/C_1 + L\ (di/dt) + \int i dt/C_2 = 0,$$

or

$$L\ (d^2i/dt^2) = -i\ (C_1+C_2)/C_1C_2. \tag{9.98}$$

If the switch, is closed at $t = 0$, then the initial conditions are $i(0) = 0$ and d$i(0)$/d$t = V_o/L$. The solution of Eq. (9.98) is

$$i(t) = V_o \sin(\omega t) \ / \ \sqrt{L(C_1+C_2)/C_1C_2}\ , \tag{9.99}$$

where

$$\omega = \sqrt{L\ C_1C_2/(C_1+C_2)}$$

TABLE 9.4 Parameters: EAGLE Pulsed Power Generator[a]

EAGLE module

1. Power compression cycle[b]

Element	Energy Transfer Time (μs)	Output Switch
Marx generator	1.3	Gas switches (25), active trigger
Transfer capacitor water-filled	0.3	Triggered gas switch, high-voltage isolation
Charging pulseline	0.1	Multipin, self-breaking water switch
Pulse-forming line	0.1	Multipin, self-breaking water switch

2. Measured parameters

Marx generator, stored energy	500 kJ
Marx generator voltage	3.15 MV
Energy transfer efficiency	50%
Output power	4.5×10^{12} W
Output energy	275 kJ
Output current (1.9-Ω load)	1.6 MA
Pulselength (FWHM power)	75 ns
Output voltage	3 MV

ROULETTE-X (Proposed)

Function	Generation of Bremsstrahlung radiation and soft X rays for nuclear weapons effect simulation
Number of EAGLE modules	20
Design power at load	7×10^{13} W
Pulselength (FWHM power)	75 ns
Output voltage	2–2.5 MV
Output energy	5 MJ
Output current	20–22 MA

[a] Physics International Company

[b] Configuration: Marx generator with three stages of power compression using overstressed water dielectric. First two elements perform power compression in time, last two perform compression in space for multimodule compatibility.

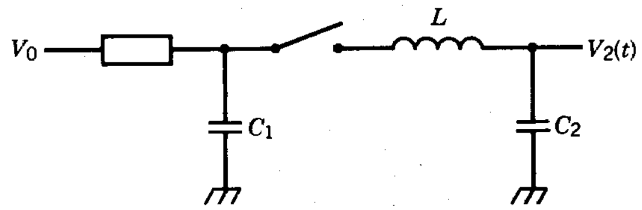

Figure 9.43 Peaking capacitor circuit.

The quantities of interest are the time-dependent charge voltages on the two capacitors.

$$V_1(t) = V_o - \int idt/C_1, \quad V_2(t) = \int idt/C_2. \tag{9.100}$$

Substituting Eq. (9.99) into Eqs. (9.100), we find that

$$V_1 = V_o\ [1 - [C_2/(C_1+C_2)]\ (1 - \cos\omega t)], \tag{9.101}$$

$$V_2 = V_o\ [1 - [C_1/(C_1+C_2)]\ (1 - \cos\omega t)]. \tag{9.102}$$

Waveforms are plotted in Figure 9.44 for $C_2 = C_1$ and $C_2 \ll C_1$. The first case is the optimum choice for a high-efficiency power compression circuit. A complete transfer of energy from the first to the second capacitor occurs at time $t = \pi/\omega$. In the second case, the energy transfer is inefficient but the second capacitor is driven to twice the charge voltage of the first. For this reason, the circuit of Figure 9.43 is often called the *peaking capacitor circuit*.

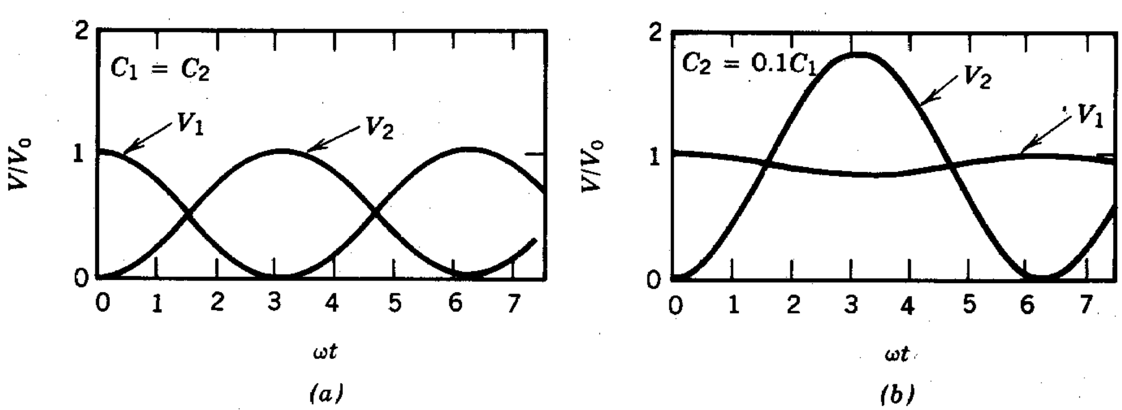

Figure 9.44 Voltage waveforms on storage capacitor and charged capacitor in a peaking capacitor circuit. (*a*) $C_2 = C_1$. (*b*) $C_2 = 0.1C_1$.

9.13 PULSED POWER SWITCHING BY SATURABLE CORE INDUCTOR

Although the process of pulse shaping by saturable core ferromagnetic inductors has been used for many years in low-voltage circuits, application to high-power circuits is a recent area of interest. Magnetic switches can be constructed with low inductance and high transfer efficiency. Energy losses are distributed evenly over the core mass, and there is no deionization time as there is in gas or liquid breakdown switches. These factors give magnetic switches potential capability for high repetition rate operation.

A two-stage power compression circuit with a magnetic switch is shown in Figure 9.45a. Capacitors C_0 and C_1 constitute a peaking circuit. Energy is transferred by a normal shorting switch. The energy in C_1 is then routed to a load by a saturable core inductor switch. The circuit achieves power compression if the switch out time from C_1 is short compared to the initial transfer. We choose $C_0 = C_1$ for high efficiency.

In order to understand the operation of the circuit of Figure 9.45 a, we must refer to the hysteresis curve of Figure 5.12. We assume that the ferromagnetic core of the inductor is ideal; its properties are described by a static hysteresis curve. This means that there are no real currents

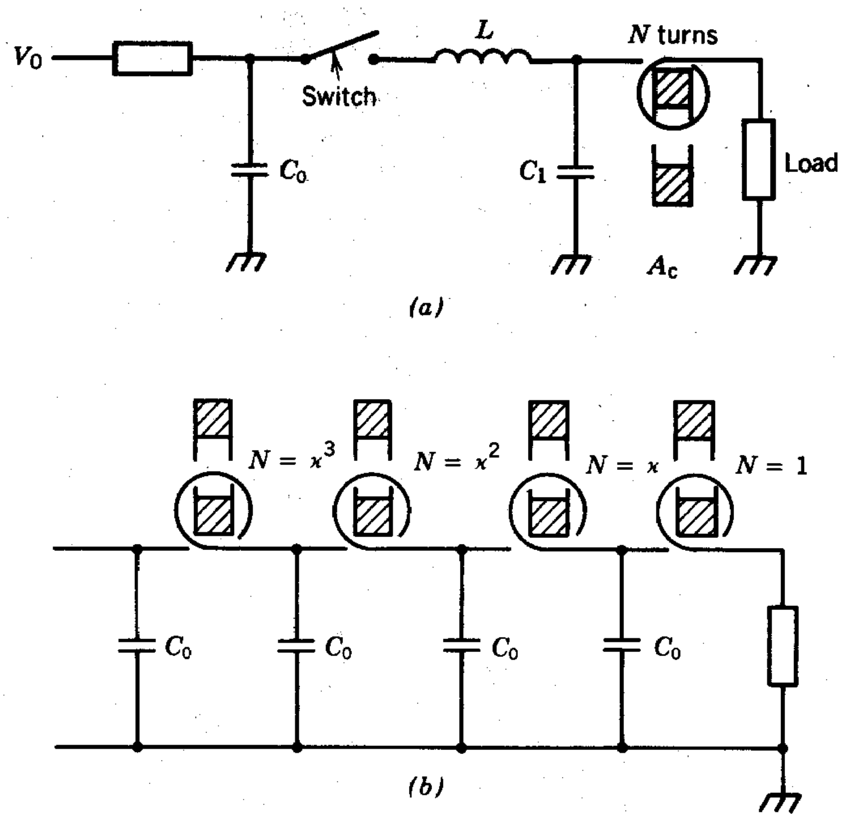

Figure 9.45 Saturable core magnetic switching. (*a*) Peaking capacitor circuit with magnetic output switch. (*b*) Multistage power compression circuit with uniform capacitors and ferromagnetic cores.

flowing in the core material; magnetic effects are produced solely by alignment of atomic currents. Methods of core construction to assure this condition are described in Chapter 10. We further assume that at some time before $t = 0$ a separate circuit has pulsed a negative current through the ferromagnetic core sufficient to bias it to $-B_s$. After the current is turned off, the core settles to a state with flux level $-B_r$. This process is called *core reset*.

Consider the sequence of events after the shorting switch is activated. At early times, the right-hand portion of the circuit is approximately an open circuit because of the high inductance of the winding around the high μ core. Energy flows from C_0 to C_1; the voltage on C_1 is given by Eq. (9.102). Further, Faraday's law implies that

$$V_1(t) = N A_c (dB/dt), \tag{9.103}$$

where A_c is the cross-section area of the core and N is the number of windings in the inductor. The core reaches saturation when

$$\int V_1(t)\ dt = N A_c (B_s + B_r). \tag{9.104}$$

After saturation, the inductance L_2 decreases by a large factor, approaching the vacuum inductance of the winding. The transition from high to low inductance is a bootstrapping process that occurs rapidly. Originally, translation along the H axis of the hysteresis curve is slow because of the high inductance. Near saturation, the inductance drops and the rate of change of leakage current increases. The rate of change of H increases, causing a further drop in the inductance. The impedance change of the output switch may be as fast as 5 ns for a well-designed core and low-inductance output winding.

Energy is utilized efficiently if the output switch has high impedance for $0 \leq t \leq \pi/\omega$ and the switch core reaches saturation at the end of the interval when all the circuit energy is stored in C_1. Integrating Eq. (9.103) over this time span gives the following prescription for optimum core parameters

$$N A_c (B_s + B_r) = V_o\pi/2\omega. \tag{9.105}$$

Power compression in the two-stage circuit is, illustrated in Figure 9.46a.
A multiple compression stage circuit with magnetic switching is shown in Figure 9.45b. The parameters of the saturable cores are chosen to transfer energy from one capacitor to the next at increasing power levels. Current waveforms in the switches are shown in Figure 9.46b. There are a number of constraints on power compression circuits:

1.The capacitance in all stages should be equal to C_0 for high efficiency.
2.Switching of each stage should occur at peak energy transfer. This means that

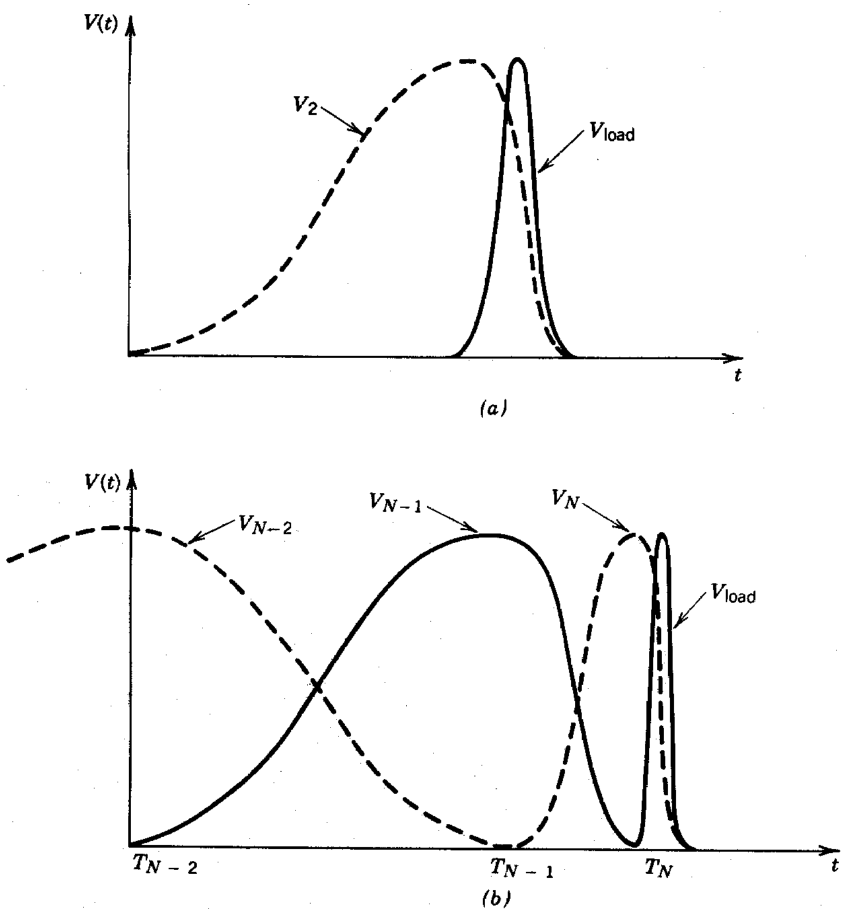

Figure 9.46 Voltage waveforms—saturable core magnetic switching. (*a*) Voltage on charged capacitor and load in single-stage circuit. (*b*) Voltages on last three capacitors and load in multistage network.

$$V_0\pi\ \sqrt{L_{n-1}^{s}\ C_0/2}\ =\ 2N_nA_c(B_s+B_r). \tag{9.106}$$

In Eq. (9.106), L_{n-1}^{s} is the saturated (or vacuum) inductance of the winding around core *n*-1 and N_n is the number of turns around core *n*.

3.The unsaturated inductance of winding *n* should be much larger than the saturated inductance of winding *n*-1, or

$$L_n^{u}\ \gg\ L_{n-1}^{s}. \tag{9.107}$$

Equation (9.107) implies that prepulse is small; power does not move forward in the circuit until switching time.

4. The saturated inductance of winding n should be small compared to the saturated inductance of winding n-1,

$$L_n^u \ll L_{n-1}^u. \tag{9.108}$$

Equation (9.108) guarantees that the time for energy transfer from C_n to C_{n+1} is short compared to the time for energy to flow backward from C_n to C_{n-1}; therefore, most of the energy in the circuit moves forward.

One practical way to construct a multistage power compression circuit is to utilize identical cores (constant A_c, B_s and B_r) and capacitors (constant C_0) and to vary the number of turns around each core to meet the conditions listed above. In this case, the first and second conditions imply that the number of turns decreases geometrically along the circuit or $N_n = B_{n-1}/\kappa$. If we assume that the saturated and unsaturated inductances vary by a factor μ/μ_o, conditions 3 and 4 imply that $\kappa^2 \ll (\mu/\mu_o)$ and $\kappa^2 \gg 1$. These conditions are satisfied if $1 < \kappa < \sqrt{\mu/\mu_o}$.The power compression that can be attained per stage is limited. The time to transfer energy scales as

$$\tau_n/\tau_{n-1} \cong \sqrt{L_n/L_{n-1}} \cong 1/\kappa. \tag{9.109}$$

The power compression ratio is the inverse of Eq. (9.109). For ferrite cores with $\mu/\mu_o \cong 400$, the maximum power compression ratio per stage is about 5.

Magnetic switches in low-power circuits are usually toroidal pulse cores with insulated wire

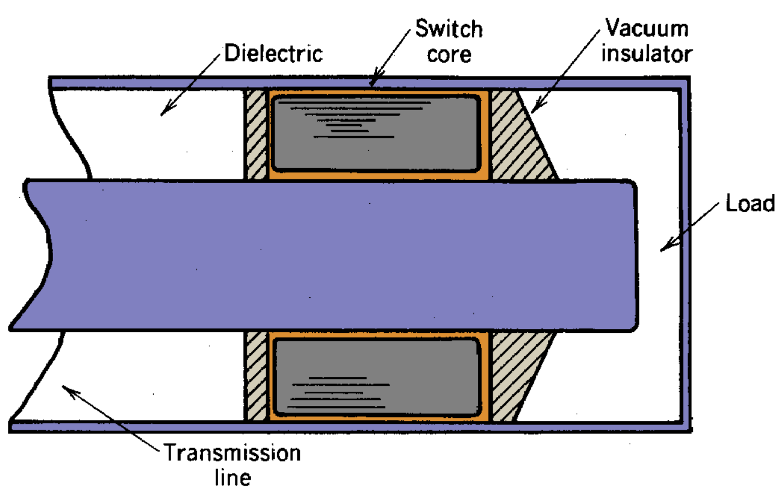

Figure 9.47 Pulse-charged coaxial transmission line with a low-inductance, saturable core magnetic output switch.

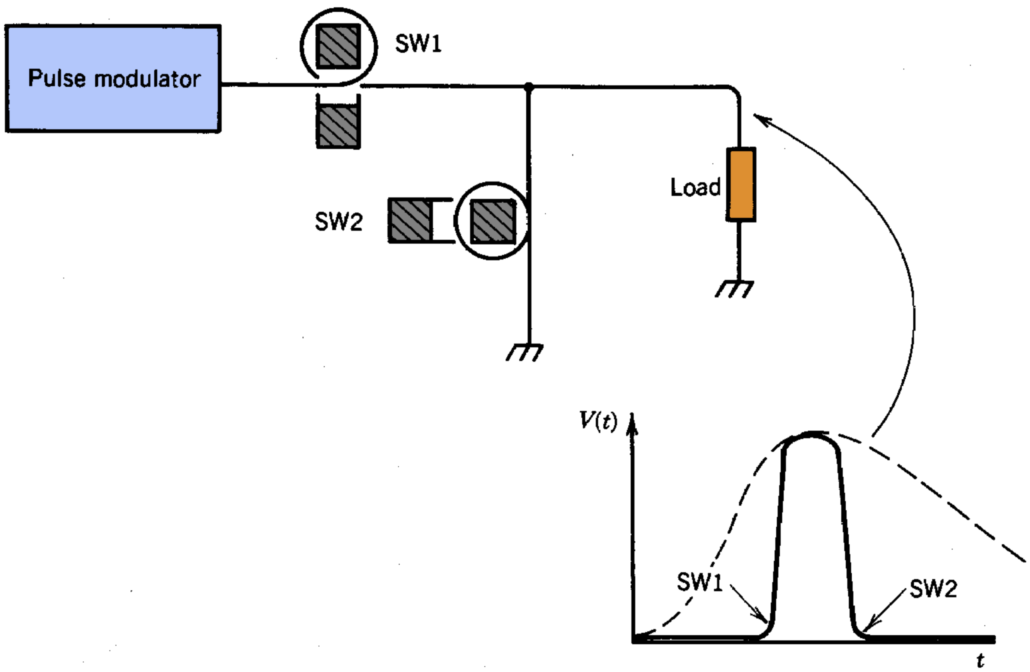

Figure 9.48 Pulse shaping with saturable core magnetic switches.

windings. Magnetic switches used to control the output of a high-power pulse-charged transmission line must be designed for high-voltage standoff and low inductance. A typical configuration is shown in Figure 9.47. Saturable core inductors can also be used for pulselength shortening and risetime sharpening if efficiency is not a prime concern. The circuit illustrated in Figure 9.48 produces a short, fast-rising voltage pulse from a slow pulse generator.

9.14 DIAGNOSTICS FOR PULSED VOLTAGES AND CURRENTS

Accurate measurements of acceleration voltage and beam current are essential in applications to charged particle acceleration. The problem is difficult for pulsed beams because the frequency response of the diagnostic must be taken into account. In this section, we shall consider some basic diagnostic methods.

The diagnostic devices we shall discuss respond to electric or magnetic fields over a limited region of space. For instance, measurement of the current through a resistor gives the instantaneous spatially-averaged electric field over the dimension of the resistor. Confusion often arises when electric field measurements are used to infer a voltage. In particle acceleration applications voltage usually means the energy a charged particle gains or loses crossing the region of measurement. Signals from voltage diagnostics must be carefully interpreted at high frequency because of two effects.

1. Particle energy gain is not equal to $\int \mathbf{E}\cdot d\mathbf{x}$ (where the integral is taken at a fixed time) when the

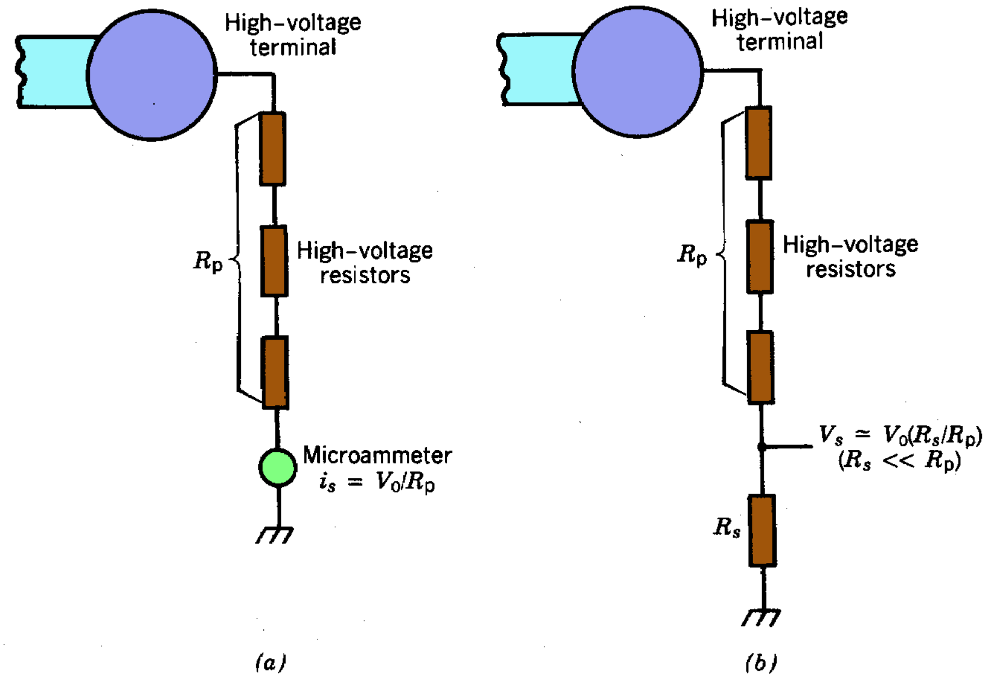

Figure 9.49 High-voltage measurements with resistor strings. (*a*) Resistive shunt. (*b*) Resistive divider.

time interval for the particle to cross the region is comparable to or less than the period of voltage oscillations. This is called the *transit time effect* and is treated in Section 14.4.

2. The voltage difference between two points is not a useful concept when the wavelength of electromagnetic oscillations is less than or comparable to the dimension of the region. In this case, electric field may vary over the length of the diagnostic. For example, in the presence of a bipolar electric field pattern, a voltage diagnostic may generateno signal.

Similarly, magnetic field measurements can be used to infer current flow at low frequency, but caution should be exercised in interpretation at high frequency.

A. Steady-State Voltage Mesurement

The only, time-independent device that can measure a dc voltage is the resistive shunt (Fig. 9.49a). The resistive shunt consists of a resistor string of value R_p attached between the measurement point and ground. The quantity R_p must be high enough to prevent overloading the voltage source or overheating the resistors. The net voltage can be inferred by measuring current flow through the chain with a microammeter,

$$i_s = V_0/R_p. \tag{9.110}$$

Another approach is to measure the voltage across a resistor R_s at the low-voltage end of the chain. This configuration is called a *resistive divider* (Fig. 9.49b). The division ratio, or the signal voltage divided by the measured voltage, is

$$V_s/V_0 = R_s / (R_p + R_s). \tag{9.111}$$

Capacitive voltage measurements of dc voltages are possible if there is a time variation of capacitance between the source and the diagnostic. The charge stored in a capacitance between a high-voltage electrode and a diagnostic plate (C_p) is

$$Q = C_p V_0.$$

The total time derivative of the charge is

$$i_s = dQ/dt = C_p \ (dV_0/dt) + V_0 \ (dC_p/dt). \tag{9.112}$$

In pulsed voltage measurements, C_p is maintained constant and a diagnostic current is generated by dV_0/dt. Measurements of dc voltages can be performed by varying the capacitance as indicated by the second term on the right-hand side of Eq. (9.112).

The voltage probe of Figure 9.50 has an electrode exposed to electric fields from a high-voltage terminal. A rotating grounded disc with a window changes the mutual capacitance between the probe and high-voltage electrodes, inducing a current. The following example of a voltage measurement on a Van de Graaff accelerator illustrates the magnitude of the signal current. Assume the high-voltage electrode is a sphere of radius R_o in a grounded spherical chamber of radius R_1. With gas insulation, the total capacitance between the outer and inner electrodes is

$$C_t \cong 4\pi\varepsilon_o R_0 R_1/(R_1 - R_0). \tag{9.113}$$

We assume further that the probe electrode and rotating window are near ground potential and that their surfaces are almost flush with the surface of the outer electrode. Field lines between the high-voltage electrode and the probe are radial; therefore, the mutual capacitance is equal to C_t times the fraction of outer electrode area occupied by the probe. If A_p is the area of the hole in the rotating plate, then the capacitance between the high-voltage electrode and probe varies between

$$0 \le C_p \le C_t \ A_p/4\pi R_1^2.$$

As an example, take V_0 = 1 MV, R_0 = 0.3 m, R_1 = 1 m, and $A_p = 8 \times 10^{-3}$ m^2. A plate, rotating at 1000 rmp (ω = 100 s^{-1}) obscures the probe half the time. The total spherical capacitance is C_t =

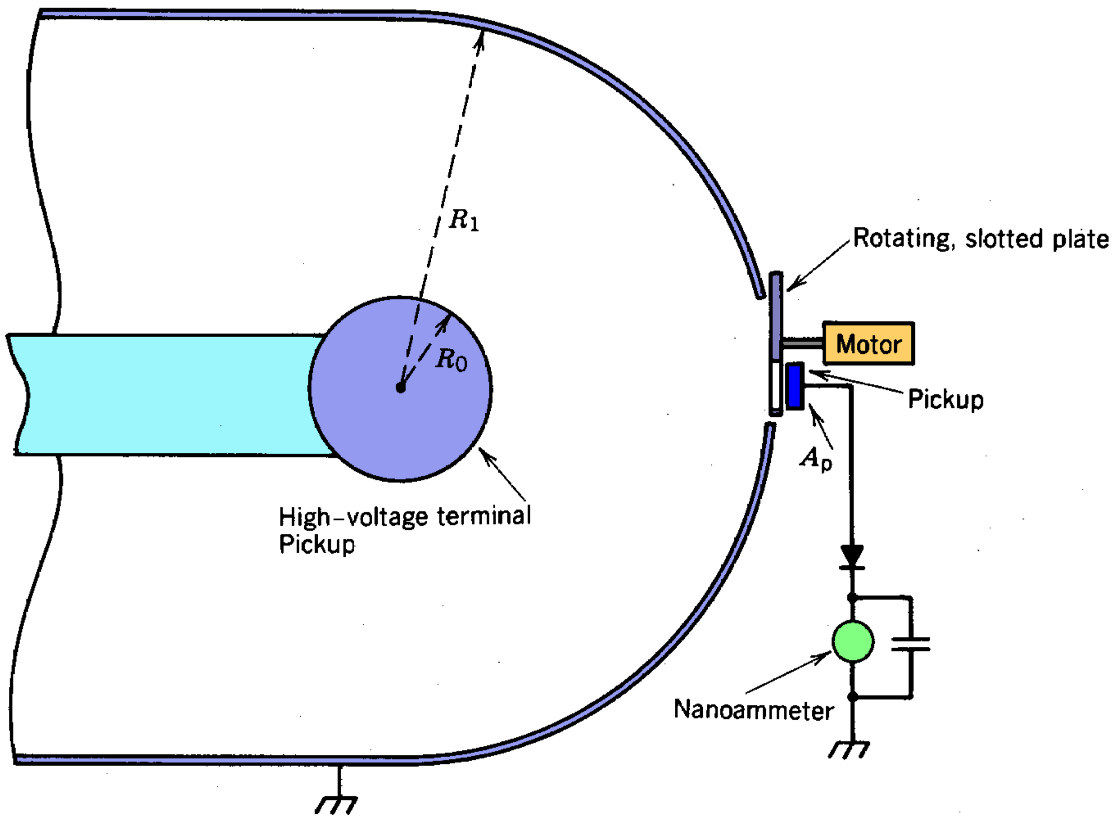

Figure 9.50 Generating voltmeter; high-voltage probe with time-varying capacitance.

100 pF; the mutual capacitance between terminal and probe is 0.07 pF. The signal current is approximately $i_s \cong V_0\ (\omega C_p/2)\ \cos\omega t$. Substituting values, the magnitude of the ac current is 3.5 μA, an easily measured quantity.

B. Resistive Dividers for Pulsed Voltages

T'he electrostatic approximation is usually applicable to the measurements of output voltage for pulsed power modulators. For example, electromagnetic waves travel 15 m in vacuum during a 50-ns pulse. The interpretation of voltage monitor outputs is straightforward as long as the dimensions of the load and leads are small compared to this distance.

Resistive dividers are well suited to pulsed voltage measurements, but some care must be exercised to compensate for frequency-dependent, effects. Consider the divider illustrated in Figure 9.49. Only the resistance values are important for dc measurements, but we must include effects of capacitance and inductance in the structure for pulsed measurements. A more detailed circuit model for the resistive divider is shown in Figure 9.51. There is inductance associated with current flow through the resistors and a shunt capacitance between points on the divider.

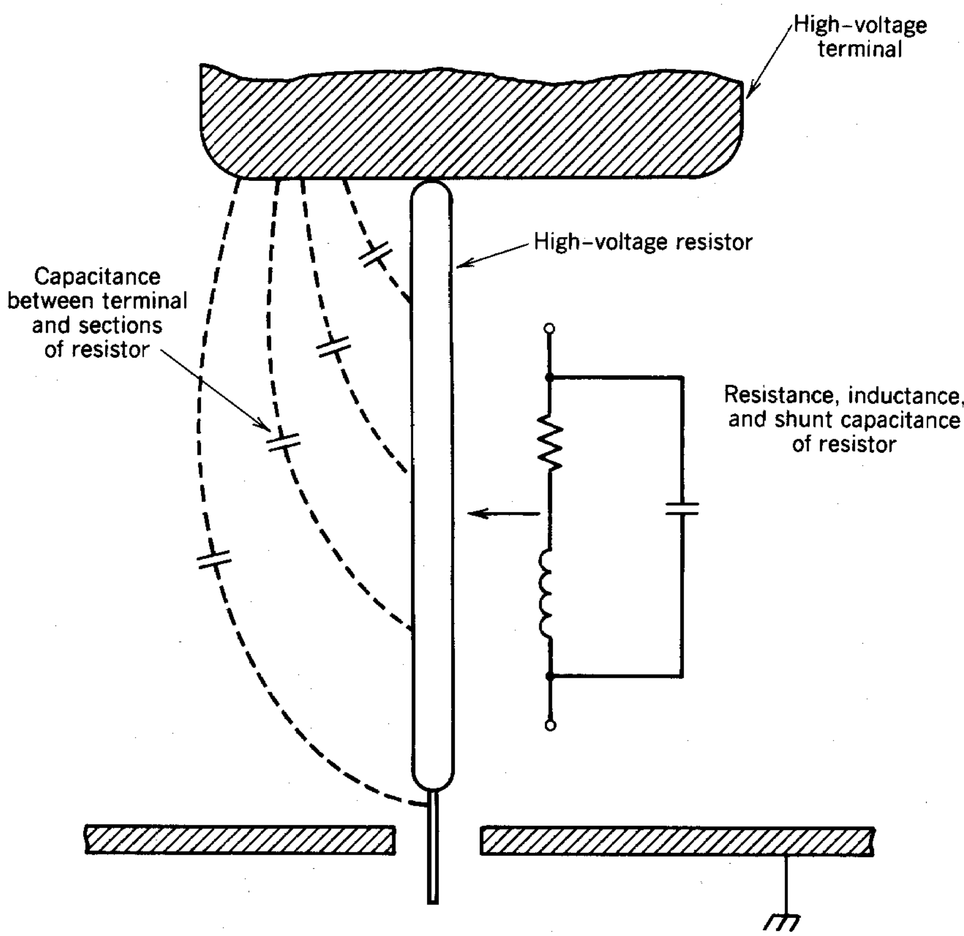

Figure 9.51 Effect of stray capacitance, shunt capacitance, and series inductance on resistive voltage divider.

A particularly unfavorable situation occurs when the primary resistor chain is a water solution resistor and the signal resistor is an ordinary carbon-composition resistor. Water resistors have high dielectric strength and good energy-absorbing ability, but they also have a large shunt capacitance, C_p. Therefore, on time scales less than R_0C_p, the circuit acts as a differentiator. A square input pulse gives the pulse shape shown in Figure 9.52b.

The above example illustrates a general problem of pulsed voltage attenuators; under some circumstances, they may not produce a true replication of the input waveform. We can understand the problem by considering the diagnostic as a device that transforms an input waveform to an output waveform. We can represent the process mathematically by expressing the input signal as a Fourier integral,

$$V_0(t) = \int a(\omega)\ \exp(j\omega t), \tag{9.114}$$

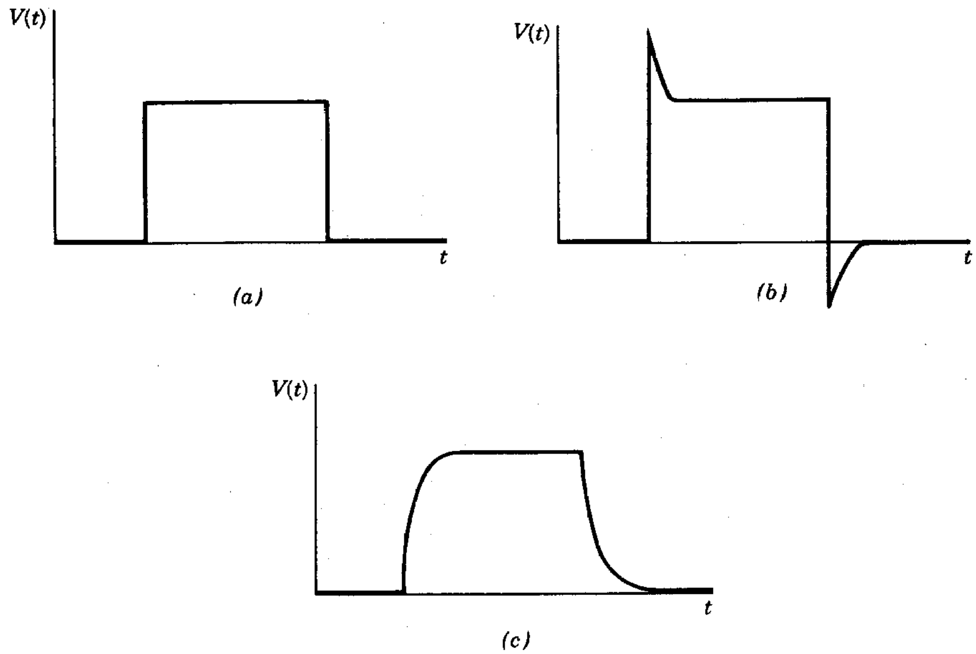

Figure 9.52 Waveforms from resistive voltage divider. (*a*) Ideal output voltage from a square-pulse input. (*b*) Output with significant shunt capacitance. (*c*) Output with significant series inductance.

where $a(\omega)$ is a complex number. Neglecting the electromagnetic transit time through the diagnostic, the transform function of a diagnostic system is a function of frequency, $g(\omega)$. The quantity $g(\omega)$ is a complex number, representing changes in amplitude and phase. The output signal is

$$V_s(t) = \int a(\omega)\ g(\omega)\ \exp(j\omega t). \tag{9.115}$$

In an ideal diagnostic, the transformation function is a real number independent of frequency over the range of interest. When this condition does not hold, the shape of the output signal differs from the input. In the case of the water solution resistive divider, $g(\omega)$ is constant at low frequency but increases in magnitude at high frequency. The result is the spiked appearance of Figure 9.52b. Conversely, if the inductance of the divider stack is a dominant factor, high frequencies are inhibited. The pulse risetime is limited to about L/R_0, producing the pulse shown in Figure 9.52c.

Pulse shapes can often be reconstructed by computer if the transfer function for a diagnostic and the associated cabling is known. Nonetheless, the best practice is to design the diagnostic for flat frequency response. Devices with frequency variations must be compensated. For example, consider the water solution resistive divider. A method of compensation is evident if we recognize that pulsed voltage dividers can be constructed with capacitors or inductors. In the capacitive divider (Fig. 9.53a), the division ratio is

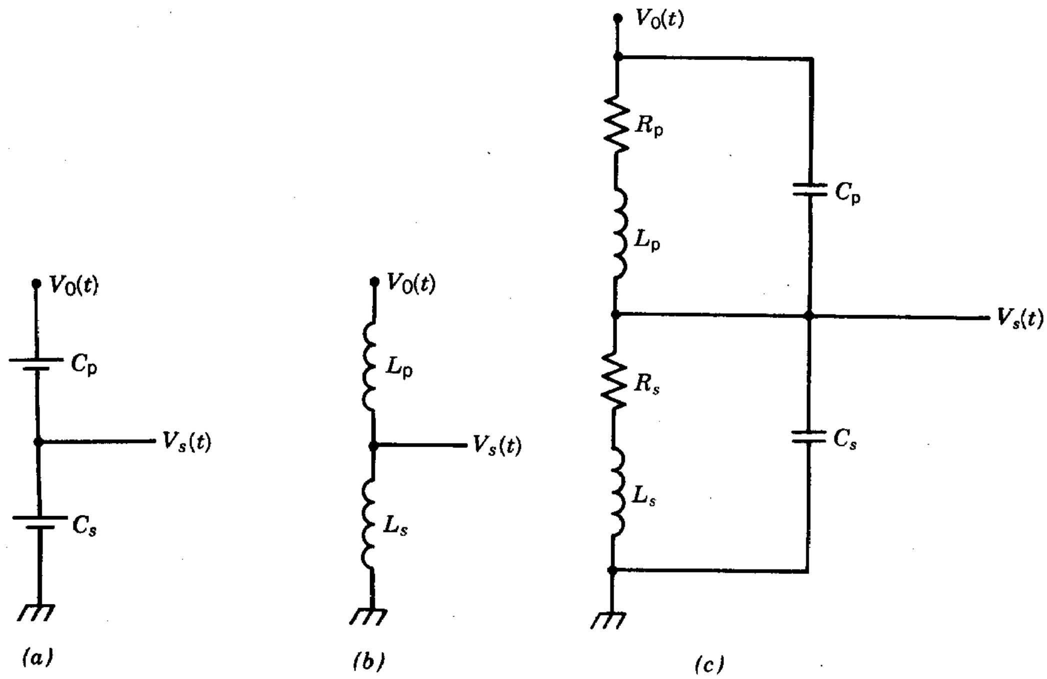

Figure 9.53 Voltage dividers. (*a*) Capacitive. (*b*) Inductive. (*c*) Balanced voltage divider.

$$V_s/V_0 = C_p/(C_s+C_p), \tag{9.116}$$

and for an inductive divider (Fig. 9.53b),

$$V_s/V_0 = L_s/(L_s+L_p), \tag{9.117}$$

A balanced divider is illustrated in Figure 9.53c. Extra circuit components (C_s and L_s) have been added to the probe of Figure 9.51 to compensate for the capacitance and inductance of the probe. The divider is balanced if

$$R_s/(R_s+R_p) = C_p/(C_s+C_p) = L_s/(L_s+L_p). \tag{9.118}$$

The component C_s pulls down the high-frequency components passed by C_p eliminating the overshoot of Figure 9.52a. Similarly, the inductance L_s boosts low-frequency components which were over-attenuated by L_p to improve the risetime of Figure 9.52b. Sometimes, C_p and L_p are not known exactly, so that variable C and L are incorporated. These components are adjusted to give the best output for a fast-rising square input pulse.

Divider balance can also be achieved through geometric symmetry. A balanced water solution resistive divider is shown in Figure 9.54. The signal pick-off point is a screen near the ground plane. The probe resistor and signal resistor, R_p and R_s, share the same solution. The division ratio

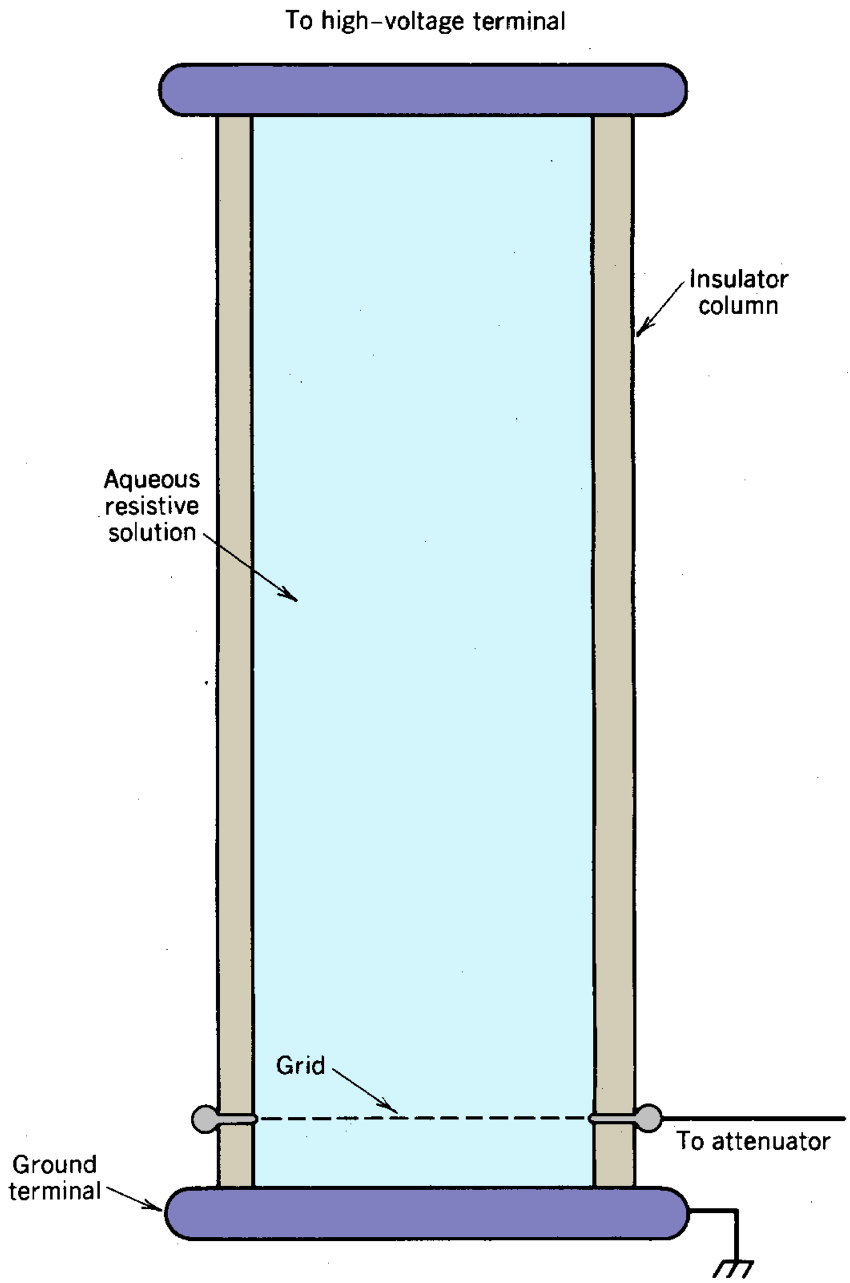

Figure 9.54 Balanced voltage divider with water solution resistor.

is given by the ratio of the length of R_s to the length of R_p. The high dielectric constant of the water solution assures that electric field fines in the water are parallel to the column [see Eq. (5.6)]. Inspection of Figure 9.54 shows that the resistances, capacitances, and inductances are all in the proper ratio for a balanced divider when the solution resistance, resistor diameter, and electric field are uniform along the length of the resistor.

C. Capacitive Dividers for Pulsed Voltages

High-voltage dividers can be designed with predominantly capacitive coupling to the high-voltage electrode. Capacitive probes have the advantage that there is no direct connection and there are negligible electric keld perturbations. Two probes for voltage measurements in high-voltage transmission lines are shown in Figures 9.55a and b.

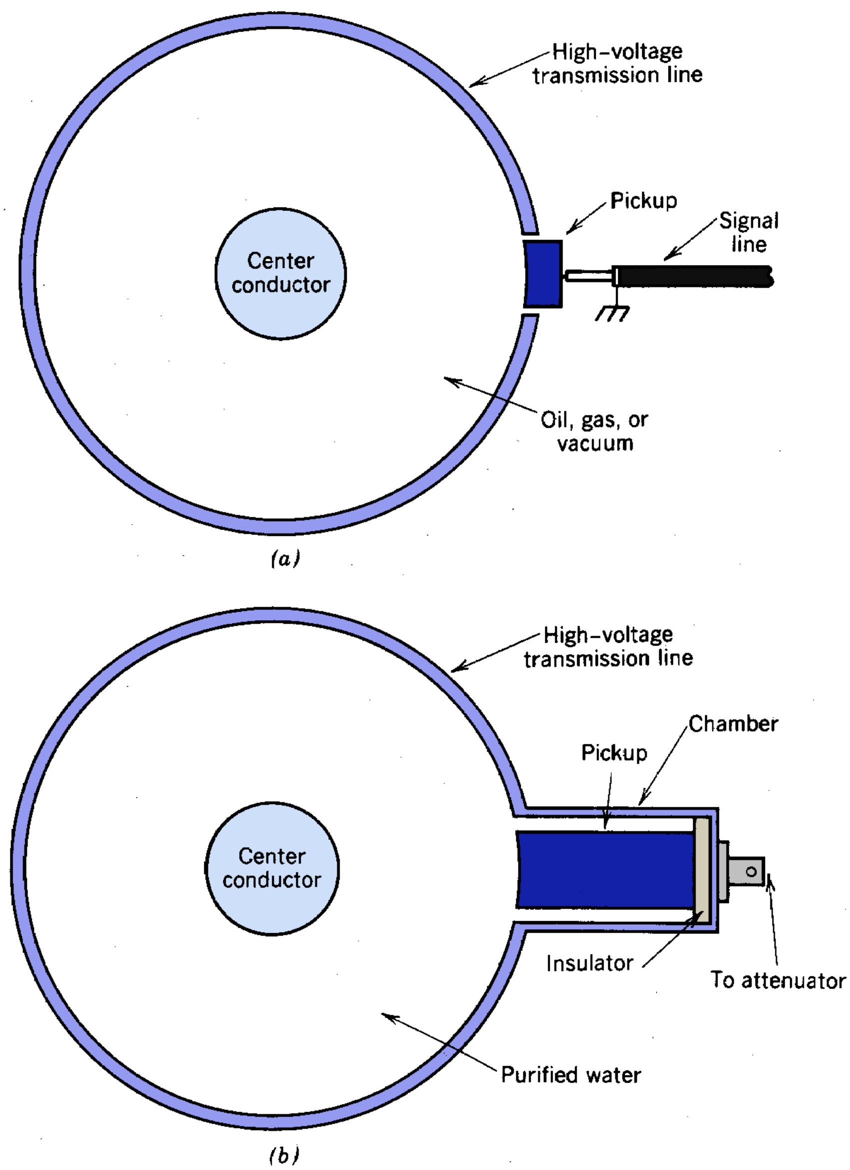

Figure 9.55 Capacitive voltage monitors in high-voltage transmission line. (*a*) Capacitive dV/dt pickup. (*b*) Balanced capacitive divider.

T'he first probe is suitable for use in an oil or gas-filled line where the resistance of the medium is effectively infinite and the mutual capacitance between terminal and probe is low. The capacitance between the probe and the wall, C_s, is purposely made small. The probe is connected directly to a signal transmission line of impedance Z_o. The signal voltage on the line is

$$V_s \cong (C_p Z_o)\ (dV_0/dt). \tag{9.119}$$

This signal is processed by an integration circuit (Section 9.1). The minimum time response of the probe is about $Z_o C_s$. The maximum time is determined by the integration circuit.

The second probe is a self-integrating.probe for use in water-filled transmission lines. The coupling capacitance is high in water lines; in addition, there is real current flow because of the non-zero conductance. In this situation, the capacitance between the probe and the wall is made high by locating the probe in a reentrant chamber. The probe acts as a capacitive divider rather than a coupling capacitor. If the space between between the probe electrode and the wall of the chamber is filled with a non-conductive dielectric, the divider is unbalanced because of the water resistance. Balance can be achieved if the water of the transmission line is used as the dielectric in the probe chamber. The minimum time response of the divider is set by electromagnetic pulse transit time effects in the probe chamber. Low-frequency response is determined by the input resistance of the circuit attached to the probe. If R_d is the resistance, then the signal of a square input pulse will droop as $\exp(-t/R_d C_s)$. Usually, a high series R_d is inserted between the transmission line and the probe to minimize droop and further attenuate the signal voltage.

D. Pulsed Current Measurements with Series Resistors

Measurements of fast-pulsed beam flux or currents in modulators are usually performed with either series resistors, magnetic pickup loops, or Rogowski loops. A typical series resistor configuration for measuring the current from a pulsed electron gun is shown in Figure 9.56a. Power is supplied from a voltage generator through a coaxial transmission line. The anode is connected to the return conductor through a series resistor called a *current-viewing resistor* (CVR). Current is inferred from the voltage across the resistor. The CVR has low resistance, R_s, and very low series inductance. In many cases, diagnostic cables and power leads are connected to the anode. In this situation, some circuit current flows through the ground connectors of the cables, ultimately returning to the generator. This current does not contribute to a signal on the CVR. The current loss is minimized if the inductance associated with the loss paths is large compared to the series inductance of the CVR. When this condition holds, most of the primary circuit current flows through the CVR for times short compared to L/R_s, where L is the inductance along the connecting cables.

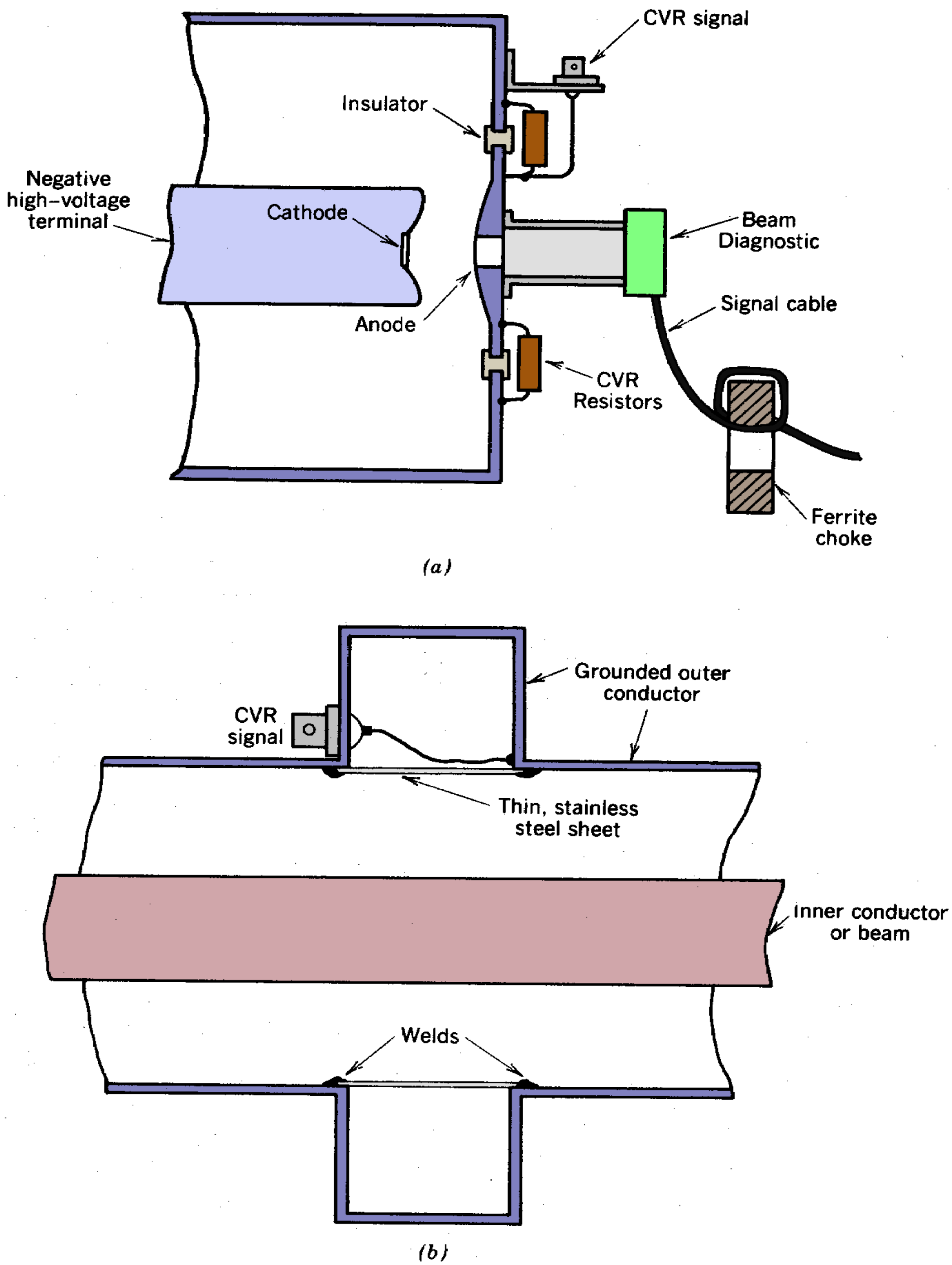

Figure 9.56 Current-viewing resistors. (*a*) Typical arrangement for current measurements from a pulsed electron injector with inductive isolation for beam diagnostics. (*b*) Low-inductance CVR for high-power transmission line or beamline.

A design used for commercial CVRs is shown in Figure 9.56b. The diagnostic is mounted on the return conductor of a coaxial transmission line. It consists of a toroidal chamber with a thin sheet of stainless steel welded across the opening to preserve the cylindrical geometry. In the absence of the resistive sheet, current flow generates a magnetic field inside the chamber; there is an inductance L_s, associated with the convoluted path of return current. When a sheet with resistance R_s, is added, current flows mainly through the sheet for times less than L_s/R_s. When this condition holds, voltage measured at the pick-off point is approximately equal to iR_s. The response of the CVR can be extended to lower frequencies by the inclusion of a ferromagnetic material such as ferrite in the toroidal chamber. The principle of operation of the ferrite-filled probe will be clear when we study inductive linear accelerators in the next chapter.

E. Pulsed Current Measurements with Magnetic Pickup Loops

The magnetic pickup loop measures the magnetic field associated with current flow. It consists of a loop normal to the magnetic field of area A with N turns. If the signal from the loop is passed through a passive integrator with time constant RC, then the magnetic field is related to the integrator output voltage by

$$V_s = NAB/RC. \tag{9.120}$$

Current can be inferred if the geometry is known. For instance, if the current is carried by the center conductor of a transmission line or a cylindrically symmetric beam on axis, the magnetic field at a probe located a distance r from the axis is given by Eq. (4.40). The loop is oriented to sense toroidal magnetic fields.

The net current of a beam can be determined even if the beam moves off axis by adding the signals of a number of loops at different azimuthal positions. Figure 9.57 shows a simple circuit to add and integrate the signals from a number of loops. Magnetic pickup loops at diametrically opposite positions can detect beam motion off-axis along the diameter. In this case, the loop signals are subtracted to determine the difference signal. This is accomplished by rotating one of the loops 180° and adding the signals in the circuit of Figure 9.57.

The high-frequency response of a magnetic pickup loop is determined by the time it takes magnetic fields to fill the loop. The loop is diamagnetic; currents induced by changing flux produce a counterflux. The response time for a loop with inductance L and a series resistance R is L/R. The resistance is usually the input impedance of a transmission line connected to a loop. Sensitive magnetic pickup loops with many turns generally have slow time response.

The magnetic pickup loop has a useful application in pulsed -voltage systems when the voltage diagnostic cannot be attached at the load. For instance, in driving a high-current electron extractor with a transmission line modulator, it may be necessary to measure voltage in the line rather than at the vacuum load. If there is inductance L between the measurement point and the acceleration gap,

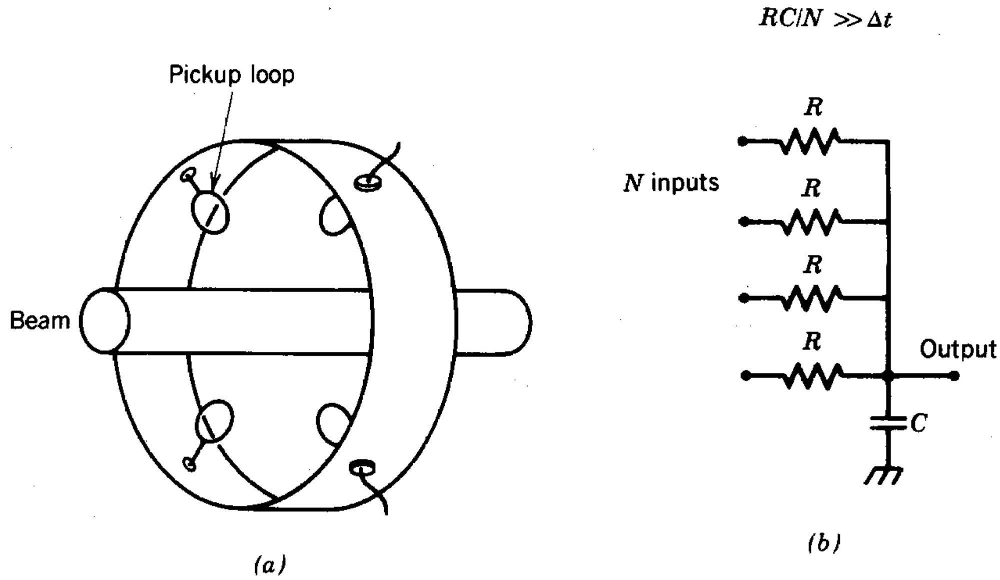

Figure 9.57 (*a*) Multiple magnetic pickup loops for measurements of net beam current or beam position. (*b*) Passive integrator with provision for adding (or subtracting) probe signals.

the actual voltage on the gap is

$$V_g(t) = V_0(t) - L_p\ (di/dt). \tag{9.121}$$

The quantity V_0 is the voltage at the measurement point and V_g is, the desired voltage. A useful measurement can often be achieved by adding an inductive correction to the signal voltage. An unintegrated magnetic pickup loop signal (proportional to $-di/dt$) is added to the uncorrected voltage through a variable attenuator. The attenuator is adjusted for zero signal when the modulator drives a shorted load. The technique is not reliable for time scales comparable to or less than the electromagnetic transit time between the measurement point and the load. A transmission line analysis must be used to infer high-frequency correction for the voltage signal.

F. Rogowski Loop

The final current diagnostic we will study is the Rogowski loop (Fig. 9.58). It is a multi-turn toroidal inductor that encircles the current to be measured. When the dimension of the loops is small compared to the major radius, Eq. (4.39) implies that the net flux linking the series of loops does not depend on the position of the measured current inside the loop. Adopting this approximation, we assume the magnetic field is constant over the cross-sectional area of the windings and approximate the windings as a straight solenoid.

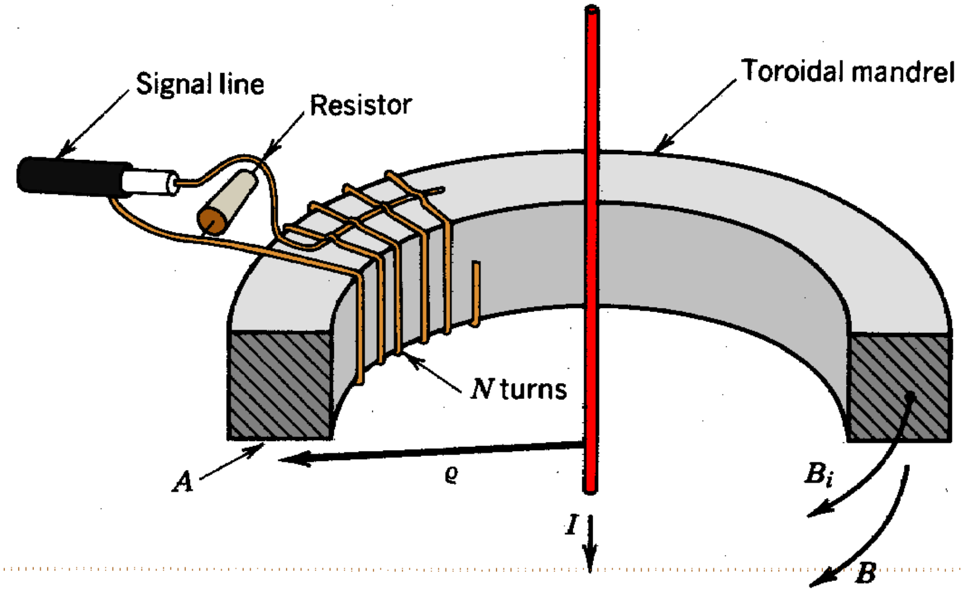

Figure 9.58 Rogowski loop—self-integrating current probe.

The quantity B(t) is the magnetic field produced by the measured current and $B_i(t)$ is the total magnetic field inside the loop. The loop has N windings and a series resistance R at the output. The current flowing in the loop circuit is the total loop voltage divided by R or

$$i(t) = \frac{NA\ (dB_i/dt)}{R}\ . \tag{9.122}$$

The field inside the loop is the applied field minus the diamagnetic field associated with the loop current or

$$B_i(t) = B(t) - \mu_o\ i(t)\ (N/2\pi\rho). \tag{9.123}$$

Substituting Eq. (9.122) into (9.123),

$$(\mu_o N^2 A/2\pi\rho R)\ (dB_i/dt) + B_i = (L/R)\ (dB_i/dt) + B_i = B(t). \tag{9.124}$$

The second form is derived by substituting the expression for the inductance of a toroidal winding, Eq. (9.18). In the limit that the time scale for variations of the measured current I is short compared to L/R, the first term on the left-hand side is large compared to the second term. In this limit very little of the magnetic field generated by the current to be measured penetrates into the winding. Dropping the second term and substituting Eqs. (9.122) and (4.40), we find that

$$i = I/N, \tag{9.125}$$

where i is the loop output current and I is the measured current.
In summary, the Rogowski loop has the following properties:

1. The output signal is unaffected by the distribution of current encircled by the loop.

2. The Rogowski loop is a self-integrating current monitor for time scales $\Delta t \ll L/R$.

3. The probe can respond to high-frequency variations of current.

The low-frequency response of the Rogowski loop can be extended by increasing the winding inductance at the expense of reduced signal. The inductance is increased a factor μ/μ_o by winding the loop on a ferrite torus. In this case, Eq. (9.125) becomes

$$i = \frac{I}{N\ (\mu/\mu_o)}. \tag{9.126}$$

G. Electro-optical Diagnostics

The diagnostics we have considered are basic devices that are incorporated on almost all pulsed voltage systems. There has been considerable recent interest in the use, of electro-optical techniques to measure rapidly varying electric and magnetic fields. The main reason is the increasing, use of digital data acquisition systems. Optical connections isolate sensitive computers from electromagnetic noise, a particular problem for pulsed voltage systems.

A diagnostic for measuring magnetic fields is illustrated in Figure 9.59. Linearly polarized light from a laser is directed through a single-mode, fiber-optic cable. The linearly polarized light wave can be resolved into two circularly polarized waves. A magnetic field parallel to the cable affects the rotational motion of electrons in the cable medium. The consequence is that the index of refraction for right and left circularly polarized waves is different. There is a phase difference between the waves at the end of the cable. The phase difference is proportional to the strength of the magnetic field integrated along the length of the cable, $\int \mathbf{B}\cdot\mathbf{dl}$. When the waves are recombined, the direction of the resulting linearly polarized wave is rotated with respect to the initial wave. This effect is called *Faraday rotation*. The technique can be used for current diagnostics by winding one or more turns of the fiber-optic cable around the measured current path. Equation (4.39) implies that the rotation angle is proportional to the current. Electric fields can be sensed through the Kerr effect or the Pockels effect in an optical medium. Interferometric techniques are used to measure changes in the index of refraction of the medium induced by the fields.

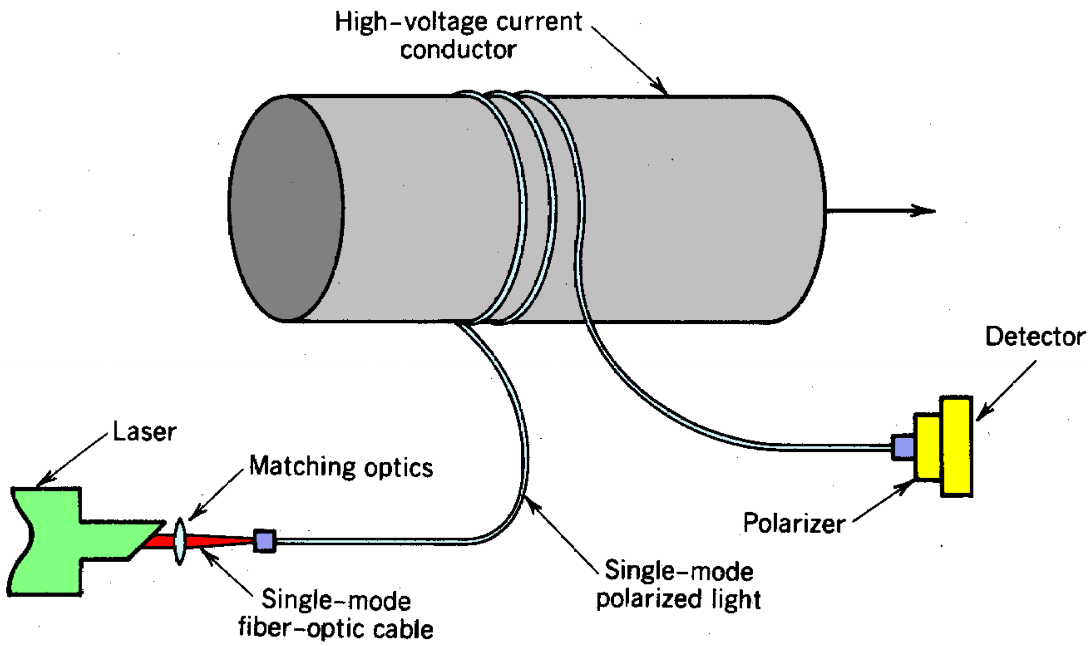

Figure 9.59 Current probe using Faraday rotation of laser-generated light in a fiber-optic cable.

The main drawbacks of electro-optical diagnostics techniques is the cost of the equipment and the complex analyses necessary to unfold the data. In the case of the Faraday rotation measurement, bifringence in ordinary fiber-optic materials complicates the interpretation of the rotation, and extensive computations must be performed to determine the measured current. Electro-optical devices have some unique applications that justify the additional effort, such as the direct measurement of intense propagating microwave fields.

10

Linear Induction Accelerators

The maximum beam energy achievable with electrostatic accelerators is in the range of 10 to 30 MeV. In order to produce higher-energy beams, the electric fields associated with changing magnetic flux must be used. In many high-energy accelerators, the field geometry is such that inductive fields cancel electrostatic fields over most the accelerator except the beamline. The beam senses a large net accelerating field, while electrostatic potential differences in the accelerating structure are kept to manageable levels. This process is called *inductive isolation*. The concept is the basis of linear induction accelerators [N. C. Christofilos *et. al.*, Rev. Sci. Instrum. **35**, 886 (1964)]. The main application of linear induction accelerators has been the generation of pulsed high-current electron beams.

In this chapter and the next we shall study the two major types of nonresonant, high-energy accelerators, the linear induction accelerator and the betatron. The principle of energy transfer from pulse modulator to beam is identical for the two accelerators; they differ mainly in geometry and methods of particle transport. The linear induction accelerator and betatron have the following features in common:

1. They use ferromagnetic inductors for broadband isolation.

2. They are driven by high-power pulse modulators.

3. They can, in principle, produce high-power beams.

4. They are both equivalent to a step-up transformer with the beam acting as the secondary.

In the linear induction accelerator, the beam is a single turn secondary with multiple parallel primary inputs from high-voltage modulators. In the betatron, there is usually one pulsed-power primary input. The beam acts as a multi-turn secondary because it is wrapped in a circle.

The linear induction accelerator is treated first since operation of the induction cavity is relatively easy to understand. Section 10.1 describes the simplest form of inductive cavity with an ideal ferromagnetic isolator. Section 10.2 deals with the problems involved in designing isolation cores for short voltage pulses. The limitations of available ferromagnetic materials must be understood in order to build efficient accelerators with good voltage waveform. Section 10.3 describes more complex cavity geometries. The main purpose is to achieve voltage step-up in a single cavity. Deviations from ideal behavior in induction cavities are described in Sections 10.4 and 10.5. Subjects include flux forcing to minimize unequal saturation in cores, core reset for maximum flux swing, and compensation circuits to achieve uniform accelerating voltage. Section 10.6 derives the electric field in a complex induction cavity. The goal is to arrive at a physical understanding of the distribution of electrostatic and inductive fields to determine insulation requirements. Limitations on the average longitudinal gradient of an induction accelerator are also reviewed. The chapter concludes with a discussion of induction accelerations without ferromagnetic cores. Although these accelerators are of limited practical use, they make an interesting study in the application of transmission line principles.

10.1 SIMPLE INDUCTION CAVITY

We can understand the principle of an induction cavity by proceeding stepwise from the electrostatic accelerator. A schematic of a pulsed electrostatic acceleration gap is shown in Figure 10.1a. A modulator supplies a voltage pulse of magnitude V_0. The pulse is conveyed to the acceleration gap through one or more high-voltage transmission lines. If the beam particles have positive charge ($+q$), the transmission lines carry voltage to elevate the particle source to positive potential. The particles are extracted at ground potential with kinetic energy qV_0. The energy transfer efficiency is optimized when the characteristic impedance of the generator and the parallel impedance of the transmission lines equals V_0/I. The quantity I is the constant-beam current. Note the current path in Figure 10.1a. Current flows from the modulator, along the transmission line center-conductors, through the beam load on axis, and returns through the transmission line ground conductor.

A major problem in electrostatic accelerators is controlling and supplying power to the particle source. The source and its associated power supplies are at high potential with respect to the laboratory. It is more convenient to keep both the source and the extracted beam at ground potential. To accomplish this, consider adding a conducting cylinder between the high-voltage and ground plates to define a toroidal cavity (Fig. 10.1h). The source and extraction point are at the same potential, but the system is difficult to operate because the transmission line output is almost

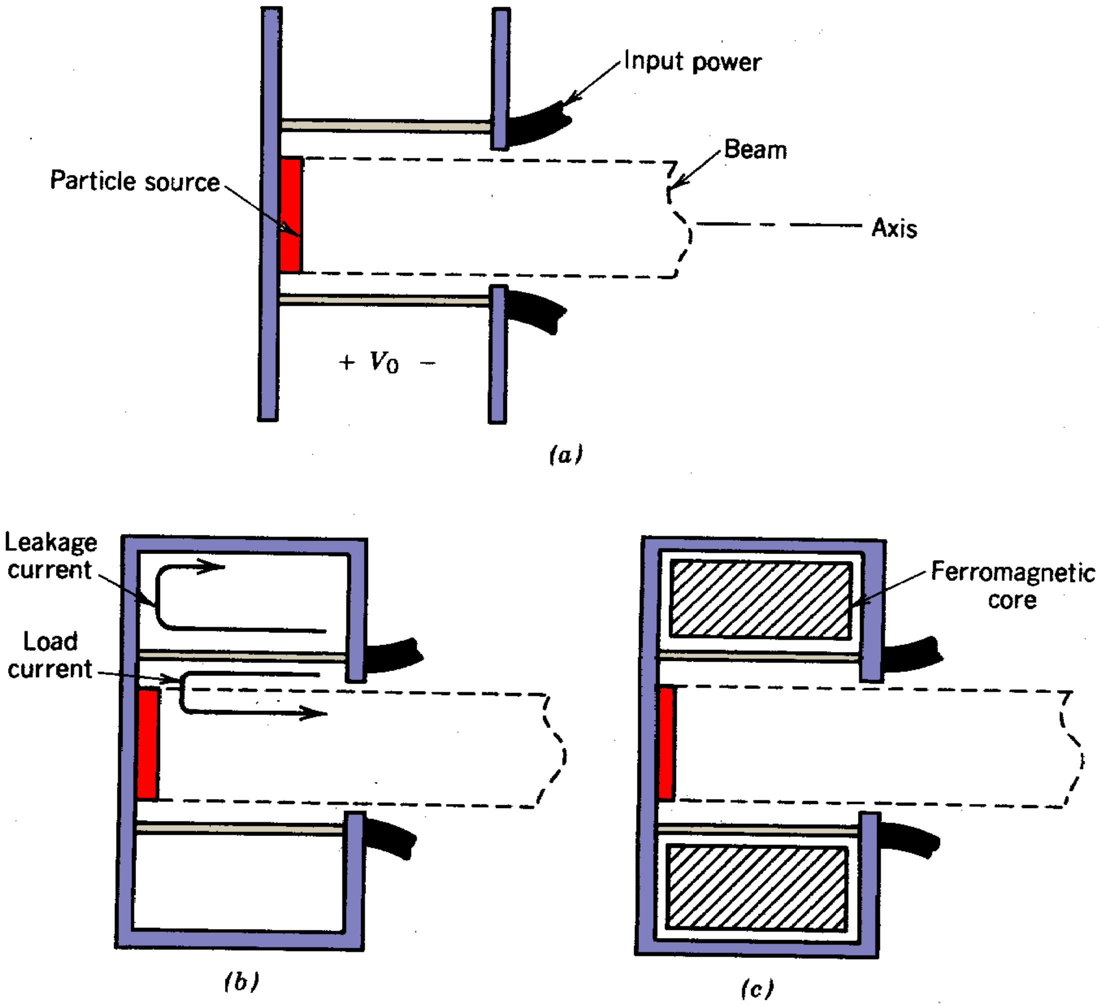

Figure 10.1 Inductively isolated injector cavity. (*a*) Electrostatic injector. (*b*) Shorted electrostatic injector. (*c*) Injector with high-inductance leakage path.

short-circuited. Most of the current flows around the outer ground shield; this contribution is *leakage current*. There is a small voltage across the acceleration gap because the toroidal cavity has an inductance L_1. The leakage inductance is given by Eq. (9.15) if we take R_i as the radius of the power feeds and R_o as the radius of the cylinder. Thus, a small fraction of the total current flows in the load. The goal is clearly to reduce the leakage current compared to the load current; the solution is to increase L_1.

In the final configuration (Fig. 10.1c), the toroidal volume occupied by magnetic field from leakage current is filled with ferromagnetic material. If we approximate the ferromagnetic torus as an ideal inductor, the leakage inductance is increased by a factor μ/μ_o. This factor may exceed 1000. The leakage current is greatly reduced, so that most of the circuit current flows in the load. At constant voltage, the cavity appears almost as a resistive load to the pulse modulator. The voltage waveform is approximately a square pulse of magnitude V_0 with some voltage droop

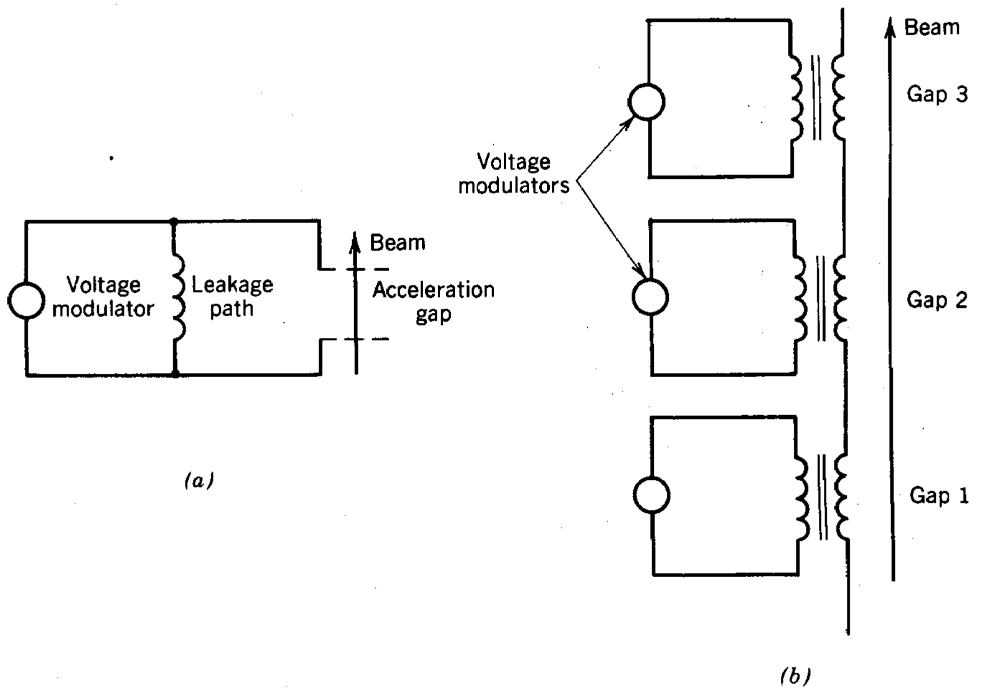

Figure 10.2 Equivalent circuits. (*a*) Inductively isolated acceleration cavity. (*b*) Induction accelerator with a series of cavities.

caused by the linearly growing leakage current. The equivalent circuit model of the induction cavity is shown in Figure 10.2a; it is identical to the equivalent circuit of a 1:1 transformer (Fig. 9.7).

The geometry of Figure 10.1c is the simplest possible inductive linear accelerator cavity. A complete understanding of the geometry will clarify the operation of more complex cavities.

1. The load current does not encircle the ferromagnetic core. This means that the integral $\int \mathbf{H}\cdot\mathbf{dl}$ from load current is zero through the core. In other words, there is little interaction between the load current and the core. The properties of the core set no limitation on the amount of beam current that can be accelerated.

2. To an external observer, both the particle source and the extraction point appear to be at ground potential during the voltage pulse. Nonetheless, particles emerge from the cavity with kinetic energy gain qV_0.

3.The sole purpose of the ferromagnetic core is to reduce leakage current.

4.There is an electrostaticlike voltage across the acceleration gap. Electric fields in the gap are identical to those we have derived for the electrostatic accelerator of Figure 10.1a. The inductive core introduces no novel accelerating field components.

5. Changing magnetic flux generates inductive electric fields in the core. The inductive field at the outer radius of the core is equal and opposite to the electrostatic field; therefore, there is no net electric field between the plates at the outer radius, consistent with the fact that they are connected by a conducting cylinder. The ferromagnetic core provides inductive isolation for the cavity.

When voltage is applied to the cavity, the leakage current is small until the ferromagnetic core becomes saturated. After saturation, the differential magnetic permeability approaches μ_o and the cavity becomes a low-inductance load. The product of voltage and time is limited. We have seen a similar constraint in the transformer [Eq. (9.29)]. If the voltage pulse has constant magnitude V_0 and duration t_p, then

$$V_0 \; t_p \; = \; \Delta B \; A_c. \tag{10.1}$$

where A_c is the cross-sectional area of the core. The quantity ΔB is the change of magnetic field in the core; it must be less than $2B_s$. Typical operating parameters for an induction cavity with a ferrite core are V_0 = 250 kV and t_p = 50 ns. Ferrites typically have a saturation field of 0.2-0.3 T. Therefore, the core must have a cross-sectional area greater than 0.025 m^2.

The most common configuration for an inductive linear accelerator is shown in Figure 10.3. The beam passes through a series of individual cavities. There is no electrostatic voltage difference in

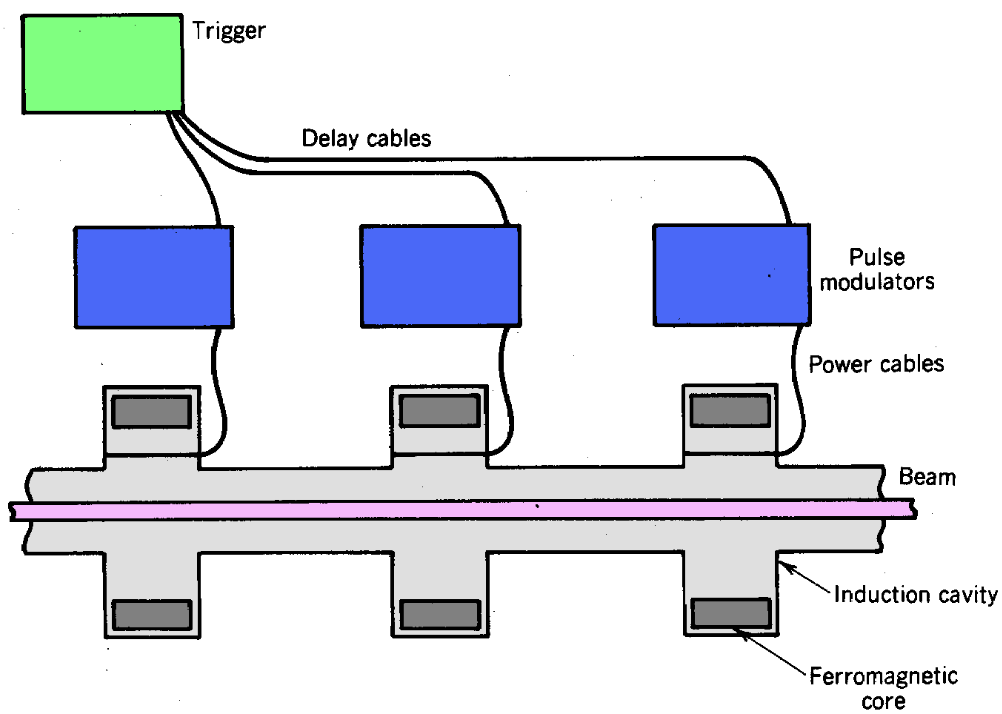

Figure 10.3 Schematic diagram of a linear induction acceleration with cavities in series.

TABLE 10.1 Parameters of the ATA[a] Accelerator

Function	
Research on the propagation of self-focused electron beams in gas, free electron laser driver.	
Configuration	
Length	85 m
Average gradient	0.59 MV/m
Injector	
Voltage	2.5 MV
Voltage source	10 stacked 250-kV induction cavities
Electron source diameter	0.25 m
Configuration	Triode, extraction by high-voltage control grid
Cathode	Cold cathode, whisker emission
Main accelerator	
Voltage gain	47.5 MeV
Voltage per stage	0.25 MV
Number of stages	190
Repetition rate	5 Hz 10 kHz (10 pulse burst)
Acceleration cavity	
Voltage	250 kV
Power modulator	Coaxial, water-filled Blumlein line pulse charged through a 10 : 1 step-up transformer
Modulator impedance	12 Ω
Modulator switch	Gas-blown spark gap
Inductive isolator	Ferrite toroids
Output beam	
Pulselength	70 ns
Energy	50 MeV
Peak current	10 kA

[a] Advanced Test Accelerator, Lawrence Livermore Laboratory.

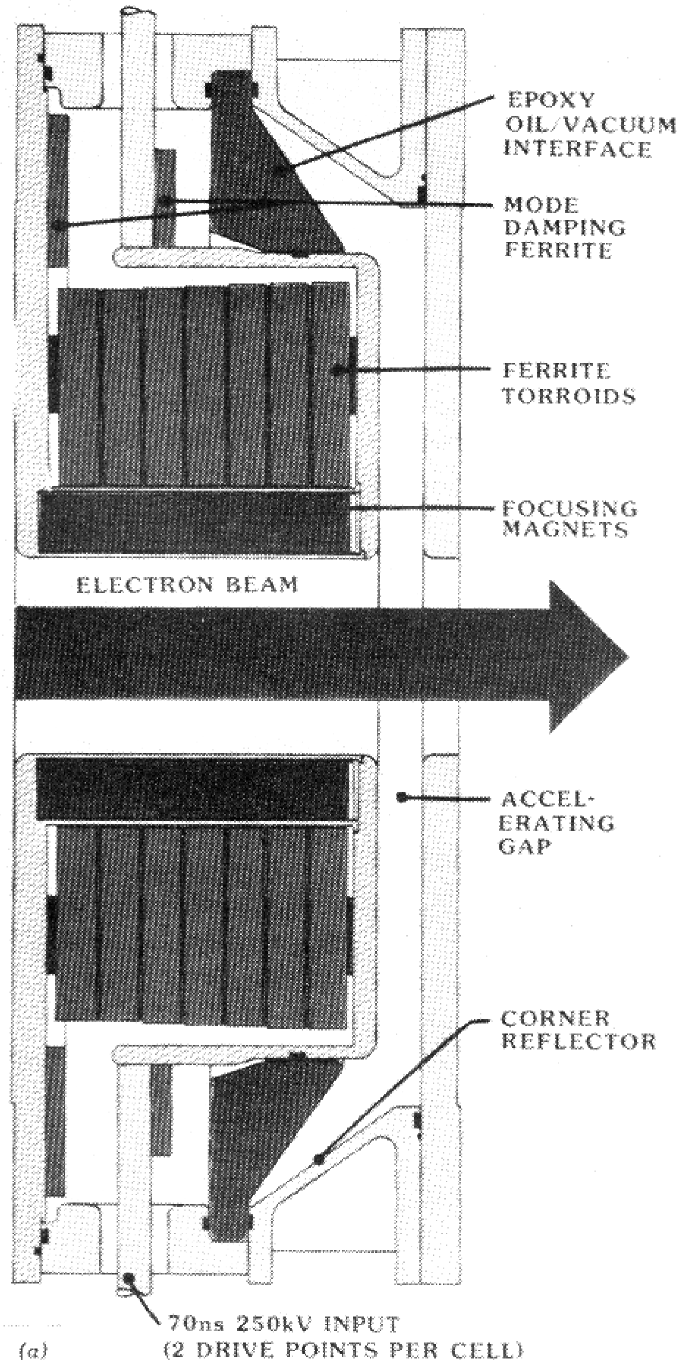

Figure 10.4 Scale drawings, Advanced Test Accelerator. (*a*) 250 kV, ferrite isolated induction cell with mode damping ferrites to minimize beam breakup instabilities. (*b*) 2.5 MV, 10-cell block. (Courtesy D. Prono, Lawrence Livermore Laboratory.)

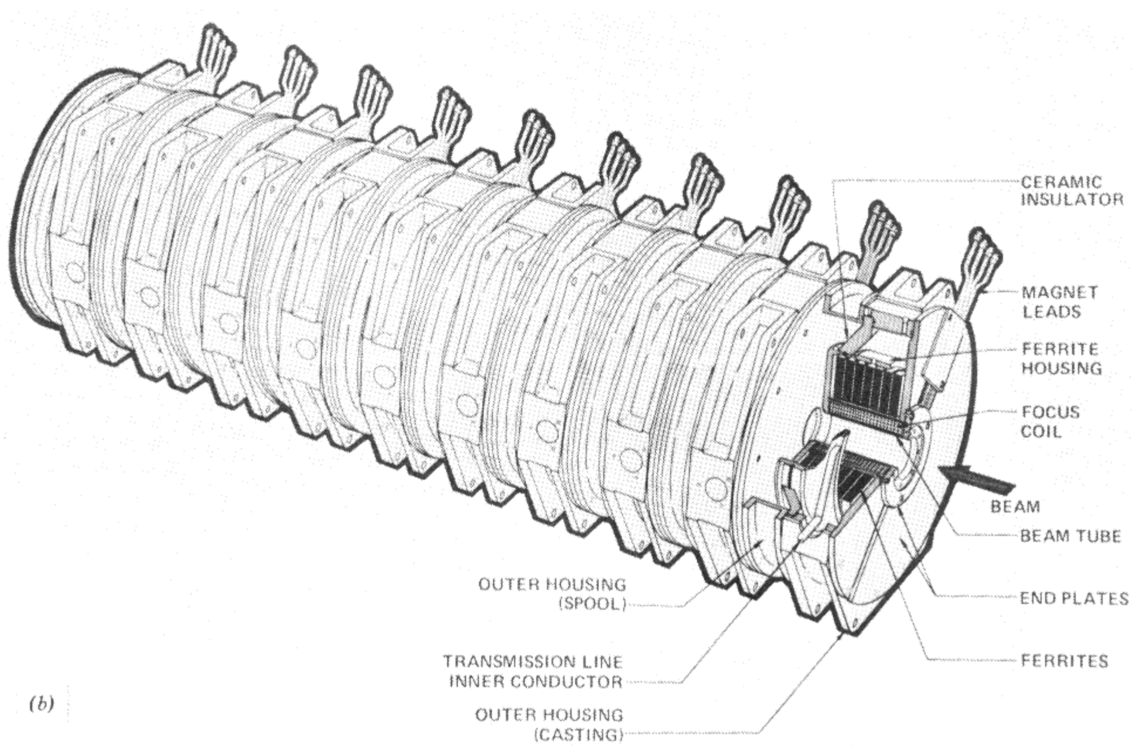

(*b*)

Figure 10.4 (Continued).

the system higher than V_0. Any final beam energy consistent with cost and successful beam transport can be attained by adding more cavities. The equivalent circuit of an induction accelerator is shown in Figure 10.2b. Characteristics of the ATA machine, the highest energy induction accelerator constructed to data, are summarized in Table 10.1. A single-acceleration cavity and a 10-cavity block of the ATA accelerator are illustrated in Figures 10.4a and 10.4b, respectively.

10.2 TIME-DEPENDENT RESPONSE OF FERROMAGNETIC MATERIALS

We have seen in Section 5.3 that ferromagnetic materials have atomic currents that align themselves with applied fields. The magnetic field is amplified inside the material. The alignment of atomic currents is equivalent to a macroscopic current that flows on the surface of the material. When changes in applied field are slow, atomic currents are the dominant currents in the material. In this case, the magnetic response of the material follows the static hysteresis curve (Fig. 5.12).

Voltage pulselengths in linear induction accelerators are short. We must include effects arising from the fact that most ferromagnetic materials are conductors. Inductive electric fields can generate real currents; real currents differ from atomic currents in that electrons move through the material. Real current driven by changes of magnetic flux is called *eddy current*. The contribution of eddy currents must be taken into account to determine the total magnetic fields in materials. In ferromagetic materials, eddy current may prevent penetration of applied magnetic field so that magnetic moments in inner regions are not aligned. In this case, the response of the material deviates from the static hysteresis curve. Another problem is that resistive losses are associated with eddy currents. Depending on the the type of material and geometry of construction, magnetic cores have a maximum usable frequency. At higher frequencies, resistive losses increase and the effective core inductance drops.

Eddy currents in inductive isolators and transformer cores are minimized by laminated core construction. Thin sheets of steel are separated by insulators. Most common ac cores are designed to operate at 60 Hz. In contrast, the maximum-frequency components in inductive accelerator pulses range from 1 to 100 MHz. Therefore, core design is critical for fast pulses. The frequency response is extended either by using very thin laminations or using alternatives to steel, such as ferrites.

The skin depth is a measure of the distance magnetic fields penetrate into materials as a function of frequency. We can estimate the skin depth in ferromagnetic materials in the geometry of Figure 10.5. A lamination of high μ material with infinite axial extent is surrounded by a pulse coil excited by a step-function current waveform. The coil carries an applied current per length J_o (A/m) for $t > 0$. The applied magnetic field outside the high μ material is

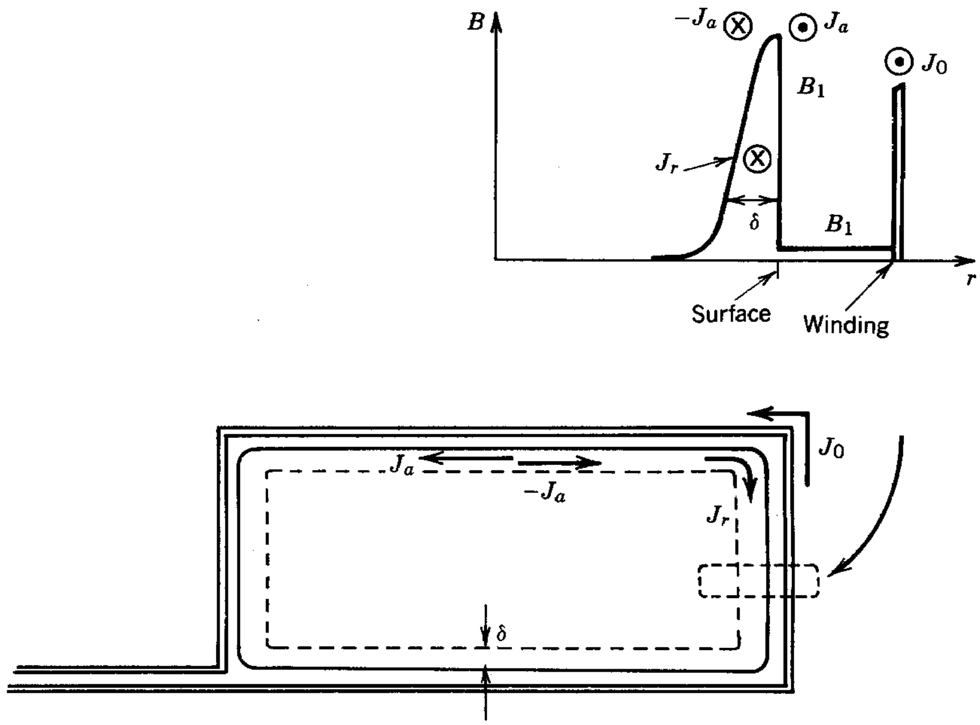

Figure 10.5 Eddy currents and atomic currents in a ferromagnetic lamination subject to a pulsed external magnetic field.

$$B_1 = \mu_o\ J_o. \tag{10.2}$$

A real return current J_r flows in the conducting sample in the opposite direction from the applied current. We assume this current flows in an active layer on the surface of the material of thickness δ. The magnetic field decreases across this layer and approaches zero inside the material. The total magnetic field as a function of depth in the material follows the variation of Figure 10.5. The return current is distributed through the active layer, while the atomic currents are concentrated at the layer surfaces. The atomic current J_a is the result of aligned dipoles in the region of applied magnetic field penetration; it amplifies the field in the active layer by a factor of μ/μ_o. The field just inside the material surface is $(\mu/\mu_o)B_1$. The magnetic field inward from the active layer is zero because the return current cancels the field produced by the applied currents. This implies that

$$J_r \approx -J_o. \tag{10.3}$$

We can estimate the skin depth by making a global balance between resistive effects (which impede the return current) and inductive effects (which drive the return current). The active, layer is assumed to penetrate a small distance into the lamination. The lamination has circumference *C*. If the material is an imperfect conductor with volume resistivity ρ (Ω-m), the resistive voltage around the circumference from the flow of real current is

$$V_r \cong J_r \rho C/\delta. \tag{10.4}$$

The return current is driven by an electromotive force (emf) equal and opposite to V_r. The emf is equal to the rate of change of flux enclosed within a loop at the location under consideration. Because the peak magnetic field $(\mu/\mu_o)B_1$ is limited, the change of enclosed flux must come about from the motion of the active layer into the material. If the layer moves inward a distance δ, then the change of flux inside a circumferential loop is $\Delta\Phi \cong (\mu/\mu_o)B_1C\delta$. Taking the time derivative and using Eq. (4.42), we find the inductive voltage

$$V_i \cong \mu C J_r\ (d\delta/dt).$$

Setting V_i equal to V_r gives

$$C\mu J_r\ (d\delta/dt) \cong J_r \rho C/\delta. \tag{10.5}$$

The circumference cancels out. The solution of Equation (10.5) gives the skin depth

$$\delta = \sqrt{2\rho t/\mu}. \tag{10.6}$$

The magnetic field moves into the material a distance proportional to the square root of time if the applied field is a step function. A more familiar expression for the skin depth holds when the applied field is harmonic, $B_1 \sim \cos(\omega t)$:

$$\delta = \sqrt{2\rho/\mu\omega} \tag{10.7}$$

In this case, the depth of the layer is constant; the driving emf is generated by the time variation of magnetic field.

The two materials commonly used in pulse cores are ferrites and steel. The materials differ mainly in their volume resistivity. Ferrites are ceramic compounds of iron-bearing materials with volume resistivity on the order of 10^4 Ω-m. Silicon steel is the most common transformer material. It is magnetically soft; the area of its hysteresis loop is small, minimizing hysteresis losses. Silicon steel has a relatively high resistivity compared to other steels, 45×10^{-8} Ω-m. Nickel steel has a higher resistivity, but it is expensive. Recently, noncrystalline iron compounds

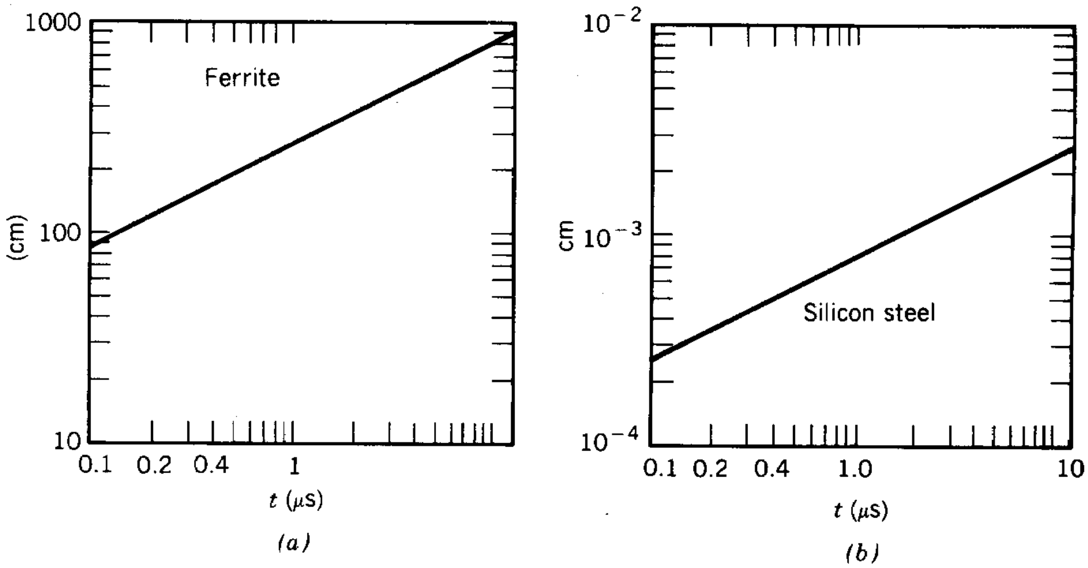

Figure 10.6 Typical values of small-signal skin depth. (*a*) Ferrite. (*b*) Silicon steel.

have been developed. They are known by the tradename Metglas [Allied Corporation]. Metglas is produced in thin ribbons by injecting molten iron compounds onto a cooled, rapidly rotating drum. The rapid cooling prevents the formation of crystal structures. Metglas alloy 2605SC has a volume resistivity of 125×10^{-8} Ω-m. Typical small-signal skin depths for silicon steel and ferrites as a function of applied field duration are plotted in Figure 10.6. There is a large difference between the materials; this difference is reflected in the construction of cores and the analysis of time-dependent effects.

An understanding of the time-dependent response of ferromagnetic materials is necessary to determine leakage currents in induction linear accelerators. The leakage current affects the efficiency of the accelerator and determines the compensation circuits necessary for waveform shaping. We begin with ferrites. In a typical ferrite isolated accelerator, the pulselength is 30-80 ns and the core dimension is < 0.5 m. Reference to Figure 10.6 shows that the skin depth is larger than the core; therefore, to first approximation, we can neglect eddy currents and consider only the time variation of atomic currents. A typical geometry for a ferrite core accelerator cavity is shown in Figure 10.7. The toroidal ferrite cores are contained between two cylinders of radii R_i and R_o. The leakage current circuit approximates a coaxial transmission line filled with high μ material. The transmission line has length d; it is shorted at the end opposite the pulsed power input. We shall analyze the transmission line behavior of the leakage current circuit with the assumption that $(R_o - R_i)/R_o \ll 1$. Radial variations of toroidal magnetic field in the cores are neglected.

The transmission line of length d has impedance Z_c given by Eq. (9.86) and a relatively long transit time $\delta t = d\sqrt{\epsilon\mu}$. Consider, first, application of a low-voltage step-function pulse. A voltage wave from a low-impedance generator of magnitude V_0 travels through the core at velocity $c/\sqrt{(\epsilon/\epsilon_o)(\mu/\mu_o)}$ carrying current V_0/Z_c. The wave is reflected at time Δt with inverse

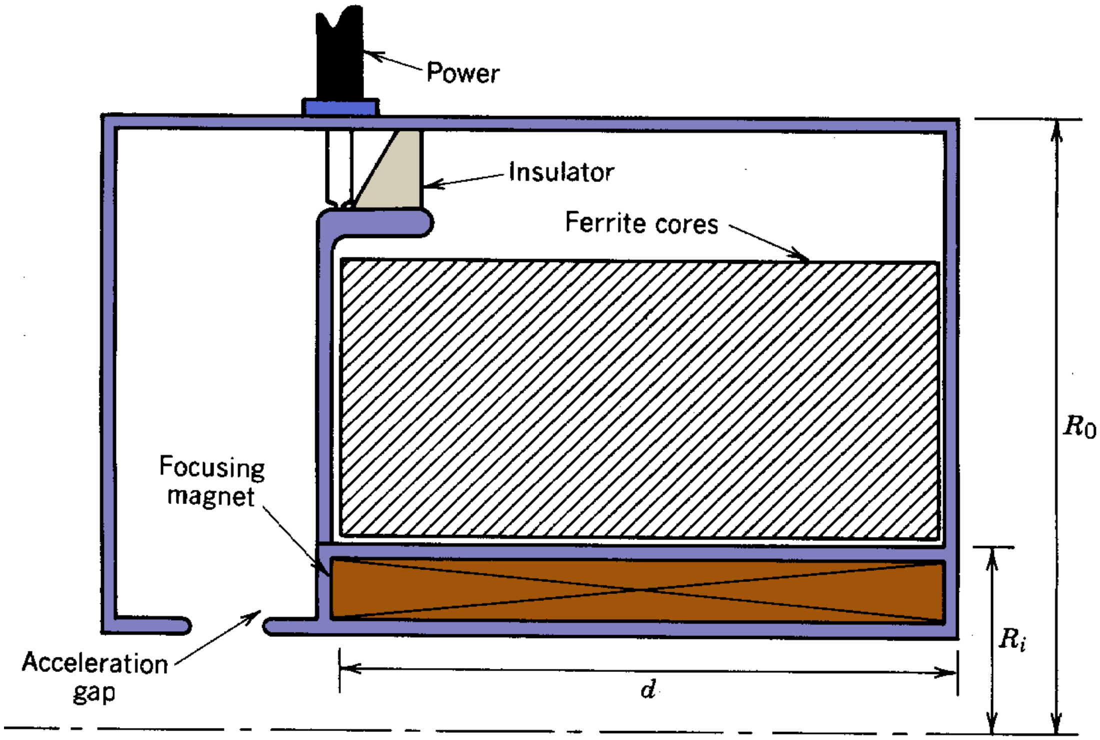

Figure 10.7 Geometry of an idealized ferrite core acceleration cavity.

polarity from the short-circuit termination. The inverted wave arrives back at the input at time

$2\Delta t$. In order to match the input voltage, two voltage waves, each carrying current V_0/Z_c are launched on the line. The net leakage current during the interval $2\Delta t \le t \le 4\Delta t$ is $3V_0/Z_c$. Subsequent wave reflections result in the leakage current variation illustrated in Figure 10.8a. The dashed line in the figure shows the current corresponding to an ideal lumped inductor with $L = Z_c\Delta t$. The core approximates a lumped inductor in the limit of low voltage and long pulselength. The leakage current diverges when it reaches the value $i_s = 2\pi R_i H_s$. The quantity H_s is the saturation magnetizing force.

Next, suppose that the voltage is raised to V_s so that the current during the initial wave transit is

$$i = V_s/Z_c = i_s = 2\pi R_i H_s. \tag{10.8}$$

The wave travels through the core at the same velocity as before. The main difference is that the magnetic material behind the wavefront is saturated. When the wave reaches the termination at time Δt, the entire core is saturated. Subsequently, the leakage circuit acts as a vacuum transmission line. The quantities Z_c and Δt decrease by a factor of μ/μ_o, and the current increases rapidly as inverted waves reflect from the short circuit. The leakage current for this case is plotted in Figure 10.8b. The volt-second product before saturation again satisfies Eq. (10.1).

At higher applied voltage, electromagnetic disturbances propagate into the core as a saturation

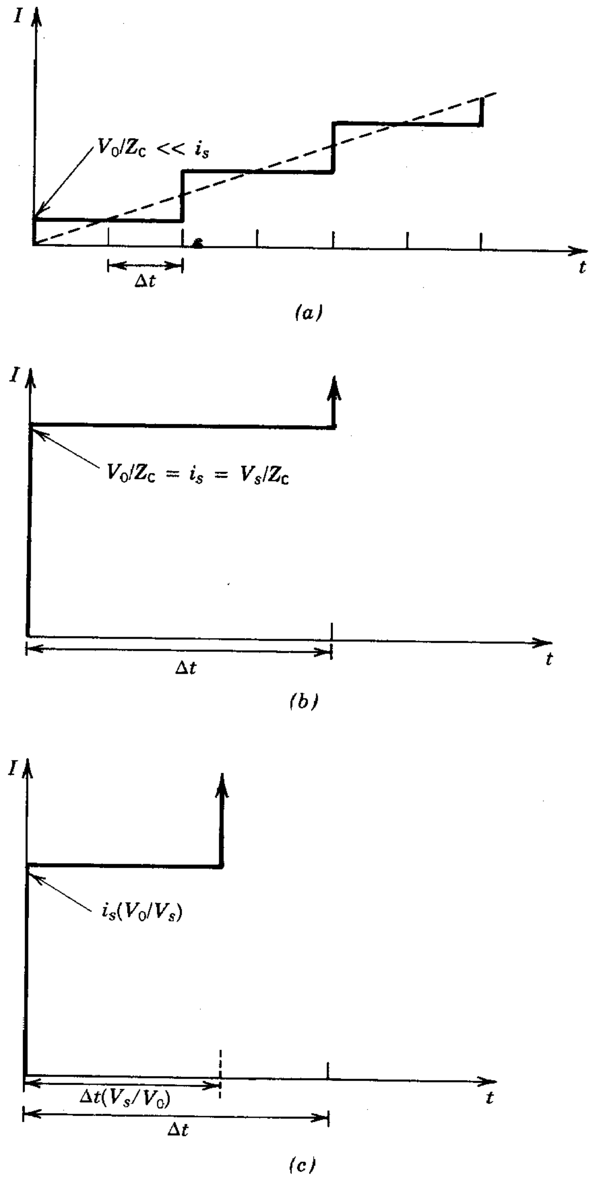

Figure 10.8 Time-dependent leakage current in a ferrite core acceleration cavity. (*a*) Low applied voltage. (*b*) Saturation voltage. (*c*) High voltage.

wave. The wave velocity is controlled by the saturation of magnetic material in the region of rising current; the saturation wave moves more rapidly than the speed of electromagnetic pulses in the high μ medium. When $V_0 > V_s$ conservation of the volt-second product implies that the time T for the saturation wave to propagate through the core is related to the small-signal propagation time by

$$T/\Delta t = V_s/V_0. \tag{10.9}$$

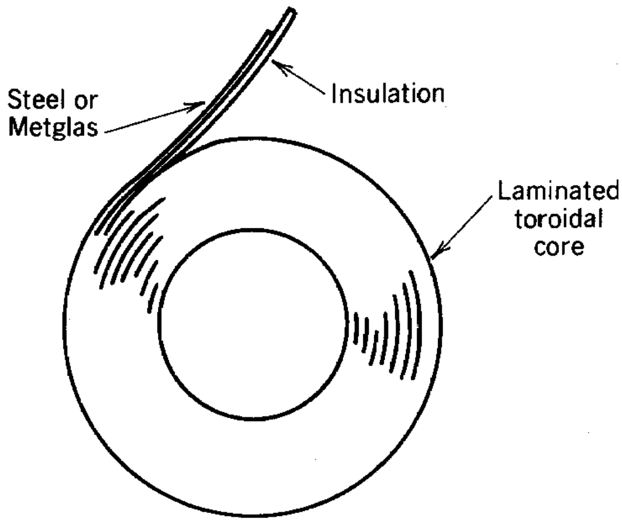

Figure 10.9 Construction of a laminated ferromagnetic isolation core.

The transmission line is charged to voltage V_0 at time T; therefore, a charge CV_0 flowed into the leakage circuit where C is the total capacitance of the circuit. The magnitude of the leakage current accompanying the saturation wave is thus $i = CV_0/T$, or

$$i = i_s\ (V_0/V_s). \qquad (10.10)$$

The leakage, current exceeds the value given in Eq. (10.8). Leakage current variation in the high-voltage limit is illustrated in Figure 10.8c.

In contrast to ferrites, the skin depth in steel or Metglas is much smaller than the dimension of the core. The core must therefore be divided into small sections so that the magnetic field penetrates the material. This is accomplished by laminated construction. Thin metal ribbon is wound on a cylindrical mandrel with an intermediate layer of insulation. The result is a toroidal core (Fig. 10.9). In subsequent analysees, we assume that the core is composed of nested cylinders and that there is no radial conduction of real current. In actuality, some current flows from the inside to the outside along the single ribbon. This current is very small because the path has a huge inductance. A laminated pulse core may contain thousands of turns.

Laminated steel cores are effective for pulses in the microsecond range. In the limit that $(R_o - R_i)/R_o \ll 1$, the applied magnetic field is the same at each lamination. The loop voltage around a lamination is thus V_0/N, where N is the number of layers. In an actual toroidal core, the applied field is proportional to $1/r$ so that lamination voltage is distributed unevenly; we will consider the consequences of flux variation in Section 10.4.

If the thickness of the lamination is less than the skin depth associated with the pulselength, then magnetic flux is distributed uniformly through a lamination. Even in this limit, it is difficult to calculate the inductance exactly because the magnetic permeability varies as the core field changes from $-B_r$ to B_s. For a first-order estimate of the leakage current, we assume an average

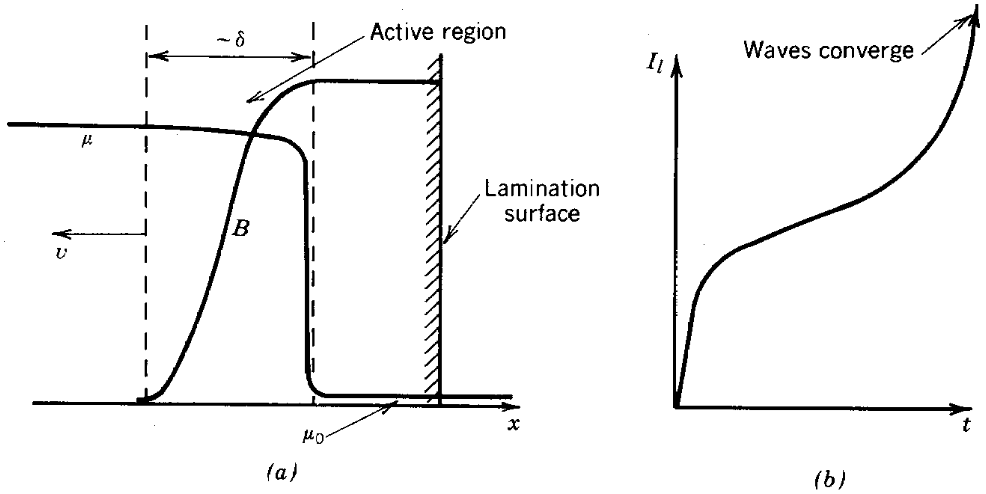

Figure 10.10 Saturation waves in a laminated ferromagnetic core. (*a*) Spatial variation of magnetic field and μ in a lamination. (*b*) Time variation of leakage current.

permeability $\bar{\mu} = B_s/H_s$. The inductance of the core is

$$L = \bar{\mu}\ d\ \ln(R_o/R_i)\ /\ 2\pi. \tag{10.11}$$

The time-dependent leakage current is

$$i_l \cong (V_0/L)\ t = [2\pi V_0/\bar{\mu}\ d\ \ln(R_o/R_i)]\ t. \tag{10.12}$$

The behavior of laminated cores is complex for high applied voltage and short pulselength. When the skin depth is less than half the lamination thickness, magnetic field penetrates in a saturation wave (Fig. 10.10a). There is an active layer with large flux change from atomic current alignment. There is a region behind the active layer of saturated magnetic material; the skin depth for field penetration is large in this region because $\mu \cong \mu_o$. Changes in the applied field are communicated rapidly through the saturated region. The active layer moves inward, and the saturation wave converges at the center at a time equal to the volt-second product of the lamination divided by V_0/N.

Although the volt-second product is conserved in the saturation wave regime, the inductance of the core is reduced below the value given by Eq. (10.11). This comes about because only a fraction of the lamination cross-sectional area contributes to flux change at a particular time. The core inductance is reduced by a factor on the order of the width of the active area divided by the half-width of the lamination. Accelerator efficiency is reduced because of increased leakage current and eddy current core heating. Leakage current in the saturation wave regime is illustrated in Figure 10.10b.

TABLE 10.2 Properties: Materials for Induction Linear Accelerators

Quantity	Ferrite (TDK PE-14)	Silicon Steel	Metglas Allied (2605SC)
ρ (Ω-m)	10^4	45×10^{-8}	125×10^{-8}
μ/μ_0 (small signal)	300–600	600	1200
$\langle(\mu/\mu_0)\rangle$ $B_s/\mu_0 H_s$ (static)		10^4	10^5
B_s (T)	0.4	1.4	1.6
B_r (T)	0.3	1.2	1.4
ΔB_{max} (T)	0.7	2.6	3.0

Core material and lamination thickness should be chosen so that skin depth is greater than half the thickness of the lamination. If this is impossible, the severity of leakage current effects can best be estimated by experimental modeling. Saturation wave analyses seldom give an accurate figure for leakage current. Measurements for a single lamination are simple; a loop around the lamination is driven with a pulse of voltage V_0/N and pulselength equal to that of the accelerator. The most reliable method to include the effects of radial field variations is to perform measurements on a full-radius core segment.

Properties of common magnetic materials are listed in Table 10.2. Ferrite cores have the capability for fast response; they are the only materials suitable for the 10-50 ns regime. The main disadvantages of ferrites are that they are expensive and that they have a relatively small available flux swing. This implies large core volumes for a given volt-second product.

Silicon steel is inexpensive and has a large magnetic field change, ~3 T. On the other hand, it is a brittle material and cannot be wound in thicknesses < 2 mil (5×10^{-3} cm). Reference to Figure 10.6 shows that silicon steel cores are useful only for pulselengths greater than 1 µs. There has been considerable recent interest in Metglas for induction accelerator cores. Metglas has a larger volume resistivity than silicon steel. Because of the method of its production, it is available in uniform thin ribbons. It has a field change about equal to silicon steel, and it is expected to be fairly inexpensive. Most important, because it is noncrystalline, it is not brittle and can be wound into cores in ribbons as thin as 0.7 mil (1.8×10^{-3} cm). It is possible to construct Metglas cores for short voltage pulses. If there is high load current and leakage current is not a primary concern, Metglas cores can be used for pulses in the 50-ns range.

The distribution of electric field in isolation cores must be known to determine insulation requirements. Electric fields have a simple form in laminated steel cores. Consider the core in the cavity geometry of Figure 10.11 with radial variations of applied field neglected. We know that there is a voltage V_0 between the inner and outer cylinders at the input end (marked α) and there is zero voltage difference on the right-hand side (marked β) because of the connecting radial

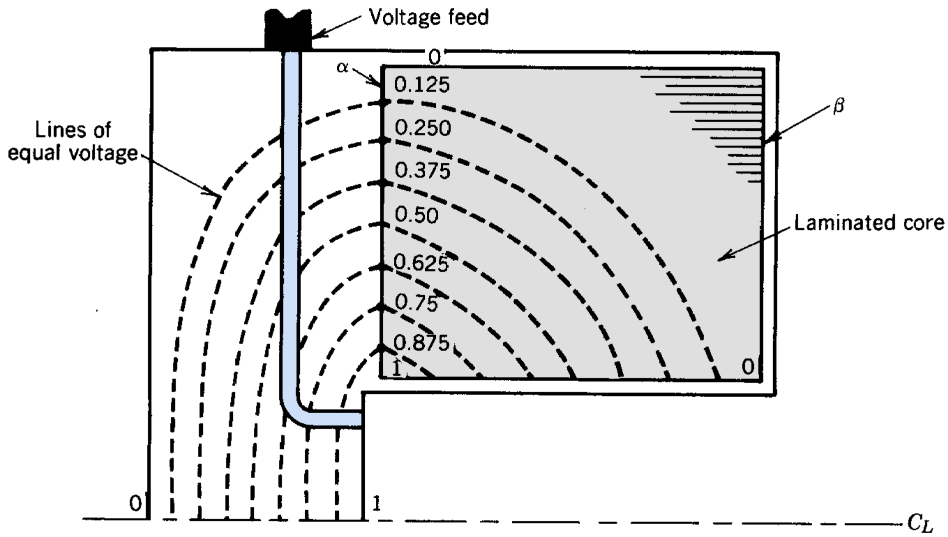

Figure 10.11 Distribution of voltage in a laminated isolation core (no local saturation).

conductor. Furthermore, the laminated core has zero conductivity in the radial direction but has high conductivity in the axial direction. Image charge is distributed on the laminations to assure that E_z equals zero along the surfaces. Therefore, the electric field is almost purely radial in the core. This implies that:

1. Except for small fringing fields, the electric field is radial along the input edge (α). The voltage drop across each insulating layer on the edge is V_0/N.

2. Moving into the core, inductive electric fields cancel the electrostatic fields. The net voltage drop across the insulating layers decreases linearly to zero moving from α to β.

Figure 10.11 shows voltage levels in the core relative to the outer conductor. Note that this is not an electrostatic plot; therefore, the equal voltage lines in the core are not normal to the electric fields.

10.3 VOLTAGE MULTIPLICATION GEOMETRIES

Inductive linear accelerator cavities can be configured as step-up transformers. High-current, moderate-voltage modulators can be used to drive a lower-current beam load at high voltage. Step-up cavities are commonly used for high-voltage electron beam injectors. Problems of beam transport and stability in subsequent acceleration sections are reduced if the injector voltage is high. Multi-MV electrostatic pulse generators are bulky and difficult to operate, but 0.25-MV modulators are easy to design. The inductive cavity of Figure 10.12a uses 10 parallel 0.25-MV

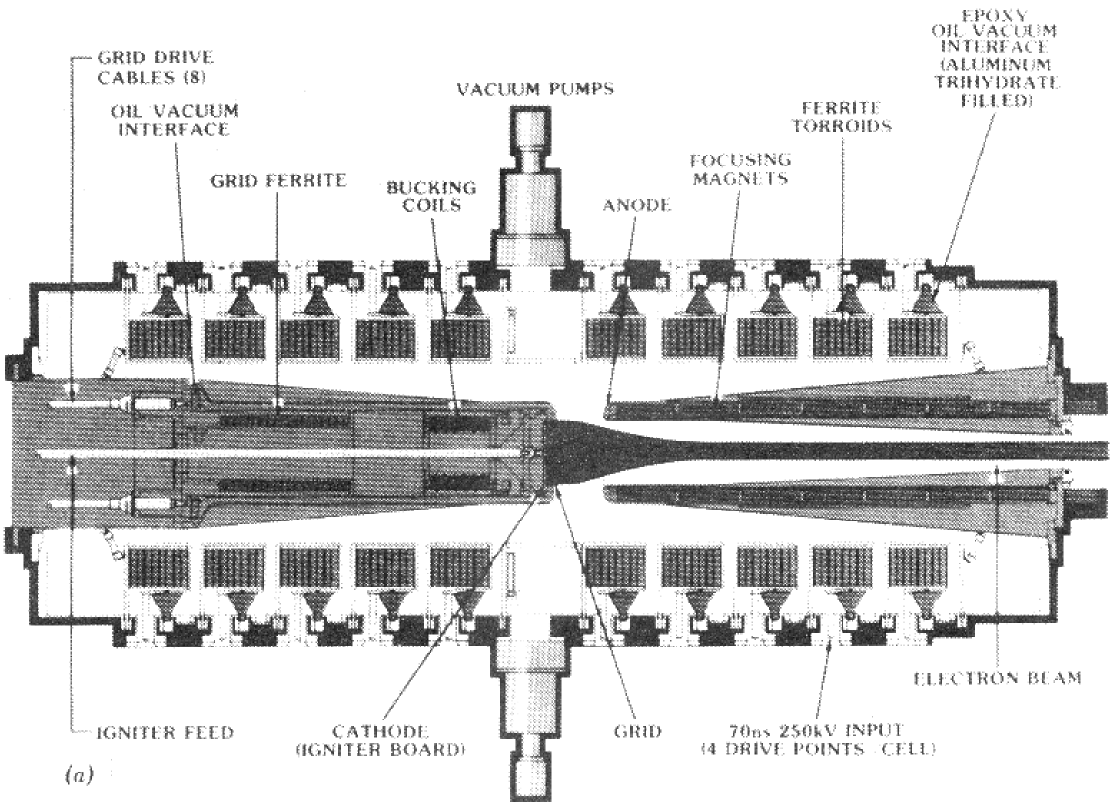

Figure 10.12 Longitudinal stacking of induction cells for electron injection high energy. (*a*) Scale drawing of ATA 2.5-MeV injector, Advanced Test Accelerator. (Courtesy D. Prono, Lawrence Livermore Laboratory.) (*b*) Current flow in a four-stage cavity.

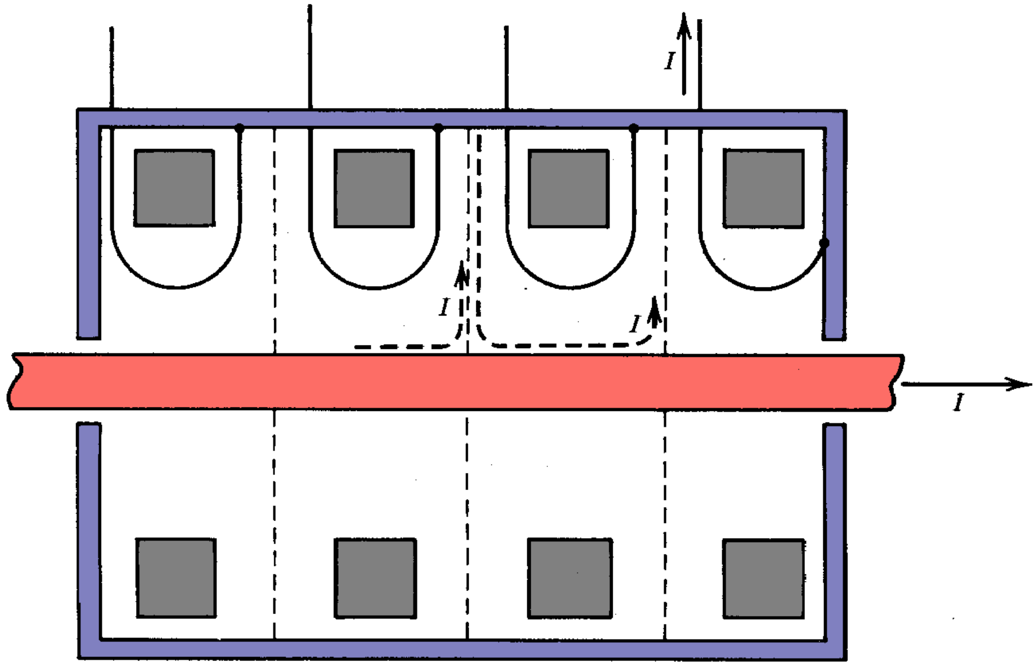

Figure 10.12 (*Continued*).

pulses to generate a 2.5-W pulse across an injection gap. Figure 10.12 illustrates *longitudinal core stacking.*

A schematic view of a 4:1 step-up circuit with longitudinal stacking is shown in Figure 10.12b. Note that if electrodes are inserted at the positions of the dotted lines, the single gap of Figure 10.12b is identical to a four-gap linear induction accelerator. The electrodes carry no current, so that the circuit is unchanged by their presence. We assume that the four input transmission lines of characteristic impedance Z_0 carry pulses with voltage V_0 and current $I_0 = V_0/Z_0$. A single modulator to drive the four lines must have an impedance $4Z_0$. The high core inductance constrains the net current through the axis of each core to be approximately zero. Therefore, the beam current for a matched circuit is I_0. The voltage across the acceleration gap is $4V_0$. The matched load impedance is therefore $4Z_0$. This is a factor of 16 higher than the primary impedance, as we expect for a 4:1 step-up transformer.

It is also possible to construct voltage step-up cavities with radial core stacking, as shown in Figure 10.13. It is more difficult to understand the power flow in this geometry. For clarity, we will proceed one step at a time, evolving from the basic configuration of Figure 10.1c to a dual-core cavity. We assume the beam load is driven by matched transmission lines. There are two main constraints if the leakage circuits have infinite impedance: (1) all the current in the system must be accounted for and (2) there is no net axial current through the centers of either of the cores.

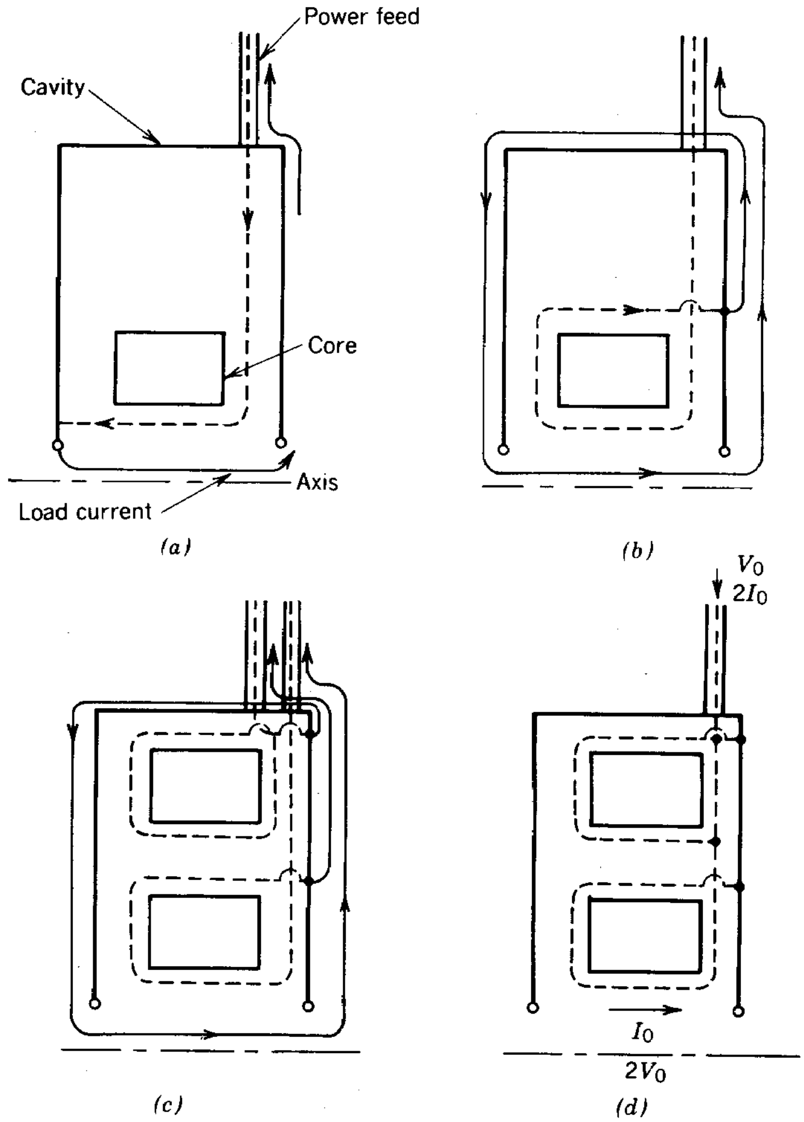

Figure 10.13 Acceleration cavity with radially stacked cores. Dashed arrows, current on power feeds; solid arrows, current in cavity. (*a*) Single core, simple power feed. (*b*) Single core with encircling power feed. (*c*) Two cores with dual power feeds. (*d*) Two cores with single power feed and flux-forcing connections.

Figure 10.13a shows a cavity with one core and one input transmission line. The difference from Figure 10.lc is that the line enters radially; this feature does not affect the behavior of the cavity. Note the current path; the two constraints are satisfied. In Figure 10.13b, the power lead is wrapped around the core and connected back to the input side of the inductive cavity. The current cannot flow outward along the wall of the cavity and return immediately along the transmission line outer conductor; this path has high inductance. Rather, the current follows the convoluted path shown, flowing through the on-axis load before returning along the ground lead of the transmission line. Although the circuit of Figure 10.13b has a more complex current path and higher parasitic inductance than that of Figure 10.12a, the net behavior is the same.

The third step is to add an additional core and an additional transmission line with power feed wrapped around the core. The voltage on the gap is $2V_0$ and the load current is equal to that from one line. Current flow from the two lines is indicated. The current paths are rather complex; current from the first transmission line flows around the inner core, along the cavity wall, and returns through the ground conductor of the second tine. The current from the second line flows around the cavity, through the load, back along the cavity wall, and returns through the ground lead of the first line. The cavity of Figure 10.13c conserves current and energy. Furthermore, inspection of the current paths shows that the net current through the centers of both cores is zero. An alternative configuration that has been used in accelerators with radially stacked cores is shown in Figure 10.13d. Both cores are driven by a single-input transmission line of impedance $V_0/2I_0$.

10.4 CORE SATURATION AND FLUX FORCING

In our discussions of laminated inductive isolation cores, we assumed that the applied magnetic field is the same at all laminae. This is not true in toroidal cores where the magnetic field decreases with radius. Three problems arise from this effect:

1. Electric fields are distributed unevenly among the insulation layers. They are highest at the center of the core.

2. The inner layers reach saturation before the end of the voltage pulse. There is a global saturation wave in the core; the region of saturation grows outward. The result is that the magnetically active area of the core decreases following saturation of the inner lamination. The inductance of the isolation circuit drops at the end of the pulse.

3. During the saturation wave, the circuit voltage is supported by the remaining unsaturated laminations. The field stress is highly nonuniform so that insulation breakdowns may occur.

The first problem can be addressed by using thicker insulation near the core center. The second and third problems are more troublesome, especially in accelerators with radially stacked cores. The effects of unequal saturation on the leakage current and cavity voltage are illustrated in Figure 10.14. The leakage current grows non-linearly during the latter portion of the pulse making compensation (Section 10.5) difficult. The tail end of the voltage pulse droops. Although the quantity $\int V dt$ is conserved, the waveform of Figure 10.14 may be useless for acceleration if a small beam energy spread is required.

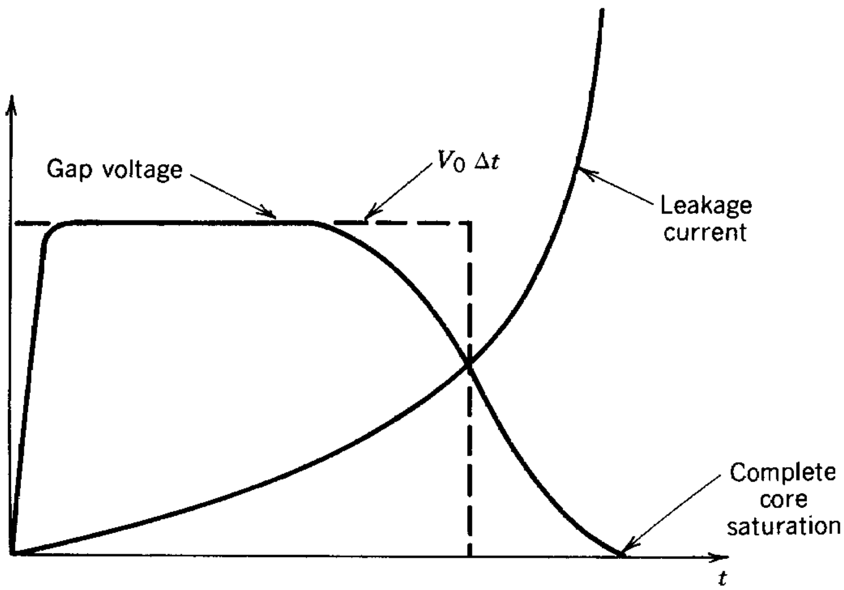

Figure 10.14 Acceleration gap voltage and leakage current waveforms with local saturation of isolation cores.

The problem of unequal saturation could be solved by using a large core to avoid saturation of the inner laminations. This approach is undesirable because core utilization is inefficient. The core volume and cost increase and the average accelerating gradient drops (see Section 10.7). Ideally, the core and cavity should be designed so that the entire volume of the core reaches saturation simultaneously at the end of the voltage pulse. This condition can be approached through *flux forcing.*

Flux forcing was originally developed to equalize saturation in large betatron cores. We will illustrate the process in a two-core radially stacked induction accelerator cavity. In Figure 10.15a, two open conducting loops encircle the cores. There is an applied voltage pulse of magnitude V_0. The voltage between the terminals of the outer loop is smaller than that of the inner loop because the enclosed magnetic flux change is less. The sum of the voltages equals V_0 with polarities as shown in the figure. In Figure 10.14b, the ends of the loops are connected together to form a single figure-8 winding. If the net enclosed magnetic flux in the outer loop were smaller than that of the inner loop, a high current would flow in the winding. Therefore, we conclude that a moderate current is induced in the winding that equalizes the magnetic flux enclosed by the two loops.

The figure-8 winding is called a *flux-forcing strap*. The distribution of current is illustrated in Figure 10.15c. The inner loop of the flux-forcing strap reduces the magnetic flux in the inner core, while the outer loop current adds flux at the outer core. If both cores in Figure 10.15 have the same cross-sectional area, they reach saturation at the same time because $d\Phi/dt$ is the same inside both loops. Of course, local saturation can still occur in a single core. Nonetheless, the severity of saturation is reduced for two reasons:

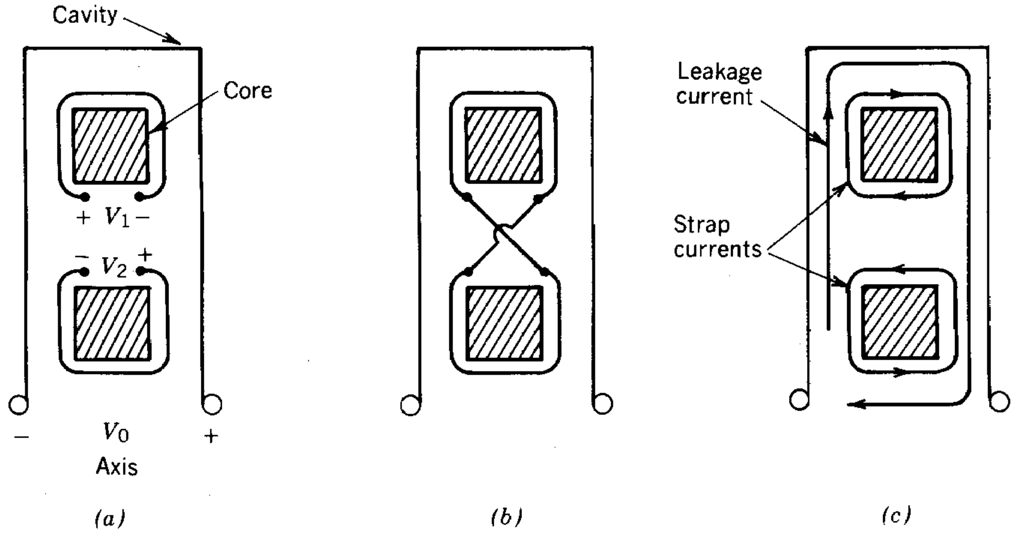

Figure 10.15 Flux-forcing straps. (*a*) Voltage on unconnected straps. (*b*) Figure-8 winding for flux forcing. (*c*) Current flow in flow-forcing straps relative to leakage current.

1. The ratio of the inner to outer radius is closer to unity for a single core section than for the entire stack.

2. Even if there is early saturation at the inside of the inner core, the drop in leakage circuit inductance is averaged over the stack.

Figure 10.16 illustrates an induction cavity with four core sections. The cavity was designed to achieve a high average longitudinal gradient in a long pulse linear induction accelerator. A large-diameter core stack was used for high cross-sectional area. There are two interesting aspects of the cavity:

1. The cores are driven in parallel from a single-pulse modulator. There is a voltage step-up by a factor of 4.

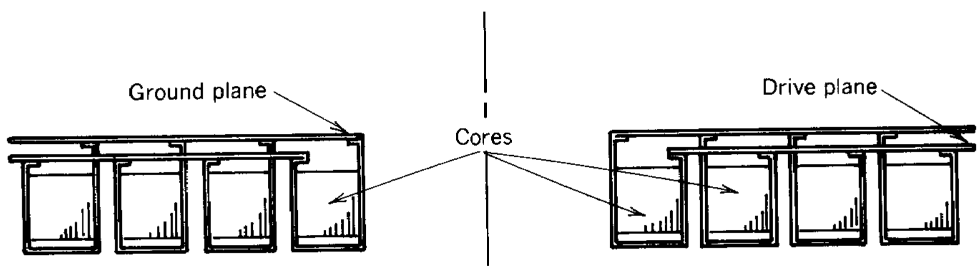

Figure 10.16 Core and power feed geometry for a 4 : 1 step-up cavity with flux forcing. (Courtesy M. Wilson, National Bureau of Standards.)

2. The parallel drive configuration assures that the loop voltage around each core is the same; therefore, the current distribution in the driving loops provides automatic flux forcing.

10.5 CORE RESET AND COMPENSATION CIRCUITS

Following a voltage pulse, the ferromagnetic core of an inductive accelerator has magnetic flux equal to $+B_r$. The core must be reset to $-B_r$ before the next pulse; otherwise, the cavity will be short-circuited soon after the voltage is applied.

Reverse biasing of the core is accomplished with a reset circuit. The reset circuit must have the following characteristics:

1. The circuit can generate an inverse voltage-time product greater than $(B_s+B_r)\ A_c$.

2. It can supply a unidirectional reverse current through the core axis of magnitude

$$I_s > 2\pi R_o H_s. \tag{10.13}$$

The quantity H_s is the magnetizing force of the core material and R_o is the outercore radius. Higher currents are required for fast-pulsed reset.

3. The reset circuit has high voltage isolation so that it does not absorb power during the primary pulse.

A long pulse induction cavity with reset circuit is shown in Figure 10.17. Note that a *damping resistor* in parallel with the beam load is included in the cavity. Damping resistors are incorporated in most induction accelerators. Their purpose is to prevent overvoltage if there is an error in beam arrival time. Some of the available modulator energy is lost in the damping resistor. Induction cavities have typical energy utilization efficiencies of 20-50%.

Reset is performed by an RC circuit connected to the cavity through a mechanical high-voltage relay. The relay acts as an isolator and a switch. The reset capacitor C_r is charged to voltage $-V_r$; the reset resistance R_r is small compared to the damping resistor R_d. There is an inductance L_r associated with the flow of reset current. Neglecting L_r and the current through the leakage circuit, the first condition above is satisfied if

$$\int V_r\ \exp(-t/R_dC_r)\ dt > (B_s+B_r)\ A_c. \tag{10.14}$$

If the inequality of Eq. (10.14) is well satisfied, the second condition is fulfilled if

$$V_r/R_d > I_s. \tag{10.15}$$

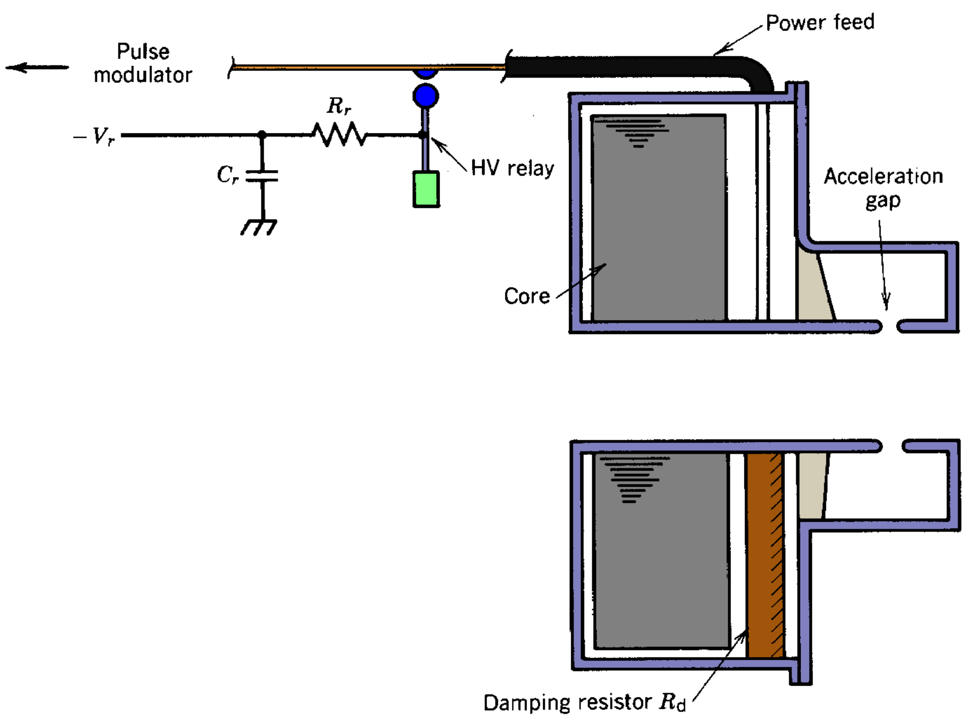

Figure 10.17 Reset circuit for a long-pulse induction cavity.

Equation (10.15) implies that the reset resistance should be as low as possible. There is a minimum value of R_r that comes about when the effect of the inductance L_r is included. Without the resistance, the circuit is underdamped; the reset voltage oscillates. The behavior of the *LC* circuit with saturable core inductor is complex; depending on the magnetic flux in the core following the voltage pulse and the charge voltage on the reset circuit, the core may remain with flux anywhere between $+B_r$ and $-B_r$ after the reset. Thus, it is important to ensure that reset current flows only in the proper direction. The optimum choice of R_r leads to a critically damped reset circuit:

$$R_s \geq > 2 \sqrt{L_r/C_r}, \tag{10.16}$$

when Eq. (10.16) is satisfied, the circuit generates a unidirectional pulse with maximum output current.

The following example illustrates typical parameters for an induction cavity and reset circuit. An induction linear accelerator cavity supports a 100-kV, 1-μs pulse. The beam current is 2 kA. The laniinated core is constructed of 2-mil silicon steel ribbon. The skin depth for the pulselength in silicon steel is about 0.33 mil. The core is therefore in the saturation wave regime. The available flux change in the laminations is 2.6 T. The radially sectioned core has a length of 8 in. (0.205 m). We assume about 30% of the volume of the isolation cavity is occupied by insulation and power straps. Taking into account the required volt-second product, the area of the core assembly is

$$A_c = (10^5\ V)(10^{-6}\ s)/(0.7)(2.6\ T) = 0.055\ m^2.$$

If the inner radius of the core assembly is 6 in. (0.154 m), then the outer radius must be 16.4 in. (0.42 m). These parameters illustrate two features of long-pulse induction accelerators: (1) there is a large difference between R_o and R_i so that flux forcing must be used for a good impedance match, and (2) the cores are large. The mass of the core assembly in this example (excluding insulation) is 544 kG. The beam impedance is 50 Ω. Assume that the damping resistor is 25 Ω and the charge voltage on the reset circuit is 1000 V. Equation (10.14) implies that

$$C_r > (0.1\ V{-}s)/(30\ \Omega)(1000\ V) = 3.3\ \mu F.$$

We choose C, = 10 μF; the core is reverse saturated 120 μs after closing the isolation relay. The capacitor voltage at this time is 670 V. Referring to the hysteresis curve of Figure 5.13, the required reset current is 670 A. This implies that R_d < 1 Ω. Assuming that the parasitic inductance of the reset circuit is about 1 μH, the resistance for a critically damped circuit is 0.632 Ω; therefore, the reset circuit is overdamped, as required.

A convenient method of core reset is possible for short-pulse induction cavities driven by pulse-charged Blumlein line modulators. In the system of Figure 10.18a, a Marx generator is used to charge an oil- or water-filled Blumlein line. The Blumlein line provides a flat-top voltage pulse to a ferrite or Metglas core cavity. A gas-filled spark gap shorts the intermediate conductor to the outer conductor to initiate the pulse. In this configuration, the intermediate conductor is charged negative for a positive output pulse. The crux of the auto-reset process is to use the negative current flowing from the center conductor of the Blumlein line during the pulse-charge cycle to reset the core. Reset occurs just before the main voltage pulse. Auto-reset eliminates the need for a separate reset circuit and high-voltage isolator. A further advantage is that the core can be driven to $-B_s$ just before the pulse.

Figure 10.18b shows the main circuit components. The impulse generator has capacitance C_g and inductance L_g. It has an open circuit voltage of $-V_0$. If the charge cycle is long compared to an electromagnetic transit time, the inner and outer parts of the Blumlein line can be treated as lumped capacitors of value C_1. The outer conductor is grounded; the inner conductor is connected to ground through the induction cavity. We assume there is a damping resistor R_d that shunts some of the reset current. We will estimate $V_c(t)$ (the negative voltage on the core during the charge cycle) and determine if the quantity $\int V_c dt$ exceeds the volt-second product of the core.

Assume that $V_c(t)$ is small compared to the voltage on the intermediate conductor. In this case, the voltage on the intermediate conductor is approximated by Eq. (9.102) with $C_2 = 2C_1$. Assuming that $C_g = 2C_1$ the voltage on the intermediate conductor is

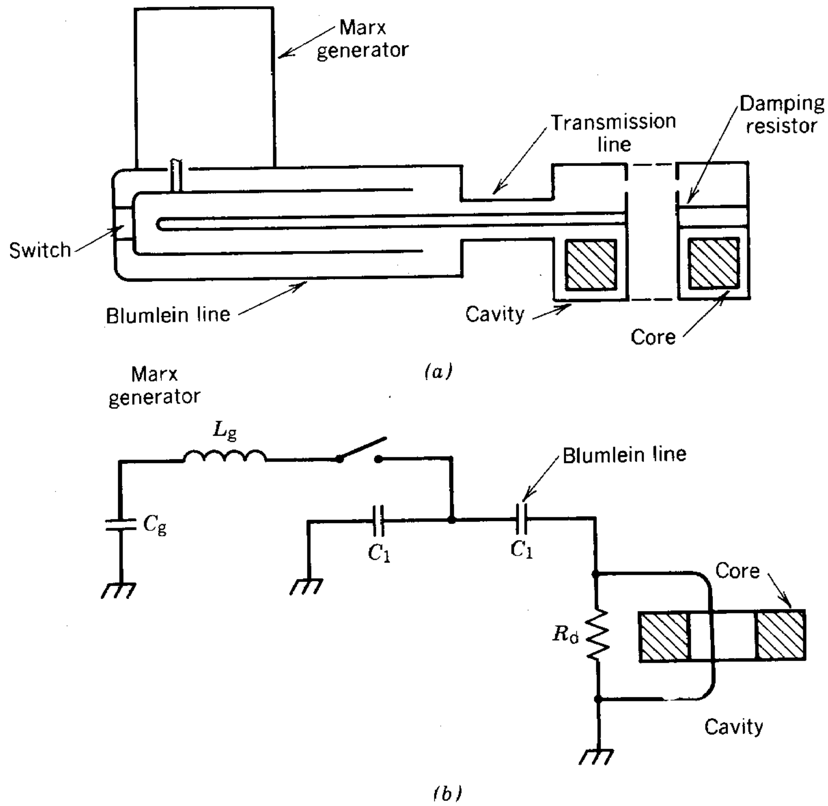

Figure 10.18 Auto-reset in an induction cavity driven by a Blumlein line. (*a*) System geometry. (*b*) Equivalent circuit.

$$V_2 = [V_0\ (1-\cos\omega t)]/2, \tag{10.17}$$

where $\omega = 1/\sqrt{L_g C_1}$.The charging current to the cavity is $i_c \cong C_1\ (dV_2/dt)$. Assuming most of this current flows through the damping resistor, the reset voltage on the core during the Blumlein line charge is

$$V_c \cong -\ (V_0/2)\ (R_d\ /\ \sqrt{L/C_1})\ \sin\omega t. \tag{10.18}$$

If the Blumlein is triggered at the time of completed energy transfer, $t = \pi/\omega$, then the volt-second integral during the charge phase is

$$\int V_C\ dt = V_0\ (C_1 R_d). \tag{10.19}$$

The integral of Eq. (10.19) must exceed the volt-second product of the core for successful reset. This criterion can be written in a convenient form in terms of Δt_p, the length of the main voltage pulse in the cavity. Assuming a square pulse of magnitude V_0, the volt-second product of the core should be $V_0 \Delta t_p$. Substituting this expression in Eq. (10.19) gives the following condition:

$$\Delta t_p \;\leq\; C_1 R_d. \tag{10.20}$$

Furthermore, we can use Eq. (9.89) to find the pulselength in terms of the line capacitance. Equation (10.20) reduces to the following simple criterion for auto-reset:

$$Z_1 \;\leq\; R_d. \tag{10.21}$$

The quantity Z_1 is the net output impedance of the Blumlein line, equal to twice the impedance of the component transmission lines. Clearly, Eq. (10.21) is always satisfied.

In summary, auto-reset always occurs during the charge cycle if (1) the Marx generator is matched to the Blumlein line, (2) the core volt-second product is matched to the output voltage pulse, and (3) the Blumlein line impedance is matched to the combination of beam and damping resistor. Reset occurs earlier in the charge cycle as R_d is increased. The condition of Eq. (10.21) holds only for the simple circuit of Figure 10.18. More complex cases may occur; for instance, in some accelerators the cavity and Blumlein line are separated by a long transmission line which acts as a capacitance during the charge cycle. Premature core saturation shorts the reset circuit and can lead to voltage reversal on the connecting line. The resulting negative voltage applied to the cavity subtracts from the available volt-second product.

Flat voltage waveforms are usually desirable. In electron accelerators, voltage control assures an output beam with small energy spread. Voltage waveform shaping is essential for induction accelerators used for nonrelativistic particles. In this case, a rising voltage pulse is required for longitudinal beam confinement (see Section 13.5). Power is usually supplied from a pulse modulator which generates a square pulse in a matched load. There are two primary causes of waveform distortion: (1) beam loading and (2) transformer droop. We will concentrate on transformer droop in the remainder of this section.

The equivalent circuit of an induction linear accelerator cavity is shown in Figure 10.19a. The driving modulator maintains constant voltage if the current to the cavity is constant. Current is divided between the beam load, the damping resistor, and the leakage inductance. The leakage current increases with time; therefore, the cavity does not present a matched load at an times and the voltage droops. The goal is to compensate leakage current by inserting an element with a rising impedance.

A simple compensation circuit is shown in Figure 10.19b. A series capacitor is added to the damping resistor so that the impedance of the damping circuit rises with time. We can estimate the value of capacitance that must be added to keep V_0 constant by making the following

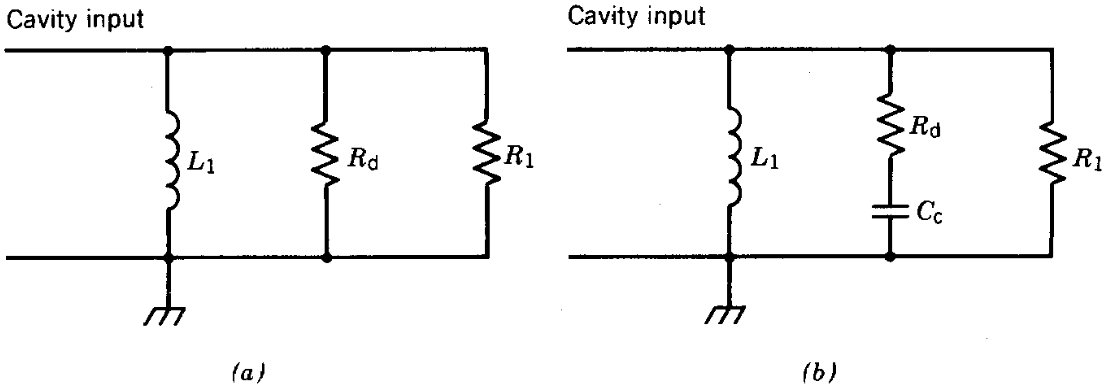

Figure 10.19 Compensation of voltage droop in an induction cavity. (*a*) Equivalent circuit of cavity with damping resistor R_d, no compensation. (*b*) Simple compensation circuit.

simplifying assumptions: (1) the leakage path inductance is assumed constant over the pulselength, Δt_p; (2) the voltage on the compensation capacitor C_c is small compared to V_0; (3) the leakage current is small compared to the total current supplied by the modulator; and (4) the beam current is constant. The problem resolves into balancing the increase in leakage current by a decrease in damping current.

With the above assumptions, the time-dependent leakage current is

$$i_1 \cong V_0 t/L_1 \tag{10.22}$$

for a voltage pulse initiated at $t = 0$. The current through the damping circuit is approximately

$$i_d \cong (V_0/R_d)\ (1 - t/R_d C_d). \tag{10.23}$$

Balancing the time-dependent parts gives the following condition for constant circuit current:

$$R_d C_c = L_1/R_d. \tag{10.24}$$

As an example, consider the long-pulse cavity that we have already discussed in this section. Taking the average value of μ/μ_o as 10,000 and applying Eq. (9.15), the inductance of the leakage path for ideal ferromagnetic material is

$$L_1 = (\mu/\mu_o)\ (\mu_o/2\pi)\ d\ \ln(R_o/R_i) \cong 400\ \mu H.$$

The core actually operates in the saturation regime with a skin depth about one-third the half-thickness of the lamination; we can make a rough estimate of the leakage current by dividing the inductance by three, $L_1 = 133\ \mu$H. With a damping resistance of $R_d = 30\ \Omega$ and a cavity voltage of 100 kV, the modulator supplies a current greater than 5.3 kA. The leakage current is maximum at the end of the pulse. Equation (10.22) implies that i_1 = 0.25 kA at t = Δt_p, so that the third assumption above is valid. The compensating capacitance is predicted from Eq. (10.24) to be C_c = 0.15 µF. The maximum voltage on the capacitor is 22 kV: thus, assumption 2 is also satisfied. Capacitors are generally available in the voltage and capacitance range required, so that the compensation method of Figure 10.19 is feasible.

10.6 INDUCTION CAVITY DESIGN: FIELD STRESS AND AVERAGE GRADIENT

At first glance, it is difficult to visualize the distribution of voltage in induction cavities because electrostatic and inductive electric fields act in concord. In order to clarify field distributions, we shall consider the specific example of the electron injector illustrated in Figure 10.20. The configuration is the most complex one that would normally be encountered in practice. It has

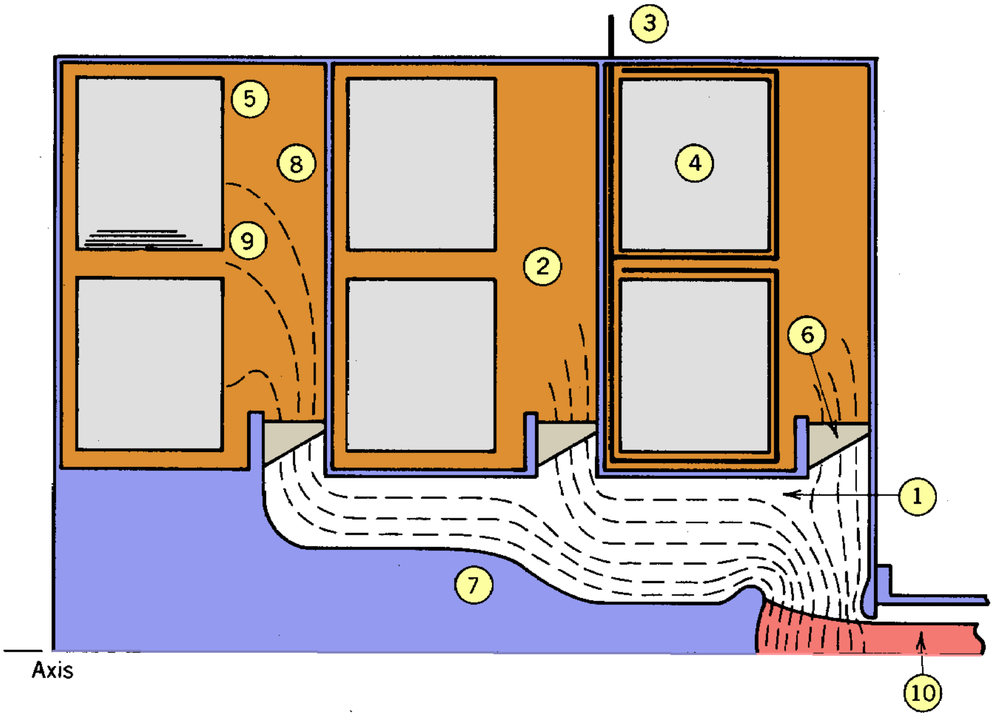

Figure 10.20 Equipotential lines in six-core injector cavity with radial and longitudinal stacking. (1) Vacuum region, acceleration gap. (2) Transformer oil insulation. (3) Insulated power feed. (4) Laminated isolation core. (5) Exposed face of laminated core. (6) Vacuum insulator with optimized shaping. (7) Shaped negative high-voltage electrode with electron source. (8) Grounded face of laminated core. (9) Location of equipotential line at voltage V_0 with respect to outer wall when flux-forcing straps used. (10) Extracted electron beam.

laminated cores, longitudinal stacking, radial stacking, and flux-forcing straps. We shall develop an electric field map for times during which all core laminations are unsaturated. In the following discussion, bracketed numbers are keyed to points in the figure.

1. Three cavities are combined to provide 3:1 longitudinal voltage step-up. The load circuit region (1) is maintained at high vacuum, for electron transport. The leakage circuit region (2) is filled with transformer oil for good insulation of the core and high-voltage leads. The vacuum insulator (6) is shaped for optimum resistance to surface breakdown.

2. Power is supplied through transmission lines entering the cavity radially (3). At least two diametrically opposed lines should be used in each cavity. Current distribution from a single power feed has a strong azimuthal asymmetry. If a single line entered from the top, the magnetic field associated with load current flow would be concentrated at the top, causing a downward deflection of the electron beam.

3. The cores (4) are constructed by interleaving continuous ribbons of ferromagnetic material and insulator; laminations are orientated as shown in Figure 10.20. One of the end faces (5) must be exposed; otherwise, the cavity will be shorted by conduction across the laminations.

4. If V_0 is the matched voltage output of the modulator, a single cavity produces a voltage $2V_0$. Equipotential lines corresponding to this voltage pass through the vacuum insulator (6). At radii inside the vacuum insulator, the field is electrostatic. The inner vacuum region has coaxial geometry. To an observer on the center conductor (7), the potential of the outer conductor appears to increase by $2V_0$ crossing each vacuum insulator from left to right.

5. Equipotential lines are sketched in Figure 10.20. In the vacuum region, an equal number of lines is added at each insulator. The center conductor is tapered to minimize the secondary inductance and to preserve a constant field stress on the metal surfaces.

6. In the core region, the electric field is the sum of electrostatic and inductive contributions. We know that the two types of fields cancel along the shorted wall (8). We have already discussed the distribution of equipotential lines inside the core in Section 10.2, so we will concentrate on the potential distribution on the exposed face (5). The inclusion of flux-forcing straps ensures that the two cores in each subcavity enclose equal flux. This implies that the point marked (9) between the cores is at a relative potential Vo.

7. Each lamination in the cores isolates a voltage proportional to the applied magnetic field $B_1(r)$. Furthermore, electrostatic fields in the core are radial. Therefore, the electric field along the exposed face of an individual core has a l/r variation, and potential varies as $\Phi(r) \sim \ln(r)$. The electrostatic potential distribution in the oil insulation has been sketched by connecting equipotential lines to the specified potential on the exposed core surface (5).

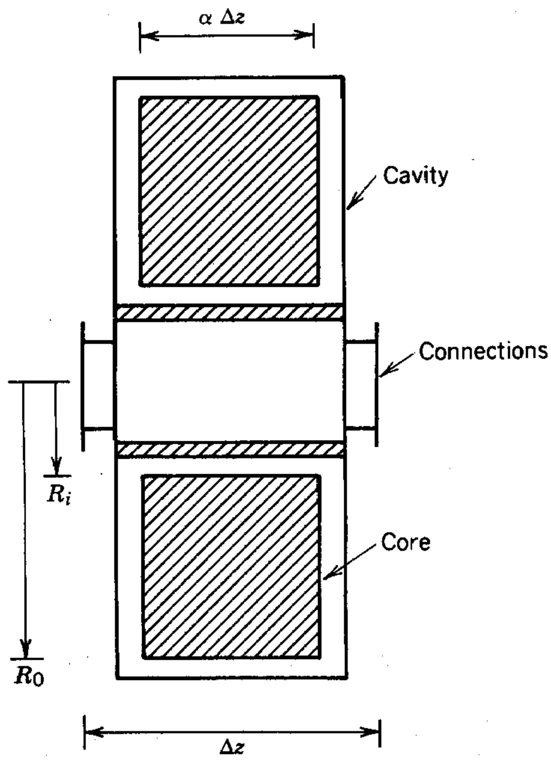

Figure 10.21 Geometric parameters for calculation of average gradient of linear induction accelerator.

In summary, although the electric field distribution in compound inductive cavities is complex, we can estimate it by analyzing the problem in parts. The distribution could be determined exactly with a computer code to solve the Laplace equation in the presence of dielectrics. There is a specified boundary condition on φ along the core face. It should be noted that the above derivation gives, at best, a first-order estimate of field distributions. Effects of core nonlinearities and unequal saturation complicate the situation considerably.

Average longitudinal gradient is one of the main figures of merit of an accelerator. Much of the equipment associated with a linear accelerator, such as the accelerator tunnel, vacuum systems, and focusing system power supplies, have a cost that scales linearly with the accelerator length. Thus, if the output energy is specified, there is an advantage to achieving a high average gradient. In the induction accelerator, the average gradient is constrained by the magnetic properties and geometry of the ferromagnetic core. Referring to Figure 10.21, assume the core has inner and outer radii R_i and R_o, and define κ as the ratio of the radii, $\kappa = R_o/R_i$. The cavity has length Δz of which the core fills a fraction α. If particles gain energy ΔE in eV in a cavity with pulselength t_p, the volt-second constraint implies the following difference equation:

$$\Delta E\ t_p = \Delta B\ (R_o - R_i)\ \alpha\ \Delta z. \tag{10.25}$$

where ΔB is the volume-averaged flux change in the core. The pulselength may vary along the length of the machine; Eq. (10.25) can be written as an integral equation:

$$\int_{E_i}^{E_f} dE\ t_p(E) = \alpha\ \Delta B\ R_o\ (\kappa-1)\ L, \qquad (10.26)$$

where E_f is the final beam energy in electron volts, E_i is the injection energy, and L is the total length. Accelerators for relativistic electrons, have constant pulselength. Equation (10.26) implies that

$$(E_f - E_i)/L = \alpha\ \Delta B\ R_o\ (\kappa-1)\ /\ \Delta t_p\ (V/m). \qquad (10.27)$$

In proposed accelerators for nonrelativistic ion beams [see A,Fattens, E. Hoyer, and D. Keefe, **Proc. 4th Intl. Conf. High Power Electron and Ion Beam Research and Technology**, (Ecole Polytechnique, 1981), 751]. the pulselength is shortened as the beam energy is raised to maintain a constant beam length and space charge density. One possible variation is to take the pulselength inversely proportional to the longitudinal velocity:

$$t_p(E) = t_{pf}\ \sqrt{E_f\ /\ E(z)}. \qquad (10.28)$$

The quantity t_{pf} is the pulselength of the output beam. Inserting Eq. (10.28) into Eq. (10.26) gives

$$\left(E_f - \sqrt{E_f E_i} \right) / L = \alpha\ \Delta B\ R_o\ (\kappa-1)\ /\ 2t_{pf}. \qquad (10.29)$$

In the limit that $E_i \ll E_f$, the expressions of Eqs. (10.27) and (10.29) are approximately equal to the average longitudinal gradient. In terms of the quantities defined, the total volume of ferromagnetic cores in the accelerator is

$$V = \pi\ (\kappa^2-1)\ \alpha\ L\ R_o^2. \qquad (10.30)$$

Equations (10.27), (10.29), and (10.30) have the following implications:

1. High gradients are achieved with a large magnetic field swing in the core material (ΔB) and the tightest possible core packing α.
2. The shortest pulselength gives the highest gradient. Properties of the core material and the inductance of the pulse modulators determine the minimum t_p. High-current ferrite accelerators have a minimum practical pulselength of about 50 ns. The figure is about 1 μs for silicon steel

cores and 100 ns for Metglas cores with thin laminations. Because of their high flux swing and fast pulse response, Metglas cores open new possibilities for high-gradient-induction linear accelerators.

3. The average gradient is maximized when κ approaches infinity. On the other hand, the net core volume is minimized when L approaches infinity. There is a crossover point of minimum accelerator cost at certain values of κ and L, depending on the relative cost of cores versus other components.

Substitution of some typical parameters in Eq. (10.27) will indicate the maximum gradient that can be achieved with a linear induction accelerator. Take t_p = 100 ns pulse and a Metglas core with ΔB = 2.5 T, R_i = 0.1 in and R_o = 0.5 m. Vacuum ports, power feeds, and insulators must be accommodated in the cavity in addition to the cores; we will take α = 0.5. These numbers imply a gradient of 5 MV/m. This gradient is within a factor of 2-4 of those achieved in rf linear electron accelerators. Higher gradients are unlikely because induction cavities have vacuum insulators exposed to the full accelerating electric fields.

10.7 CORELESS INDUCTION ACCELERATORS

The ferromagnetic cores of induction accelerator cavities are massive, and the volt-second product limitation restricts average longitudinal gradient. There has been considerable effort devoted to the development of linear induction accelerators without ferromagnetic cores [A. I. Pavlovskii, A, I. Gerasimov, D. I. Zenkov, V. S. Bosamykin, A. P. Klementev, and V. A. Tananakin, Sov. At. Eng. **28**, 549 (1970)]. These devices incorporate transmission lines within the cavity. They achieve inductive isolation through the flux change accompanying propagation of voltage pulses through the lines.

In order to understand the coreless induction cavity, we must be familiar with the radial transmission line (Fig. 10.22). This geometry has much in common with the transmission lines we have already studied except that voltage pulses propagate radially. Consider the conical section electrode as the ground conductor ans the radial plate is the center conductor. The structure has minimum radius R_i. We take the inner radius as the input point of the line. If voltage is applied to the center conductor, a voltage pulse travels outward at a velocity determined by the medium in the line. The voltage pulse maintains constant shape. If the line extends radially to infinity, the pulse never returns. If the line has a finite radius (R_o), the pulse is reflected and travels back to the center.

It is not difficult to show that the structure of Figure 10.22 has constant characteristic impedance as a function of radius. (In other words, the ratio of the voltage and current associated with a radially traveling pulse is constant.) In order to carry out the analysis, we assume that α, the angle of the conical electrode, is small. In this case, the electric field lines are primarily in the axial direction. There is a capacitance per unit of length in the radial direction given by

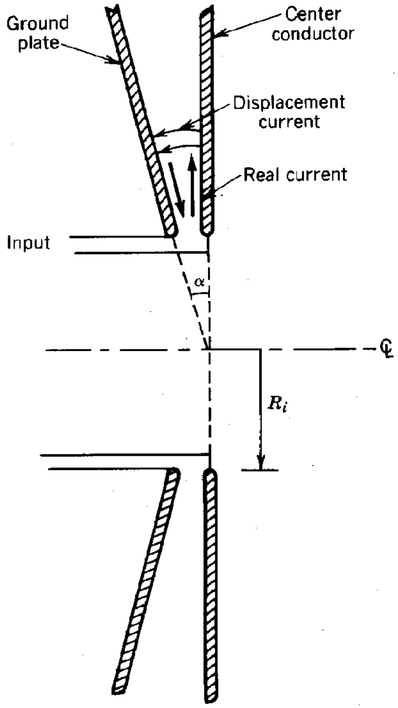

Figure 10.22 Current flow in radial transmission line.

$$c\Delta r \cong (2\pi r\Delta r)\varepsilon \;/\; r\ \tan\alpha = (2\pi\varepsilon/\tan\alpha)\ \Delta r. \tag{10.31}$$

In order to determine the inductance per unit of radial length, we must consider current paths for the voltage pulse. Inspection of Figure 10.22 shows that current flows axially through the power feed, outward along the radial plate, and axially back across the gap as displacement current. The current then returns along the ground conductor to the input point. If the pulse has azimuthal symmetry, the only component of magnetic field is B_θ. The toroidal magnetic field is determined by the combination of axial feed current, axial displacement current, and the axial component of ground return current. Radial current does not produce toroidal magnetic fields. The combination of axial current components results in a field of the form

$$B_\theta = \mu I/2\pi r \tag{10.32}$$

confined inside the transmission line behind the pulse front. The region of magnetic field expands as the pulse moves outward, so there is an inductance associated with the pulse. The magnetic field energy per element of radial section length is

$$U_m dr = (B_\theta^2/2\mu)\ (2\pi r dr)\ (r\ \tan\alpha) = \mu\ I^2\ \tan\alpha\ dr/4\pi. \tag{10.33}$$

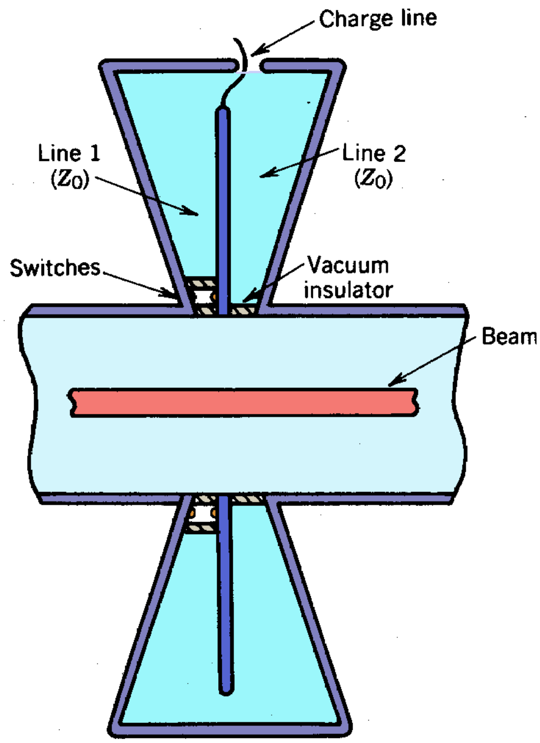

Figure 10.23 Coreless induction cavity.

This energy is equal to $\frac{1}{2} l I^2 dr$, so that

$$l = \mu \tan\alpha / 2\pi. \tag{10.34}$$

To summarize, both the capacitance and inductance per radial length element are constant. The velocity of wave propagation is

$$v = 1/\sqrt{lc} = 1/\sqrt{\epsilon\mu}. \tag{10.35}$$

as expected. The characteristic impedance is

$$Z_o = \sqrt{l/c} = (\tan\alpha/2\pi)\ \sqrt{\mu/\epsilon}. \tag{10.36}$$

For purified water dielectric, Eq. (10.34) becomes

$$Z_o = 3.4 \tan\alpha\ (\Omega). \tag{10.37}$$

The basic coreless induction cavity of Figure 10.23 is composed of two radial transmission lines. There are open-circuit terminations at both the inner and outer radius; the high-voltage radial electrode is supported by insulators and direct current charged to high voltage. The region at the outer radius is shaped to provide a matched transition; a wave traveling outward in one line propagates without reflection through the transition and travels radially inward down the other line. There is a low-inductance, azimuthally symmetric shorting switch in one line at the inner radius. The load is on the axis. We assume, initially that the load is a resistor with $R = Z_0$; subsequently, we will consider the possibility of a beam load which has time variations synchronized to pulses in the cavity.

The electrical configuration of the coreless induction cavity is shown schematically in Figure 10.24a. Because the lines are connected at the outer radius, we can redraw the schematic as a single transmission of length $2(R_o - R_i)$ that doubles back and connects at the load, as in Figure 10.24b. The quantity Δt is the transit time for electromagnetic pulses through both lines, or

$$\Delta t = 2\ (R_o - R_i)/v. \tag{10.38}$$

The charging feed, which connects to a Marx generator, approximates an open circuit during the fast output pulse of the lines. Wave polarities are defined with respect to the ground conductor; the initial charge on the high-voltage electrode is $+V_0$. As in our previous discussions of transmission lines, the static charge can be resolved into two pulses of magnitude $\frac{1}{2}V_0$ traveling in opposite directions, as shown. There is no net voltage across the load in the charged state.

Consider the sequence of events that occurs after the switch is activated at $t = 0$.

1. The point marked A is shorted to the radial electrode. During the time $0 < t < \Delta t$, the radial wave traveling counterclockwise encounters the short circuit and is reflected with reversed polarity. At the same time, the clockwise pulse travels across the short circuit and backward through the matched resistance, resulting in a voltage $-\frac{1}{2}V_0$ across the load. Charged particles gain an energy $\frac{1}{2}qV_0$ traveling from point A to point B. The difference in potential between A and B arises from the flux change associated with the traveling pulses.

2. At time $t = \Delta t$, the clockwise-going positive wave is completely dissipated in the load resistor. The head of the reflected negative wave arrives at the load. During the time $\Delta t < t < 2\Delta t$, this wave produces a positive voltage of magnitude $\frac{1}{2}V_0$ from point B to point A. The total waveform at the load is shown in Figure 10.25a.

The bipolar waveform of Figure 10.25a is clearly not very useful for particle acceleration. Only half of the stored energy can be used. Better coupling is achieved by using the beam load as a switched resistor. The beam load is connected only when the beam is in the gap. Consider the following situation. The beam, with a current $V_0/2Z_o$, does not arrive at the acceleration gap until time Δt. In the interval $0 < t < \Delta t$ the gap is an open circuit. The status of the reflecting waves is illustrated in Figure 10.24c. The counterclockwise wave reflects with inverted polarity; the clockwise wave reflects from the open circuit gap with the same polarity. The voltage from B to A

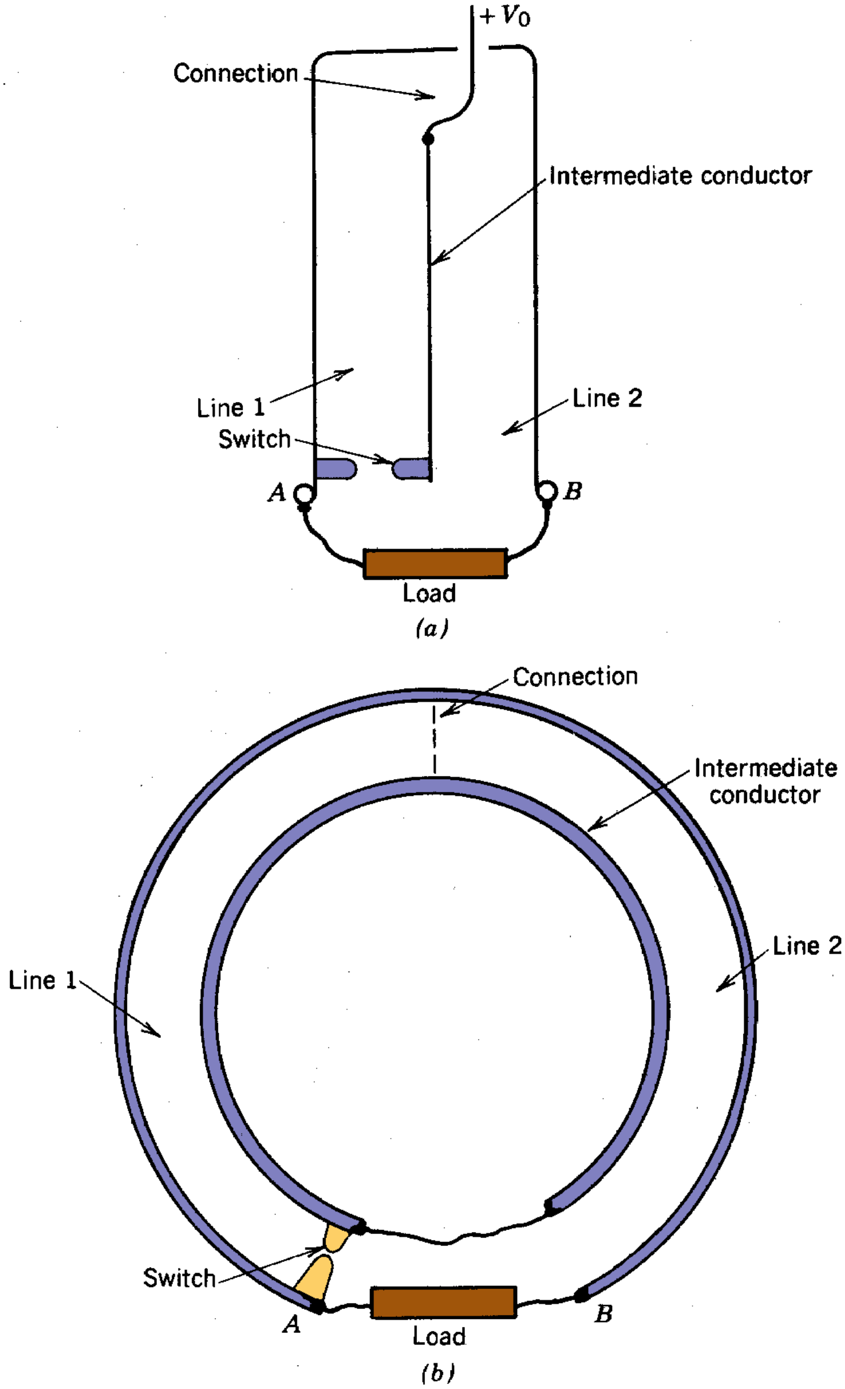

Figure 10.24 Coreless induction cavity. (*a*) Simplified geometry. (*b*) Equivalent geometry with ideal outer connection between lines. (*c*) Resolution of static charge into traveling square pulses; polarity and propagation direction of pulses immediately following switch shorting.

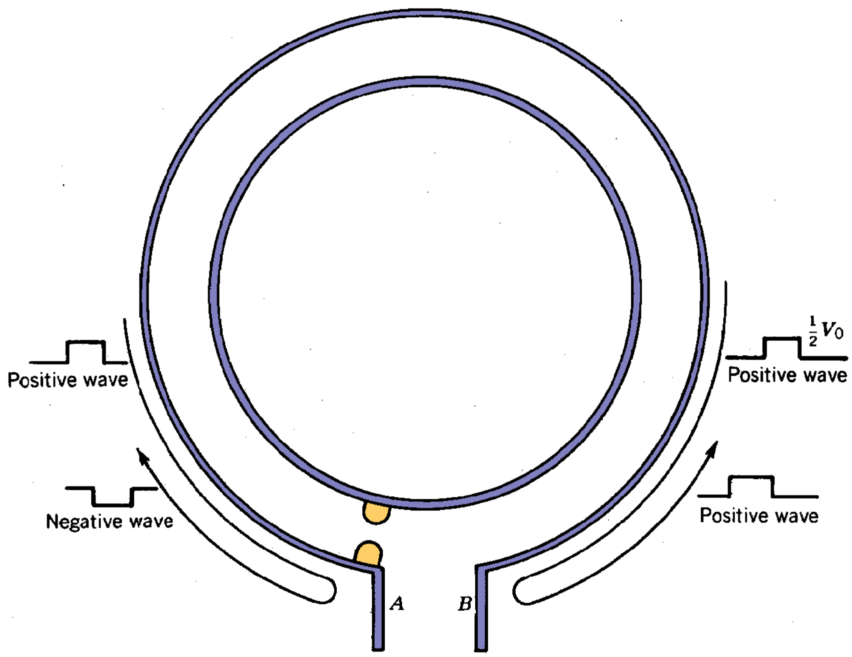

(c)

Figure 10.24 (*Continued*).

is the open-circuit voltage V_0. At time t = Δt, both the matched beam and the negative wave arrive at the gap. The negative wave makes a positive accelerating voltage of magnitude ½V_0 during the time $\Delta t < t < 2\Delta t$. In the succeeding time interval, $2\Delta t < t < 3\Delta t$, the other wave which has been reflected once from the open-circuit termination and once from the short-circuit termination arrives at the gap to drive the beam. The waveform for this sequence is illustrated in Figure 10.25b. In theory, 100% of the stored energy can be transferred to a matched beam load at voltage ½V_0 for a time 2Δt.

Although coreless induction cavities avoid the use of ferromagnetic cores, technological difficulties make it unlikely that they will supplant standard configurations. The following problems are encountered in applications:

1. The pulselength is limited by the electromagnetic transit time in the structure. Even with a high dielectric constant material such as water, the radial transmission lines must have an outer diameter greater than 9 ft for an 80-ns pulse.
2. Energy storage is inefficient for large-diameter lines. The maximum electric field must be chosen to avoid breakdown at the smallest radius. The stored energy density of electric fields [Eq. (5.19)] decreases as $1/r^2$ moving out in radius.

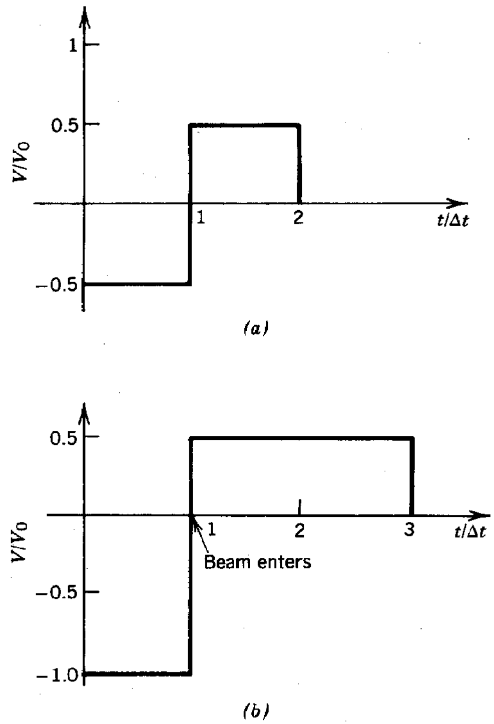

Figure 10.25 Voltage waveform in coreless induction cavity. (*a*) Simple matched load resistor. (*b*) Synchronized beam load with matched impedance.

3. Synchronous low-inductance switching at high voltage with good azimuthal symmetry is difficult.

4. Parasitic inductance in the load circuit tends to be larger than the primary inductance of the leakage path because the load is a beam with radius that is small compared to the radius of the shorting switches. The parasitic inductance degrades the gap pulse shape and the efficiency of the accelerator.

5.The switch sequence for high-efficiency energy transfer means that damping resistors cannot be used in parallel with the gap to protect the cavity.

6. The vacuum insulators must be designed to withstand an overvoltage by a factor of 2 during the open-circuit phase of wave reflection.

One of the main reasons for interest in coreless induction accelerators was the hope that they could achieve higher average accelerating gradients than ferromagnetic cavity accelerators. In fact, a careful analysis shows that coreless induction accelerators have a significant disadvantage in terms of average gradient compared to accelerators with ferromagnetic isolation. We will make the comparison with the following constraints:

1. The cavities have the same pulselength Δt_p and beamcurrent I_o.

2. Regions of focusing magnets, pumping ports, and insulators are not included.

3.The energy efficiency of the cavities is high.

We have seen in Section 10.6 that the gradient of an ideal cavity with ferromagnetic isolation of length l with core outer radius R_o and inner radius R_i is

$$V_0/l = \Delta B \ (R_o - R_i) \ / \ \Delta t_p. \tag{10.39}$$

where ΔB is the maximum flux swing. Equation (10.39) proceeds directly from the volt-second limitation on the core. In a radial line cavity, the cavity length is related to the outer radius of the line, R_o, by

$$l = 2 \ R_o \ \tan\alpha, \tag{10.40}$$

where α is the angle of the conical transmission lines. The voltage pulse in a high-efficiency cavity with charge voltage V_0 has magnitude $\frac{1}{2}V_0$ and duration

$$\tau_p = 4 \ (R_o - R_i) \ \sqrt{\varepsilon/\varepsilon_o}/c, \tag{10.41}$$

where R_i is the inner radius,of the transmission lines. We further require that the beam load is matched to the cavity:

$$Z_o = V_0/2I_0.$$

The characteristic impedance is given by Eq. (10.36). Combining Eq. (10.36) with Eqs. (10.40) and (10.41) gives the following expression for voltage gradient:

$$V_0/l = (\mu_o/\pi) \ (1 - R_i/R_o) \ I_o \ / \ \Delta t_p.$$

Equation (10.42) has some interesting implications for coreless induction cavities. First, gradient in an efficient accelerator is proportional to beam current. Second, the gradient for a given pulselength is relatively insensitive to the outer radius of the line. This reflects the fact that the energy storage density is low at large radii. Third, the gradient for ideal cavities does not depend on the filling medium of the transmission lines. Within limits of practical construction, an oil-filled line has the same figure of merit as a water-filled line.

In order to compare the ferromagnetic core and coreless cavities, assume the following conditions. The pulselength is 100 ns and the beam current is 50 kA (the highest current that has presently been transported a significant distance in a multistage accelerator). The ferromagnetic core has R_o = 0.5 m, R_i = 0.1 m, and ΔB = 2.5 T. The coreless cavity has $R_i/R_o \ll 1$. Equation (10.39) implies that the maximum theoretical gradient of the Metglas cavity is 10 MV/m, while Eq. (10.42) gives an upper limit for the coreless cavity of only 0.16 MV/m, a factor of 63 lower. Similar results can be obtained for any coreless configuration. Claims for high gradient in coreless accelerators usually are the result of implicit assumptions of extremely short pulselengths (10-20 ns) and low system efficiency.